

# **DEVELOPMENT OF SEGMENTATION TECHNIQUE TO EXTRACT BLOOD VESSELS FROM RETINAL IMAGES**

A

## **THESIS**

Presented to the Faculty of Engineering and Technology  
Punjabi University, Patiala  
in fulfillment of the requirements for the award of the degree of

**DOCTOR OF PHILOSOPHY**

**IN**

**COMPUTER SCIENCE & ENGINEERING**



(Established Under Punjab Act No.35 of 1961)

**NAVDEEP SINGH**  
(Reg. No. 7141-12-1109)

**DEPARTMENT OF COMPUTER SCI. & ENGG.,**

**PUNJABI UNIVERSITY, PATIALA-147002**

**MARCH, 2020**

## **Supervisor's CERTIFICATE**

This is to certify that this thesis entitled "Development of Segmentation Technique To Extract Blood Vessels from Retinal Images" embodies the work carried out by Navdeep Singh himself under my supervision and that is worthy of consideration for the award of the Ph.D. degree.

**(Dr. Lakhwinder Kaur)**  
Professor,  
Dept of Comp. Sci. & Engg.,  
Punjabi University, Patiala.  
(Supervisor)

**(Dr. Kuldeep Singh)**  
Assistant Professor,  
Dept. of Electronics & Comm Engg.,  
MNIT, Jaipur,  
(Co-Supervisor)

----- ----- -----  
Day      Month      Year

## **Candidate's DECLARATION**

I Navdeep Singh certify that the work embodied in this Ph. D. thesis is my own bonafide work carried out by me under the supervision of Dr. Lakhwinder Kaur and Dr. Kuldeep Singh from July 2014 to Dec 2019 at Department of Computer Science & Engineering, Punjabi University, Patiala. The matter embodied in this Ph.D. thesis has not been submitted for the award of any other degree/diploma.

I declare that I have faithfully acknowledged, given credit to and referred to the research workers wherever their works have been cited in the text and in the body of the thesis. I further certify that I have not willfully lifted up some other's work, para, text, data, results, etc. reported in the journals, books, magazines, reports, dissertations, theses, etc., or available at web-sites and included them in this Ph. D. thesis and cited as my own work. I also declare that I have adhered to all principles of academic honesty and integrity and have not misrepresented or fabricated or falsified any idea/data/fact/source in my submission. I understand that any violation of the above will be cause for disciplinary action by the University.

Date: .....

Place: Patiala

(Navdeep Singh)

This is to certify that the above statement made by the candidate is correct to the best of my/our knowledge.

**(Dr. Lakhwinder Kaur)**  
Professor  
Dept. of Comp. Sci. & Engg.  
Punjabi University Patiala  
(Supervisor)

**(Dr. Kuldeep Singh)**  
Assistant Professor,  
Dept. of Electronics & Comm Engg.,  
MNIT, Jaipur,  
(Co-Supervisor)

## Abstract

Diseases are on the rise in all parts of the world. The study shows the leading diseases affecting the population are hypertension, diabetes, stroke, and cardiovascular diseases. The effect of diabetes alone is observed to be extremely severe as it is going to affect 366 million people by the end of the year 2030, an increase of 195 million from the year 2000. Careful examination of the disease is thus the need of the hour in order to have timely medication of the patient so that the patient can be saved from life-threatening situations. The seriousness of the disease can easily be observed by a prudent investigation of the blood vessels in the retina. Extracting blood vessels manually from the retina is a time-consuming process and can only be done by a skilled professional as a lot of effort is needed to differentiate between the blood vessels and other artefacts such as the macula, fovea, etc. present in the retina. Automatic segmentation of the blood vessels, therefore, becomes very necessary in order to overcome the problems being faced in the manual segmentation. Automatic segmentation of the blood vessels can be done by any naive person and that too very accurately and swiftly thus saving a lot of effort.

The work starts with a detailed study and analysis of the existing literature and based on the research gaps, objectives have been defined. In order to accomplish the objectives, the author has broadly contributed two techniques; (i) Image Enhancement technique and (ii) Retinal Vessel Segmentation technique. The proposed techniques have been implemented in MATLAB and tested on publicly available four datasets, (i) DRIVE (Digital Retinal Images for Vessel Extraction), (ii) STARE (Structured Analysis of Retinal Images), (iii) CHASE (Child Heart and Health Study in England), and (iv) OASIS (Open Access Series of Imaging Studies). The findings are provided both quantitatively and qualitatively. Output images have been shown for qualitative assessment. Quantitative assessment of the techniques has been done in terms of metrics such as Information Content (Entropy), PSNR (Peak Signal to Noise Ratio), SSIM (Structured Similarity Index Measurement), Euclidean Distance, Sensitivity, Specificity, and Accuracy.

The databases used in this work contains fundus images of different age groups varying from children images to the images of the adults. The fundus cameras used to

take the images have a different set configuration for different datasets. Also, the images have been taken under varying light conditions because of various factors such as the distance of the eye from the imaging device, improper expansion of the pupil, and movement of the eyeball. As a result, most of the images are affected by low and non-uniform illumination. These factors hamper the process of extraction of the blood vessels from the retina. Image preprocessing thus becomes very important to enhance the quality of the images. In the preprocessing step, both the problems of low and non-uniform illumination are addressed to get a high-quality image. The high-quality image helps in better and efficient extraction of the blood vessels from the retina. In this work, two techniques, RIHE-RVE (Radiance indicator based histogram equalization for retinal vessel enhancement) and RIHE-RRVE (Radiance indicator based histogram equalization for recursive retinal vessel enhancement) are proposed to enhance the quality of the images. In both the techniques, the tunable parameter decides the point of the split of the histogram i.e. the intensity value where the histogram will be split into two sub-histograms. In RIHE-RVE, the two sub-histograms are first equalized separately and are then integrated to get a histogram. This process of split, equalization, and integration is done repeatedly depending on the difference between the radiance values of successive enhanced images corresponding to the obtained histograms. In the case of RIHE-RRVE, the histogram is first split into a number of sub-histograms depending on the chosen level of decomposition and then all the sub-histograms are equalized separately and integrated to obtain the final histogram. In addition to the above two techniques, a third technique to address the problem of over-enhancement in images has also been proposed in this work. In this approach, the histogram is clipped based on the cumulative median value prior to splitting of the histogram into sub-histograms in order to avoid over enhancement. The proposed techniques are robust in nature in a sense as they can not only be applied to retinal images but also to the images belonging to other domains. To demonstrate the effectiveness of the proposed techniques quantitatively, experiments have been performed on both retinal images taken from DRIVE, STARE, and CHASE\_DB1 datasets as well as MRI images taken from OASIS dataset. Results in terms of Entropy, PSNR, SSIM, and Euclidean distance have been compared with various other well established techniques. Both quantitative and qualitative inspection shows that the proposed methods efficiently address the

problem of low and non-uniform illumination/radiance in the images without producing unwanted artefacts.

To extract the blood vessels from the retinal images, a new feature-oriented dictionary learning and sparse coding-based ensemble classification approach has been proposed. The image is first converted into the grayscale image and then Contrast Limited Adaptive Histogram Equalization (CLAHE) technique is applied to increase the contrast of the image besides handling the non-uniform illumination in the image. In this technique, patches are created from images and for each patch, Gabor features are calculated at different scales and orientations to create feature vectors. There is a very high correlation between adjacent pixels of the image in a patch, down sampling is therefore done to reduce the information redundancy. An over complete dictionary is then learned from the feature-oriented feature vectors which are chosen on the basis of the defined threshold value of standard deviation using the KSVD dictionary learning algorithm. Once the dictionary is learned, sparse representations are calculated using Orthogonal Matching Pursuit (OMP) algorithm. A combination of feature-oriented vectors and corresponding sparse vectors is then used to train the classifier for the classification of pixels into either vessel pixels or non-vessel pixels. Post processing of the image is then done to reduce the impulse noise introduced in the image. The proposed technique is robust in nature and can handle images which are affected by noise. Another benefit associated with the proposed technique is that it requires very less number of samples for training the classifier in comparison to the well-established classification techniques. To assess the efficacy of the proposed techniques quantitatively, experiments have been conducted on the publicly available DRIVE and STARE datasets and results have been obtained in terms of sensitivity, specificity, and accuracy. Visual quality inspection clearly demonstrates the superiority of the proposed technique over existing techniques. Both quantitative, as well as qualitative results, suggest that the proposed technique outperforms most of the state of the art techniques.

The work presented in this thesis can be incorporated in the medical imaging devices for accurate automatic extraction of the blood vessels from the fundus images which can be used in the diagnosis of various diseases such as diabetic retinopathy, hypertension etc.

## List of Publications

1. Singh, N., Kaur, L., & Singh, K. (2019). Histogram equalization techniques for enhancement of low radiance retinal images for early detection of diabetic retinopathy. *Engineering Science and Technology, an International Journal*. Publisher: Elsevier, Indexing: [**SCI, ESCI, Scopus**].
2. Navdeep Singh, Lakhwinder Kaur, Kuldeep Singh, "Segmentation of retinal blood vessels based on feature-oriented dictionary learning and sparse coding using ensemble classification approach," *J. Med. Imag.* 6(4) 044006 (22 November 2019). Publisher: SPIE, Indexing: [**PubMed, ESCI, EI, Scopus**].
3. Singh, N., & Kaur, L. (2015). A survey on blood vessel segmentation methods in retinal images. **IEEE** International Conference on Electronic Design, Computer Networks and Automated Verification, EDCAV 2015.
4. Singh, N., Kaur, L., & Singh, K. (2019) A Review of the Retinal Blood Vessel Segmentation Techniques. **Springer** International Conference on Intelligent Machines, ICIM 2019. [**Communicated**]

## Acknowledgment

First of all, I would like to convey my indebtedness to the Almighty for blessing me with the courage, determination, and patience at every single phase right through my journey. I would like to express my gratitude to many people who cooperated and assisted me in completing my research work.

I would like to express my sincere gratitude to my respected supervisors Dr. Lakhwinder Kaur and my co-supervisor Dr. Kuldeep Singh for their persistent guidance, motivation, advice, and exceptional patience. I am really thankful for the amount of time, technical knowledge and moral support they have given me during this period of my work.

I extend my hearty thanks to the researchers and scholars for their papers and code that have been referenced in this work.

I would also like to express my gratitude to departmental research board members for their valuable suggestions.

I also want to acknowledge the motivational support given by my parents Mr. Karam Singh and Mrs. Krishna Devi, brother Mr. Vickram Singh and sister Mrs. Kuldeep Kaur. They are a source of immense inspiration to me and they were always there alongside me during my hard times.

Last but not the least, my hearty thanks to my kids Gurshan and Gurparwan for sacrificing their precious time during my research work.

Finally, I am out of words to express my gratitude to my loving wife Mrs. Rajdeep Kaur for her relentless support, motivation and care during my period of research work.

## List of Acronyms

RVA	Retinal vessel analysis
BMI	Body mass index
AD	Alzheimer disease
MCI	Mild cognitive impairment
AHE	Adaptive histogram equalization
CLAHE	Contrast Limited Adaptive Histogram Equalization
VLM	Vessel location map
PCA	Principal component analysis
ROI	Region of interest
LID	Left invariant derivative
LID-OS	Left invariant derivative on orientation scores
LAD	Locally adaptive derivative
LAD-OS	Locally adaptive derivative on orientation scores
GVF	Gradient vector flow
OFA	Oriented flux anti-symmetry
OAF	Optimal oriented flux
GPU	Graphical processor unit
ROC	Receiver operating characteristic curve
SN	Sensitivity
SP	Specificity

ACC	Accuracy
GMM	Gaussian mixture model
NN	Neural network
Ppv	Positive predictive value
Npv	Negative predictive value
CHASE	Child Heart and Health study in England
DRIVE	Digital retinal images for vessel extraction
STARE	Structured analysis of the retina
OASIS	Open access series of imaging studies
OCT	Optical coherence tomography
SVM	Support vector machine
AUC	Area under curve
LNNDP	Lattice Neural Network with Dendritic Processing
MLP	Multilayer perceptron
MCC	Mathews Correlation Coefficient
MFR	Matched filter response
TPR	True positive rate
FPR	False positive rate
DDL	Discriminative dictionary learning
ELM	Extreme Learning Machine
CART	Classification and Regression Trees
MPMF	Multiscale production of matched filter

SRC	Sparse representation classifier
CNN	convolutional neural networks
RF	Random Forest
DRVM	Directional response vector maps
mRmR	Maximal relevance and minimum redundancy
MF-FDOG	First order derivative of Gaussian based matched filter
GLCM	Gray level co-occurrence matrix
MF	Matched filter
SSIM	Structure similarity index measurement
PSNR	Peak signal to noise ratio
HE	Histogram equalization
CDF	Cumulative distribution function
BBHE	Brightness preserving bi-histogram equalization
BHEPL	Bi-histogram equalization with a plateau limit
DOTHE	Dominant orientation-based texture histogram equalization
SVD	Singular value decomposition
RSIHE	Recursive sub-image histogram equalization
MSSI	Mean structural similarity index
QDHE	Quadrant dynamic histogram equalization
RSWHE	Recursively separated and weighted histogram equalization
DoG	Difference of Gaussian
RIHE-RVE	Radiance indicator based histogram equalization for retinal vessel enhancement

RIHE-RRVE	Radiance indicator based
FDL	Feature-oriented dictionary learning
KSVD	K-means for singular value decomposition
BP	Basis pursuit
OMP	Orthogonal matching pursuit

# Table of Contents

Supervisor's CERTIFICATE.....	i
Candidate's DECLARATION .....	ii
Abstract.....	iii
List of Publications.....	vi
Acknowledgment.....	vii
List of Acronyms.....	viii
Chapter 1.....	1
1.1 Introduction .....	1
1.2 Motivation .....	2
1.3 Retinal fundus photography .....	3
1.3.1 Modes of examination.....	4
1.4 Retinal Vessel Segmentation.....	5
1.5 Challenges in Retinal Vessel Segmentation.....	6
1.6 Applications of Retinal Vessels.....	7
1.7 Organization of Thesis .....	8
1.8 Chapter summary.....	9
Chapter 2.....	11
2.1 Introduction .....	11
2.2 Image enhancement .....	11

2.3 Vessel segmentation.....	17
2.3.1 Deformable models .....	17
2.3.2 Vessel Tracking approaches .....	21
2.3.3 Machine learning approaches .....	24
2.4 Research Gaps .....	42
2.5 Research objectives.....	43
2.6 Research Methodology.....	43
2.6.1 Pre-processing.....	43
2.6.2 Feature extraction.....	44
2.6.3 Classification .....	44
2.6.4 Post-processing .....	44
2.7 Image Quality Metrics .....	44
2.7.1 Entropy .....	44
2.7.2 Structure Similarity Index Measure (SSIM).....	45
2.7.3 Peak Signal to Noise Ratio (PSNR).....	45
2.7.4 Euclidean Distance.....	45
2.8 Image segmentation metrics.....	46
2.8.1 Sensitivity .....	46
2.8.2 Specificity .....	46
2.8.3 Accuracy.....	46

2.9 Datasets .....	47
2.10 Chapter summary .....	49
 Chapter 3 .....	 51
3.1 Introduction .....	51
3.2 Retinal image enhancement techniques .....	52
3.2.1 Histogram Equalization (HE) .....	52
3.2.2 Brightness preserving bi-histogram equalization (BBHE).....	53
3.2.3 Bi-Histogram Equalization with a Plateau Limit (BHEPL) .....	54
3.2.4 Dominant Orientation-based Texture Histogram Equalization (DOTHE) .....	56
3.2.5 Recursive sub-image histogram equalization (RSIHE) .....	58
3.2.6 Quadrant Dynamic Histogram Equalization for Contrast Enhancement (QDHE) .....	59
3.2.7 Recursively Separated and Weighted Histogram Equalization (RSWHE) .....	60
3.3 Retinal Vessel Segmentation techniques .....	63
3.3.1 2-D Matched Filter based vessel segmentation .....	63
3.3.2 A hybrid filter of Matched and Difference of Gaussian filter based segmentation.....	64
3.3.3 Retinal Vessel Segmentation using Line Operator .....	65
3.3.4 Retinal Vessel Segmentation using Gabor wavelet and SVM.....	67

3.4 Results and Discussion.....	69
3.4.1 Performance Analysis of Image Enhancement techniques .....	69
3.4.2 Performance Analysis of Vessel Segmentation techniques.....	83
3.5 Chapter summary.....	91
Chapter 4.....	93
4.1 Introduction .....	93
4.2 Proposed work .....	93
4.2.1 Proposed Algorithms.....	94
4.3 Experimental Results .....	100
4.3.1 Dataset used.....	100
4.3.2 Performance evaluation based on visual inspection .....	100
4.3.3 Performance evaluation based on objective information .....	101
4.4 Chapter summary.....	106
Chapter 5.....	107
5.1 Introduction .....	107
5.2 Proposed work .....	107
5.2.1 Sparse representation model.....	108
5.2.2 Proposed Technique .....	109
5.3 Experimental Results .....	117
5.3.1 Material used.....	117

5.3.2 Performance evaluation.....	117
5.4 Chapter summary.....	126
Chapter 6.....	127
6.1 Conclusion.....	127
6.2 Significance to the Society .....	128
6.3 Scope of Future Work .....	129
References.....	131

## List of Figures

<b>Figure No.</b>	<b>Label</b>	<b>Page No.</b>
1.1	Fundus camera being used to capture the image of the retina	4
2.1	Block diagram of supervised technique	24
2.2	Block diagram of unsupervised technique	25
2.3	Flowchart of Blood Vessel Segmentation process	43
2.4	Sample images of DRIVE dataset	47
2.5	Manually annotated corresponding sample images of DRIVE dataset	48
2.6	Sample images of STARE dataset	48
2.7	Manually annotated corresponding sample images of STARE dataset	48
2.8	Sample images of CHASE dataset	48
2.9	Manually annotated corresponding sample images of CHASE dataset	48
2.10	Sample images of OASIS dataset	48
3.1	Image segmentation using Line operator	66
3.2	Image segmentation using Gabor filter	68
3.3	Average Entropy results obtained using various image enhancement techniques	80
3.4	Average SSIM results obtained using various image enhancement techniques	81

3.5	Average PSNR results obtained using various image enhancement techniques	81
3.6	Average Euclidean distance results obtained using various image enhancement techniques	81
3.7	Enhanced images obtained after applying various techniques on the image obtained from DRIVE dataset	82
3.8	Enhanced images obtained after applying various techniques on the image obtained from STARE dataset	82
3.9	Enhanced images obtained after applying various techniques on the image obtained from CHASE dataset	83
3.10	Average Sensitivity results obtained using various vessel segmentation techniques on DRIVE and STARE datasets	88
3.11	Average Specificity results obtained using various vessel segmentation techniques on DRIVE and STARE datasets	88
3.12	Average Accuracy results obtained using various vessel segmentation techniques on DRIVE and STARE datasets	88
3.13	Image segmentation using Matched Filter	89
3.14	Matched filter technique for vessel extraction at various orientations	89
3.15	Comparison of matched filter, DoG filter, and hybrid filter	90
3.16	Image segmentation using Line Operator	90
3.17	Gabor filter convolved maximum modulus image	90
4.1	Flowchart of RIHE-RVE technique	97
4.2	Flowchart of RIHE-RRVE technique	98
4.3	Effect of tuneable parameter ' $\psi$ ' and split level 'r' on the amount of radiance	100
4.4	Comparison of various techniques on CHASE dataset	103

4.5	Comparison of various techniques on STARE dataset	104
4.6	Comparison of various techniques on DRIVE dataset	104
4.7	Comparison of various techniques on OASIS images	104
5.1	Block diagram of the proposed technique	109
5.2	Basic image operations	110
5.3	Patch extraction	112
5.4	Gabor filters in six orientations and two scales	112
5.5	Image segmentation using the proposed approach	118
5.6	Best and Worst Case accuracy for the DRIVE dataset using LogitBoost classifier	119
5.7	Best and Worst Case accuracy for the STARE dataset using AdaBoost classifier	119

## List of Tables

<b>Table No.</b>	<b>Label</b>	<b>Page No.</b>
3.1	Performance metrics obtained on DRIVE dataset using Histogram Equalization(HE)	70
3.2	Performance metrics obtained on STARE dataset using Histogram Equalization(HE)	70
3.3	Performance metrics obtained on CHASE dataset using Histogram Equalization (HE)	71
3.4	Performance metrics obtained on DRIVE dataset using Brightness preserving Bi-Histogram Equalization (BBHE)	71
3.5	Performance metrics obtained on STARE dataset using Brightness preserving Bi-Histogram Equalization (BBHE)	72
3.6	Performance metrics obtained on CHASE dataset using Brightness preserving Bi-Histogram Equalization (BBHE)	72
3.7	Performance metrics obtained on DRIVE dataset using Bi-Histogram Equalization with Plateau Limit (BHEPL)	73
3.8	Performance metrics obtained on STARE dataset using Bi-Histogram Equalization with Plateau Limit (BHEPL)	73
3.9	Performance metrics obtained on CHASE dataset using Bi-Histogram Equalization with Plateau Limit (BHEPL)	74
3.10	Performance metrics obtained on DRIVE dataset using Dominant Orientation-based Texture Histogram Equalization (DOTHE)	74
3.11	Performance metrics obtained on STARE dataset using Dominant Orientation-based Texture Histogram Equalization (DOTHE)	75
3.12	Performance metrics obtained on CHASE dataset using Dominant Orientation-based Texture Histogram Equalization (DOTHE)	75
3.13	Performance metrics obtained on DRIVE dataset using Recursive sub-image Histogram Equalization (RSIHE)	76
3.14	Performance metrics obtained on STARE dataset using Recursive sub-image Histogram Equalization (RSIHE)	76
3.15	Performance metrics obtained on CHASE dataset using Recursive sub-image Histogram Equalization (RSIHE)	77

3.16	Performance metrics obtained on DRIVE dataset using Quadrant dynamic histogram equalization (QDHE)	77
3.17	Performance metrics obtained on STARE dataset using Quadrant dynamic histogram equalization (QDHE)	78
3.18	Performance metrics obtained on CHASE dataset using Quadrant dynamic histogram equalization (QDHE)	78
3.19	Performance metrics obtained on DRIVE dataset using Recursively Separated and Weighted Histogram Equalization (RSWHE)	79
3.20	Performance metrics obtained on STARE dataset using Recursively Separated and Weighted Histogram Equalization (RSWHE)	79
3.21	Performance metrics obtained on CHASE dataset using Recursively Separated and Weighted Histogram Equalization (RSWHE)	80
3.22	Performance metrics obtained on DRIVE dataset using Matched Filter approach	84
3.23	Performance metrics obtained on STARE dataset using Matched Filter approach	84
3.24	Performance metrics obtained on DRIVE dataset using Hybrid Filter approach	85
3.25	Performance metrics obtained on STARE dataset using Hybrid Filter approach	85
3.26	Performance metrics obtained on DRIVE dataset using Line operator	86
3.27	Performance metrics obtained on STARE dataset using Line operator	86
3.28	Performance metrics obtained on DRIVE dataset using Gabor wavelet	87
3.29	Performance metrics obtained on STARE dataset using Gabor wavelet	87
4.1	Performance comparison based on Entropy	101
4.2	Performance comparison based on SSIM	101
4.3	Performance comparison based on PSNR	102
4.4	Performance comparison based on Euclidean distance	102

4.5	Average results for DRIVE database	102
4.6	Average results for STARE database	103
4.7	Average results for CHASE database	103
4.8	Comparison of average running time of various methods	103
5.1	The values of parameters employed for Gabor filter	112
5.2	The values of parameters employed for AdaBoost and LogitBoost classifiers	117
5.3	Comparative analysis of vessel segmentation techniques on DRIVE dataset	120
5.4	Comparative analysis of vessel segmentation techniques on STARE dataset	121
5.5	Comparison of average training time of various methods	122
5.6	Effect of patch size on various parameters in the case of DRIVE dataset using AdaBoost technique	122
5.7	Effect of patch size on various parameters in the case of DRIVE dataset using LogitBoost technique	123
5.8	Effect of patch size on various parameters in the case of STARE dataset using AdaBoost technique	123
5.9	Effect of patch size on various parameters in the case of STARE dataset using LogitBoost technique	123
5.10	Effect of number of orientations on various parameters for both DRIVE and STARE datasets	123
5.11	Effect of Gabor filter size on various parameters for DRIVE dataset	124
5.12	Effect of Gabor filter size on various parameters for STARE dataset	125

# **Chapter 1**

## **Introduction**

---

---

This chapter describes the need and motivation for the work and also gives the background understanding of retinal fundus photography, retinal vessel segmentation, and relation between blood vessels and prevalent diseases. Limitations of manual extraction, advantages of automatic extraction and challenges have also been presented in this chapter.

### **1.1 Introduction**

In all areas of the globe, illnesses are on the increase in the workforce and the aged population. Diabetic retinopathy, a vision-threatening disease caused by diabetes, is one of the leading diseases which affected a large population of about 126.6 million till 2011 which is further going to rise to 191 million by 2030 (Congdon, Zheng, & He, 2012), (Yau et al., 2012). Hypertension is another disease which is alarmingly rising and a number of people that are going to be affected by it are approximately 1.6 billion by the end of the year 2025 (R. Chen et al., 2013). Macular degeneration is also going to affect 196 million by 2020 which will further rise to 288 million by 2040 (Wong et al., 2014). Various diseases such as diabetic retinopathy, hypertension, macular degeneration, glaucoma, cardiovascular diseases, etc. can be diagnosed just by examining the retina. The retina is a thin tissue layer at the back wall of the eye. It contains photoreceptors i.e. light-sensitive cells. The light from the lens falls on these cells, which is converted by these cells to the neural signals and sent to the brain through the optic nerve connected to the retina. In order to determine the condition of the retina, fundus photography of the interior surface of the eye is done using a specialized low power microscope with a camera attached to it. The diseases can be recognized just by carefully inspecting the vascular structure of the retinal blood vessels in the retina. A change in the tortuosity, reflectivity or pattern of blood vessels indicates the presence of a disease. Swelling of the blood vessel indicates an advanced

stage of the disease. All these changes if detected early by prudently examining the retinal blood vessels may save a patient from vision-threatening diseases and high financial losses.

Manual extraction of the blood vessels from the retina is a very time-consuming process and can only be done by a trained professional under the supervision of the doctor. To help ophthalmologists with this complicated and tedious job, the need for automatic extraction of the blood vessel emerges. Automatic extraction not only helps in accurate segmentation of the blood vessels but also requires little time and effort. Development of vessel segmentation technique is highly challenging because of the presence of various factors such as improper illumination in the fundus image, varying intensity levels in the background of the image especially in images belonging to people of different ethnicity, blurriness in images because of the eye movement, low radiance, and noise.

## **1.2 Motivation**

In the modern society, with the advent of contemporary lifestyle, people suffer from greater incidence of a number of diseases. Retinal imaging was earlier used in the diagnosis of various eye related diseases such as diabetic retinopathy, retinal neoplasms, and macular degeneration etc. but with more advancements in medical science it has been observed that various other kind of diseases such as hypertension, cardiovascular diseases, leukemia, subacute bacterial endocarditis, and atherosclerosis etc. can also be detected by careful examination of the retina. Some diseases require the inspection of macula or fovea such as in the case of macular degeneration whereas for glaucoma optic nerve in the retina is needed to be inspected. All these diseases that can be diagnosed by retinal imaging are vision-threatening and if they are not diagnosed and treated early can lead to vision loss besides giving rise to other severe complications. An early detection of the disease is therefore very necessary for a successful treatment which may save the patient from losing the vision. In the context of this thesis, the diseases that are focused on are diabetic retinopathy, hypertension and various other diseases that can be detected by analyzing the vascular structure of the blood vessels in the retina.

Study suggest that retinal blood vessels provide a lifetime essence of genetic and environmental exposure and thus act as a useful risk marker for future systemic diseases (Cheung & Wong, 2009). Extracting vessels from the retina is a very interesting problem and a lot of research is being done in this direction at the moment but still it is an open area of research. It is very challenging to extract blood vessels from the retina because of various factors such as noise, improper illumination, low contrast and presence of various artefacts such as optic disc, macula and fovea etc. A lot of work has been done in this direction and an effort has been made by the researchers to accurately extract the blood vessels from the retina but still there is a space for improvement. To the best of the authors' knowledge very less work has been done towards handling improper and low illumination in the retina which has a significant effect on the accurate segmentation of the blood vessels from the retina. This work focuses on addressing the issue of low and improper illumination/radiance in the images. The second problem associated with the current techniques is that a lot of training in terms of number of samples is needed to be provided to the machine learning model prior to predicting a pixel in to either a vessel or a non-vessel pixel. Higher number of samples results in large training time. In this work, a sincere effort has been made to effectively train the model using lesser number of samples and still obtain better accuracy in terms of the extraction of the blood vessels.

### **1.3 Retinal fundus photography**

Specialized fundus cameras are used in taking the photograph of the rear (retina or fundus) of the eye as shown in Fig.1.1. The camera has a low power microscope with a flash attached to the camera. The term ‘angle of view’ is generally used to describe it and it can take images covering the retina between 30 to 50 degree. The eyes of the patient are dilated prior to capturing the image of the retina. Dilation helps in increasing the angle of observation of the retina. There are certain infrared cameras, called non-mydriatic camera, which can take the good retinal images without dilating the eye. The structures that can be seen on a fundus images are retinal vessels, macula, fovea, optic disk, and various kind of lesions.



Fig 1.1 Fundus camera being used to capture the image of the retina

### 1.3.1 Modes of examination

There are various modes for capturing the fundus image. They are as follows:

- Colour fundus imaging: In it, white light is reflected on to the retina and the image is captured in full colour.
- Red-Free fundus imaging: This technique is also called Infrared reflectance imaging as it uses infrared rays instead of the white rays. It utilizes green contrast filters to alter individual tones in monochrome images to block red wavelengths in order to have better contrast image as peak spectral sensitivity of the eye lies in yellow-green spectrum. It is comparatively easy to examine the vascular abnormalities or other abnormalities such as lesions, drusen or exudates etc. in the retinal images with high contrast.
- Angiography: In the case of angiography, a fluorescent dye is injected into the blood stream of the patient and a blue light is flashed into the retina. The fluorescein molecules absorb the blue light and start emitting light with higher wavelength. This light is captured to photograph the vascular flow within the retina to analyze if there is presence of some disease. This technique has a side effect in a sense that some patients get affected with nausea.
- Stereo-Imaging: In this technique, the camera is shifted laterally and images are taken at different angles. The 2D images are then combined to create a 3D image. A 3D image provides better information about the retinal surface.
- Hyperspectral Imaging: It uses the features of both spectroscopy and 2D object visualization obtained using digital imaging. In it, rather than analyzing just the

three colors, red, green, and blue, whole spectrum of light is analyzed. An image cube is formed from multiple images. Hyperspectral imaging provides additional diagnostic information but the down side is that it is technically immature.

In this context, the thesis work focuses on color fundus imaging which is vastly used in capturing the images of the retina.

## 1.4 Retinal Vessel Segmentation

One of the important subject of research in medical image analysis is the blood vessel segmentation in the retina as the blood vascular structure is highly crucial in the diagnosis and treatment of various prevalent and on the rise diseases especially in the field of ophthalmology, neurosurgery, and laryngology. Manual segmentation besides being complex and time consuming is also affected by inter-operator reproducibility and repeatability. Automatic segmentation of the blood vessels is thus very necessary to accurately extract the blood vessels from the retina in a timely manner. Also the results obtained using automatic segmentation techniques are repeatable and reproducible. Prior to vessel segmentation, the image has to go through various steps such as the preprocessing step, which is concerned with noise suppression or reduction, contrast enhancement, illumination equivalence, data normalization and conversion from colored image to gray scale image or extraction of the green channel from the colored image. As discusses earlier, there are different modes of fundus photography, so images are affected by different levels of noise, contrast, illumination etc. and thus are needed to be handled using different preprocessing techniques. Once the quality of the image is improved during preprocessing, vessels are extracted in the vessel extraction step. Vessel extraction can be done using either supervised techniques, unsupervised techniques or deep learning techniques. Vessel extraction is followed by the post-processing step in which the vessel extracted image is thresholded to obtain a binary image of only the retinal vessels. Post-processing also takes care of unwanted noise, artefacts, and may reconnect various small vascular segments to get a better overall vascular structure of the blood vessels. In this work, segmentation of the blood vessels is carried out using the supervised learning technique. In the supervised learning technique, feature extraction phase plays a very important part in the accurate

extraction of the blood vessels. Feature extraction can be done by either using global or local descriptors. Global features uses an entire image during the calculation of the features whereas local features are derived from local neighborhood of a pixel at multiple scales in the image. Local descriptors are more robust and sensitive than the global descriptors because they take into consideration the local conditions such as illumination, contrast etc. Feature extraction is followed by the classification phase, where each pixel in the image is classified into one of the class on the basis of the ground truth images, also called gold standard images.

## 1.5 Challenges in Retinal Vessel Segmentation

Retinal vessel segmentation is a very tedious task as many challenges are associated with it which are as follows:

- **Vessel width:** The vessels present in the retina do not have a fixed width, instead the width of the vessels varies between 1 pixel to more than 10 pixels. Therefore, developing a technique which can handle varying width of the vessels is very complicated. A highly flexible technique is needed to extract blood vessels with irregular width from the retina.
- **Noise:** Sometimes the images are affected by noise. Noise affects the overall accuracy of segmentation because during classification the noisy pixel is sometimes considered to be a vessel pixel which in reality is neither a vessel pixel nor a non-vessel pixel.
- **Low contrast:** Sometimes the images have low contrast and as a result differentiating between blood vessels and the background becomes very tough.
- **Low and improper illumination/radiance:** Almost all the images are affected by non-uniform radiance, with maximum radiance at the center of the image which decreases towards the boundaries of the fundus image. This happens because sometimes the patient might be sitting near or far from the camera during image acquisition or the light falling on the retina is not uniform. Non-uniform illumination affects the accuracy of the segmentation of the blood vessels.
- **Pathological images:** Images affected by diseases may contain certain artefacts such as lesions, hemorrhages, and hard and soft exudates etc. Apart from artefacts there are certain other non-vascular structures such as optic disc,

fovea, and macula etc. which are also present in the retina. Differentiating between these artefacts or vascular structures and normal blood vessels is a complex task as sometimes the areas affected by pathologies are sometimes treated to be belonging to the vessel class but they are not in reality.

All these challenges affect the extraction/segmentation accuracy of the technique. A technique should be robust such that it can accurately and efficiently extract the blood vessels from the retina by being either immune to these challenges or by handling these challenges.

## 1.6 Applications of Retinal Vessels

Various organs of the body can be checked for their functionality just by checking the retinal vessels as the vessels usually reveal the condition of the microvasculature (smallest vessels) of the organs of the body. Not all organs can be examined by inspecting the retinal vessels but it can definitely be done for some of the organs. Some of the areas where retinal vessels are used:

- **Cardiology:** Retinal vessel analysis (RVA) is a very new method that is used to diagnose chronic heart problem which leads to heart failure. The problem in the heart can be detected by evaluating the microcirculation in the retinal vessels (Nägele et al., 2018).
- **Sports Medicine:** It has been observed that various problems such as obesity and lack of physical activity i.e. lack of exercise has a negative effect on the retinal vessels resulting in the alteration in the retinal microvascular structure. A higher BMI (body mass index) or lack of fitness results in retinal arteriolar narrowing. Therefore, retinal vessel analysis helps in ascertaining if the sports person is fit or not. The level of fitness can be determined just by examining the degree of impairment in the vessels.
- **Ophthalmology:** Various eye diseases such as diabetic retinopathy, macular degeneration, glaucoma can be diagnosed just by a careful examination of the retinal vessels.
- **Neurology:** Recently retinal vessels have found themselves to be useful biomarkers in the diagnosis of neurological diseases such as Alzheimer disease (AD) or mild cognitive impairment (MCI). The degree of impairment in the

vessels can be used to check the progression of the disease (Querques et al., 2019).

- Biometrics: Each and every person has a unique pattern of blood vessels in the retina which can be used for uniquely identifying a person in biometric authentication. To make the identification more robust, bifurcation of the vessels and crossover points are also used alongside the blood vessels for more accurate recognition of the person.

## 1.7 Organization of Thesis

The thesis has been organized in the form of chapters as follows:

**Chapter 1** introduces to the motivation behind choosing this work. It gives a brief introduction to the retinal fundus photography and the various modes through which fundus photography can be done. It also discusses various phases required to achieve the objectives besides the challenges associated with the proposed work. In the end it also gives an insight into various applications where this work can be applied.

**Chapter 2** discusses the existing work in the field of image enhancement and segmentation. Research gaps have been identified and various objectives defined on the basis of it have also been presented along with the detailed methodology to achieve the objectives. The chapter finishes after giving a detailed explanation about various metrics and datasets used in the work.

**Chapter 3** contains the analysis of various image enhancement and segmentation techniques to identify the best one. Performance evaluation of the techniques is done both quantitatively as well as qualitatively and is presented in this chapter.

**Chapter 4** discusses the proposed retinal image enhancement techniques. Overall three novel enhancement techniques have been proposed to enhance the quality of retinal images which have been explained in detail in this chapter. The chapter finishes by discussing the results obtained both visually and objectively.

**Chapter 5** contains a detailed discussion on the proposed retinal blood vessel segmentation technique. The chapter also provides a brief explanation to dictionary learning and sparse coding besides Gabor wavelet which have been used for feature vector creation. AdaBoost and Logitboost classifiers have also been discussed in the chapter along with performance evaluation of the proposed technique.

**Chapter 6** provides the summary of the research work along with an insight into future scope and significance of the work.

## **1.8 Chapter summary**

In this chapter, initially an introduction to the need and motivation for this work has been discussed in detail along with the challenges affecting the automatic extraction of blood vessels from the retinal images. A brief discussion on retinal fundus photography along with the methodology to achieve the objectives has also been presented in this chapter.



# Chapter 2

## Literature Survey

---

---

### 2.1 Introduction

In order to analyze the blood vessels, the vessels need to be extracted from the retina. Accurate segmentation of the blood vessels from the retina depend on the quality of the image. Unfortunately getting a high quality image is not always possible because of various factors such as the distance of the imaging device from the retina, movement of the eye ball and improper expansion of the eyelids etc. As a consequence, the retinal images suffer from blurriness, low contrast, low and non-uniform radiance. Therefore preprocessing plays a crucial role in the efficient and accurate segmentation of the blood vessels from the retina as it enhances the quality of the retinal image. A higher quality image leads to better vessel segmentation (Javidi, Pourreza, & Harati, 2017). Various existing quality enhancement techniques to enhance the quality of the retinal images have been discussed in this chapter.

Besides, image enhancement techniques various vessel segmentation techniques have also been discussed in this chapter. Though main contributions of various segmentation techniques have been discussed in this chapter, some of the techniques which are more relevant to the proposed work are described in greater detail.

### 2.2 Image enhancement

The problem of non-uniform illumination was addressed by subtracting the background ( $I_B$ ) of each channel from the selected channel in (Al Shehhi, Marpu, & Woon, 2016). Gaussian blurring of the channel was done by a  $61 \times 61$  filter to obtain  $I_G$ . Shade corrected image was obtained by subtracting the background image from the Gaussian blurred image i.e.  $I_S = I_G - I_B$ . The author claimed that most of the artifacts such as optic disc were eliminated by this technique. Morphological based operation was

applied on the shade corrected image to further enhance the vascular structure. Black top hat image i.e. the final enhanced image, was obtained by subtracting from the shade corrected image the closing image.

Adaptive histogram equalization (AHE) was used in (Javidi et al., 2017) to enhance the contrast in the images. Several uniform histograms were computed for local regions to adjust the contrast but this algorithm suffered from the fact that there is over enhancement in some regions.

Contrast Limited Adaptive Histogram Equalization (CLAHE) was used to increase the contrast of the retinal images in (Azzopardi, Strisciuglio, Vento, & Petkov, 2015). In CLAHE, different histograms were generated for different parts of the image and each histogram was distributed uniformly to enhance the contrast of local parts of the image. Not only it enhanced the local parts but also the edges in every region of the image. The advantage of using CLAHE is that the amplification or the enhancement is limited which reduces the problem of noise amplification.

Bilateral filtering and Histogram stretching was applied to the green channel of the image in (Budai, Bock, Maier, Hornegger, & Michelson, 2013). Bilateral filtering reduces the noise while preserving edges in the image whereas histogram stretching increases the contrast of the image. The application of these algorithms helped in reducing the false positive that may occur in images.

In (Chaudhuri, Chatterjee, Katz, Nelson, & Goldbaum, 1989), a  $5 \times 5$  mean filter was employed to reduce the effect of the noise. Edges in the image were enhanced by using both the Sobel operator and morphological operator. The combination of sobel operator and morphological operator achieved significant improvement over using just the mean filter as the edges become considerably sharpened along with significant reduction in noise by using the combination.

Noise and various pathological artifacts such as lesions, exudates, optic disc, and fovea etc. were removed using the combination of binary output of Frangi's filter, morphological filter, and Vessel location map (VLM) from the green channel of the image. Contrast limited adaptive histogram equalization (CLAHE) was used to

increase the contrast of the image. To enhance the thin vessels and edges of thick vessels, high pass filtering was done using the high boost filter.

Gaussian smoothing was used to reduce the effect of spurious noise from the green channel extracted from the retinal image in (Lázár & Hajdu, 2015). A standard deviation of 1.0 was used to construct the Gaussian filter. ROI was extracted from the image so as to reduce the computational time and to exclude some unwanted noise at the boundaries.

Per-batch brightness and contrast normalization was performed in (Liskowski & Krawiec, 2016) to adjust the brightness of the image. All the channels were considered during enhancement and patches were extracted from all the channels. All the patches were normalized by subtracting mean from each patch and the result was divided by the standard deviation of the corresponding patch. Universal correlations were removed by multiplying the whitening matrix with the data matrix.

A three step process was applied in (Marín, Aquino, Gegundez-Arias, & Bravo, 2011) to preprocess the image in order to obtain a high quality image. In the first step, central light reflex in the vessel was removed by applying a 3 pixel disc shaped structuring element in the morphological opening operation. A very careful decision was taken while choosing the size of the structuring element as inappropriate disc size might result in the merging of vessels which are close to each other. In the second step, the problem of non-uniform illumination was addressed in the image. A  $3 \times 3$  mean filter was used to smoothen the salt and pepper noise. Further noise reduction was done using Gaussian filter with zero mean. Background image was obtained using a  $69 \times 69$  filter which was subtracted from the image obtained in the first step to get a uniformly illuminated image. Vessels were enhanced in the final step in order to clearly differentiate them from the background. A vessel enhanced image was obtained by applying the top-hat transformation on the homogenized image.

Median filter was applied on the green channel to reduce the noise in (Memari, Ramlı, Sarıpan, Mashohor, & Moghbel, 2017). The benefit of using the median filter is that edge information is always preserved while it eliminates the noise from the image. Contrast between the blood vessels and the background was improved using the

Contrast Limited Adaptive Histogram Equalization (CLAHE) algorithm. The advantage of CLAHE is its ability to improve contrast without over amplification of the noise. Morphological top-hat and bottom-hat operations were further applied to the image to further reduce the effect of noise and unwanted artifacts such as optic disc, and lesions etc. Radiance inhomogeneity was reduced using the Retinex theorem based on bilateral filter. Image background was removed by subtracting the homogenous image from the median filtered image.

In (Kolar et al., 2013a), a B-spline based radiance correction algorithm was applied to the images to remove non-uniform radiance. The algorithm was applied on the green channel of the image and was able to reduce the effect of most of the artifacts such as exudates, lesions, and hemorrhages etc. The technique not only adjusted the radiance problem but also improved the contrast of the image.

The problem of low contrast and improper illumination was addressed in (Oliveira, Teixeira, Ren, Cavalcanti, & Sijbers, 2016). Contrast stretching technique was applied on the green channel extracted from the image as it has highest contrast between the background and the vessels. The technique improved both the contrast as well illumination in the image. The combination of Gabor wavelet, Frangi's filter, and Matched filter was used to enhance the overall quality of the retinal image. The advantage of using Frangi's filter is that it is less sensitive to noise and as a result can easily differentiate between noisy pixels and the pixels that belong to vessels. Matched filter and Gabor wavelet are better at enhancing the thin vessels present in the retinal images. Further a combination of deformable models and Fuzzy C-means was also used for intensity normalization of the images. Weights were automatically computed using the Genetic algorithm.

The combination of Gabor wavelet and Contrast Limited Adaptive Histogram Equalization (CLAHE) was applied to the green channel of the image in (Qian Zhao, Hong Wang, Fang Wang, & Shih, 2014). CLAHE was used to obtain a local contrast enhanced image while reducing the effect of spurious noise. Gabor wavelet was further used to increase the contrast between the vessels and the background.

In (Rahebi & Hardalaç, 2014), a hybrid filter created using median filter and local mapping was used to enhance the quality of the image. Median filter was applied to remove the impulse noise from the image. Local mapping was done to reduce the effect of darkness in fundus images besides reducing the effect of foreground during the feature extraction step.

The green plane of the retinal image was first normalized and then enhanced in (Roychowdhury, Koozekanani, & Parhi, 2014). Intensity value of each pixel was squared and then re-normalized in the range [0,1]. Squaring the intensity values make the darker pixels belonging to vessels darker and brighter pixels of the background brighter resulting in an enhanced image.

In (N. P. Singh & Srivastava, 2016), the RGB image was first converted into a grayscale image which was then enhanced. Principal component based (PCA) algorithm was used to convert the RGB image into grayscale image. The advantage of using the PCA algorithm is its effectiveness in preserving the texture and color, done on the basis of linear computations. PCA based grayscale image was further enhanced using the Contrast limited adaptive histogram equalization (CLAHE).

An iterative algorithm was developed to reduce false detection of the pixels at the border of the fundus image in (Soares, Leandro, Cesar, Jelinek, & Cree, 2006). First, the pixels at the border of the region of interest (ROI) were determined and then the region outside the ROI was grown using the concept of 8-connected component. The region was grown iteratively. This helped in the false detection of the pixels.

A three step procedure to enhance the quality of images was proposed in (Vega, Sanchez-Ante, Falcon-Morales, Sossa, & Guevara, 2015). In the first step, the central light reflex present in the blood vessels was removed by applying the morphological opening operation on the green channel of the image. In the second step, background homogenization was done by convolving with Mean filter and Gaussian kernel. An eight pixel disc shaped structuring element was used in morphological top-hat operation to improve the contrast between the vessels and the background.

Matched filter was used to enhance the vessels in (Villalobos-Castaldi, Felipe-Riverón, & Sánchez-Fernández, 2010). The use of matched filter helped in the reduction of false detection of the blood vessels in the retinal images. The other benefit associated with the technique is that it is able to reduce the noise in the non-significant areas i.e. areas outside the region of interest (ROI) where there are no blood vessels.

Histogram equalization and Gaussian filtering was applied to enhance the image quality in (S. Wang et al., 2015). Histogram equalization was used to stretch the intensity values uniformly to increase the contrast between the vessels and the background. Noise was significantly reduced and illumination was made uniform with the help of Gaussian filtering. In depth working of histogram equalization is discussed in section 3.2.1.

An inverted green color channel was used in (Welikala et al., 2014) as vessels appear brighter in it than the background. Salt and pepper noise was reduced using the median filter. CLAHE was used to adjust the contrast in the local regions. A  $105 \times 105$  median filter was used to create an approximation which was subtracted from the inverted green channel to obtain a shade corrected image. An image containing circular objects was obtained using the morphological top-hat transformation. The image was then subtracted from the shade corrected image in order to get rid of the artifacts such as exudates, lesions, and micro aneurysms etc.

A combination of reconstruction with linear structuring element employed at different orientations and gray opening operation was used to pre-process the image in (Yang, Huang, & Rao, 2008). Two other methods created using the combination of Top-Hat transform and morphological opening and closing operations were also proposed in the work to further smoothen the pre-processed image.

In (Jiong Zhang et al., 2016), three filters were employed to enhance the quality of retinal images. Uniform illumination was achieved using the luminosity normalization technique. Erroneous detection obtained as a result of bright structures such as optic disc, and central vessel reflex was reduced by using a combination of geodesic and morphological top-hat transformation operations. Vessel profiles were enhanced using the Left invariant derivative (LID) filter on orientation scores (LID-OS). Complex

bifurcations as well as crossings were preserved using the LID filter. LID filter suffered from the fact that it was not able to align the vessels perfectly and this problem was addressed using the Locally adaptive derivative (LAD) filter on orientation scores (LAD-OS). The main benefit of using LAD is that it is robust and use lesser number of orientations to enhance the blood vessels.

## **2.3Vessel segmentation**

Manual blood vessel segmentation is a time consuming operation and lack reproducibility. Semi-automatic methods need the expert advice for the evaluation of results. Automatic segmentation methods can by themselves extract the blood vessels from the retina without the need or help of experts. In this chapter various broadly classified automatic vessel segmentation techniques have been discussed to provide comprehensive information about them by summarizing their advantages and limitations. Segmentation techniques can be classified into three different categories:

1. Deformable models
2. Vessel Tracking approaches
3. Machine learning approaches

### **2.3.1 Deformable models**

Surfaces or curves defined in an image domain that can move within the model itself under the impact of internal and external forces calculated from image information form deformable models. Generality forms the basis of the deformable models. A broad range of shapes and curves can be represented by deformable models and are therefore very useful in medical domain. Apart from medical domain there are various other applications of deformable models such as segmentation, edge detection, motion tracking, and shape modelling. Deformable models are suitable for the extraction of the blood vessels from the retina which have a high size and shape variability. The main downside about the deformable models is their high computational cost. There are two different types of deformable models and they differ on the basis of the numerical implementation and contour representation. The two types are edge-based and region-based models respectively.

### 2.3.1.1 Edge-based

Edge-based models are either geometric or parametric models. To manipulate the system characteristics, parametric models use solid, feature-based, and surface modeling instruments. One of the foremost imperative highlights of parametric modeling is that qualities that are interlinked consequently alter their features. Parametric models concentrate on and parameterize the measures to create a shape. In case of the blood vessels, the edge-based models suffer from changing blood vessel topology.

An active contour framework was used for vessel segmentation in (Cheng, Hu, Wang, Wang, & Tamura, 2015). 3D computed tomography followed by vessel boundary delineation was applied on the images. The strength of this technique lied with accurate detection of the contour of thin blood vessels. Another advantage associated with the technique is the avoidance of problematic regions in the image containing pathological regions, regions with multiple close vessels. The method performed well for low contrast images and was able to segment thin vessels effectively.

In (Lee & Lee, 2015), the combination of an active contour model and Kalman filter was used to detect blood vessels from the retinal images. Computed tomography was done for each image, and vessel boundaries were detected using contour model and Kalman filter was used to track the shape of the blood vessels. Multiple seed points were selected for the first slice and for subsequent slices the seed points were selected automatically. To make the boundary detection more accurate a block-search based estimation procedure was combined with the active contour model. The advantage of this technique is its resilience to shape deformation and it needs very less human intervention.

Gradient vector flow (GVF) was used in (Xu & Prince, 1998) to address the problem of low convergence towards vessel boundaries. GVF was computed using the binary or gray level map by diffusing their gradient vectors. In this work, the GVF was generalized by using two weighing functions to improve convergence to long and thin boundaries while other existing and desirable properties of GVF were kept unchanged.

In (Jin Zhang, Tang, Gui, & Liu, 2016), an active contour model based on parameter giving method was used to extract the blood vessels from the retinal images. Hessian vessel response was used by the proposed method to model the blood vessel edge. A local region pixel method was used to prevent the problem of local minima in which the contour usually falls. Non-vessel linear structures were filtered out in the post-processing step which was based on the context feature idea.

3D curvilinear structures were segmented using the image gradients symmetry in (M. W. K. Law & Chung, 2010). Both gradient symmetry as well as gradient anti-symmetry were considered to detect the object boundary. The abrupt intensity present along curvilinear structures was suppressed using the gradient symmetry. The structure boundary was located using the gradient anti-symmetry. The method performed well on natural as well as synthetic images of different modalities.

A novel framework for extracting centerlines in images (2D and 3D) for shape analysis was done in (Hassouna & Farag, 2005). Initially the seed point was selected automatically on the basis of the maximum Euclidean distance from the boundary of the vessel which then spread across the whole vessel region. Topological information was extracted in the form of extreme points using the nonlinear partial differential equation using level set method. Using the extreme points, centerlines were extracted. The advantage associated with the proposed method is that it is computationally less intensive and can handle complex topological structures and is robust towards boundary noise.

Local orientation of the gradient was used to create ring like patterns in (Moreno & Smedby, 2015). The technique took advantage of the spherical harmonics domain in which the ring like patterns have symmetrical properties. In the first step, gradients pointing outwards from the center were filtered out to extract bright blood vessels. For dark vessels, only those gradients which pointed towards the center were filtered out. Single vesselness feature was obtained by combining the two outputs.

### 2.3.1.2 Region-based

Region-based active contour model for vessel segmentation based on variational level set was presented in (Li Wang, He, Mishra, & Li, 2009). Mean and variance dependent Gaussian distributions were used to describe local image intensities. An iterative process estimating local intensity variances and means along with interleaved sets was used to achieve energy minimization. Noise and intensity inhomogeneity was handled by spatially varying functions. The specialty about the technique is that it is able to differentiate between regions with similar means but varying variances.

Although active contour models can extract the vessels from the retinal images but they are affected with intensity homogeneity. Therefore, a novel active contour based approach based on vesselness values and image intensities from local regions was proposed to define a Gaussian distribution based fitting energy for efficient segmentation of the blood vessels in (Lei Wang, Zhang, He, Chang, & Yang, 2015). A combination of level set formulation and the fitting energy along with regularization term was used to increase the accuracy of segmentation. The advantage associated with the technique is its ability to extract thin vessels with varying widths. The technique worked well not only with normal images but also pathological images.

A spatial constraint based Bayesian method for segmentation of the vessels was proposed in (Xiao, Adel, & Bourennane, 2013). The method is based on the fact that the posterior probabilities of the neighboring pixels are used to calculate the posterior probability of the pixel under consideration. A minimization energy model was used in the approach whose energy was minimized by using the level set approach.

An active contour model with weighted local variances was proposed to segment vessels from the images with low contrast and blurred boundaries in (W. K. Law & Chung, 2006). Weighted local variance that minimizes the orientation energy was used to estimate vessel boundary. The advantage of the proposed technique is its robustness to different kinds of noises.

Quadrature filters using edge and line detectors across multiple scales was used to extract vessels from the retinal images in (Läthén, Jonasson, & Borga, 2010). Well

defined linear structures were obtained by the method. The effectiveness of the technique was demonstrated by distinct edges produced. The approach worked well for both 2D and 3D images. The method proved to be robust in terms of boundary leakage and is computationally less intensive.

### **2.3.2 Vessel Tracking approaches**

Seed points play a very important role in vessel tracking approaches. Seed points are selected either manually or automatically and then on the basis of the initial point vessel centerlines are detected which are then grown to detect the full vessel region area. Vessel tracking approaches are especially important when the vasculature is connected because in connected vascular structure less number of seed points are needed in contrast to non-connected vascular structure which requires high number of initial seed points.

Model-based approaches are mostly used for 3D vessel segmentation. The most fundamental shape that the model assumes is the elliptical shape as it represents the vessel better especially the thin vessels but other different shapes can also be assumed. An initial seed point is used to define the initial orientation and position of the model which can be done by two ways either manually or automatically. Once this is done it is repeated again at every tracking step i.e. again the orientation and position of the model is selected that best matches with the image data in the local neighborhood. The main drawback of the model-based approaches is that they get affected with image inhomogeneity, noise and pathological areas affected as a result of diseases.

A second order tensor constructed using diffusion image modeling based directional intensity measurements was used in the segmentation of the vessels in (Cetin, Demir, Yezzi, Degertekin, & Unal, 2013). A single seed point was selected, using which the whole vessel tree was segmented by a branch detection approach. The framework extracted the vessel centerlines along with the thickness of the vessels and resulted in accurate segmentation of blood vessels.

A high order tensor based on cylindrical flux was presented in (Cetin & Unal, 2015). The approach easily modelled the branching points which always act a challenge while

segmenting the vessels from the image because the model usually works in antipodal symmetry which is affected by branching. The model can work in different tensor modelling scenarios. The high order tensor lies in 2<sup>nd</sup> sphere in case of 3D tensor modelling whereas it lies in 3<sup>rd</sup> sphere in case of 4D tensor modelling.

A new approach to detect vessel centerlines and provide local radius estimates along with multiple points on the blood vessel surface was proposed in (Yureidini, Kerrien, & Cotin, 2012). Successive cylinders are fit using RANSAC based modelling on the vessel surfaces. The method is good at identifying thin, small, touching and tortuous vessels.

A semi-automated technique based on Monte Carlo approach was used for vessel detection in (Cherry et al., 2014). The technique used various features such as vesselness, intensity, minimum spanning tree information to enhance low contrast blood vessels. Classification was done using Random forest classifier which made intelligent decision making in classifying the vessels. The advantage associated with the technique is that it is robust to noise. In the post-processing step, vessel pruning operation was applied to the results to remove isolated linear structures and improve overall accuracy of the technique.

A recursive algorithm to detect branches and bifurcations on the surface of the vessels using binary connected components was proposed in (Carrillo, Hoyos, Dávila, & Orkisz, 2007). Clustering algorithm using both intensity and geometric information was used to perform local segmentation. The algorithm increases inter class separability and decreases intra-class separability and inertia of the vessel pixels. The method was able to detect various bifurcations while avoiding spurious detections. The method proved to be fast and robust to noise.

Segmentation of small vessels was done using multiple hypothetical trajectories in (Friman, Hindennach, Kühnel, & Peitgen, 2010). The method exhibited improved performance especially in the areas of low contrast by traversing low contrast passages using hypothetical trajectories. The authors also proposed a novel framework to accurately extract the centerlines from the vessels. The tracking through the low

contrast passages was fast and robust enough that it can be used in combination with other segmentation techniques.

Centerline extraction and 3D tubular structure based vessel segmentation was presented in (H. Li, Yezzi, & Cohen, 2009). The method needed only one seed point initially and detected 3D multiple tubular surfaces and various centerlines at the same time. Initially the entire surface was represented as a 4D surface and each pixel of the 4D surface was represented using 3D spheres. A key point searching scheme was applied on the chosen 3D sphere during the front propagation process. All the key points were traversed using minimal action map to obtain global multi-branch structure.

A statistical tracking approach for the segmentation of the vessels was proposed in (X. Wang et al., 2012). The approach was able to extract linear structures with ring like cross-sections. Parameter adapting was done using the domain specific knowledge during the tracking process from the training data. The authors also proposed a branching algorithm to detect various branches present in the images. The method gave motivating results comparable to state-of-the-art techniques.

Oriented flux anti-symmetry (OFA) and optimal oriented flux (OAF) based on symmetry and anti-symmetry of the gradients was used to detect blood vessels in (Zeng et al., 2017). These approaches not only helped in detecting vessels but also their boundaries. Leaf node line growing and height ridge traversal techniques were employed to extract the centerlines from the vessels. The accuracy of segmentation was further enhanced by integrating intensity model in to the graph cuts and by applying distance voting mechanism.

Weighted geodesic distances were used to increase the number of key points repeatedly starting from a single seed point to extract the entire vascular structure in (D. Chen, Mirebeau, & Cohen, 2016). The approach took in to account the direction of tubular structures and did not suffer from boundary leakage problem as it used anisotropic Riemannian metric, the problem which occur is majority of the traditional geodesic distance based methods which used isotropic Riemannian metric. The key points were selected based on path score and the selection of the key points stopped once the

proposed criteria was fulfilled thus stopping the growth of the vascular structure. The proposed technique worked at finer scale and achieved good results.

### 2.3.3 Machine learning approaches

A lot of work has been done to extract the blood vessels from the retina using various types of techniques. Broadly, the machine learning techniques can be categorized into two main categories, supervised, and unsupervised techniques. Prior knowledge about the output in terms of manual annotations of the images, done by highly trained professionals, forms the basis of supervised learning. A large number of image feature vectors, along with their corresponding labels are subsequently used to train a classifier and cross-validation is done to estimate the loss. Once trained, the classifier can be used to classify each pixel of the query image. An extensive amount of training is needed for the classifier to accurately predict the label of the pixel. Supervised methods work by finding out a predictive modeling function that can efficiently categorize a pixel into one of the two classes.

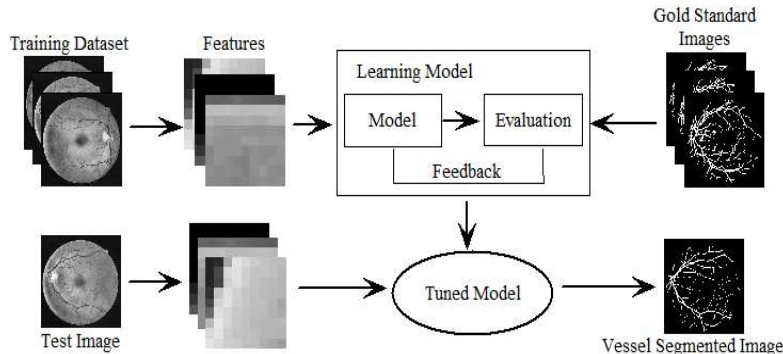


Fig 2.1 Block diagram of supervised technique

Recently, deep learning techniques have been used for the extraction of the blood vessels from the retina. Higher accuracy can be achieved using deep learning techniques. The accuracy of the deep learning techniques can be attributed to the employment of the vastly deep network architecture which can simulate very complex features present in the images. Despite the fact that the deep learning techniques are highly accurate they have certain limitations associated with them. The first and foremost is that they are computationally intensive and require a huge amount of time for training which may vary from days to weeks. Furthermore, executing the deep

learning algorithms, require very expensive high-performance processors (GPU's) which performs an inherently large amount of matrix operations in comparison to the typical algorithms. These factors i.e. large computation time and high cost may sometimes become a bottleneck in choosing the deep learning algorithms to solve a particular problem. On the other hand, unsupervised methods work without supervision making some important decisions based on the information present. They do not require previously annotated manual images. They have lesser computational complexity and higher speed than the supervised techniques.

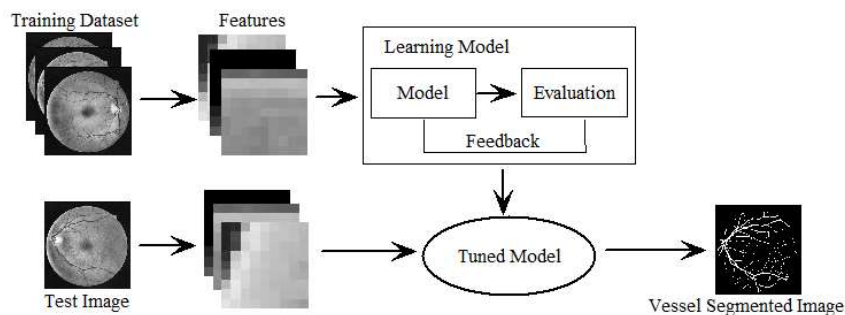


Fig 2.2 Block diagram of unsupervised technique

Generally, supervised methods are more accurate than unsupervised methods (Memari et al., 2017). As the proposed technique is a supervised machine learning technique, so a comprehensive review about various supervised machine learning techniques has been provided in this chapter.

### 2.3.3.1 Supervised Techniques

A ridge based segmentation method was proposed in (Staal, Abramoff, Niemeijer, Viergever, & van Ginneken, 2004) to extract the blood vessels from the retina. Image ridges were used to create line elements which were further used to partition image into patches. Feature vectors were computed using the combination of the patches and line elements. A combination of kNN classifier and sequential forward feature selection was used to classify pixels into vessel/non-vessel pixels. The authors claimed that their method was significantly better than the rule based methods. Two databases, DRIVE and STARE were used in the work. The training set of the DRIVE database contained 3 pathological images whereas the test set contained 4 pathological images. STARE

database contained 10 pathological images. Only green channel was used for the extraction of the vessels as it had highest contrast between the vessels and the background. The accuracy obtained with the method was 0.944 better than the second observer and it exhibited an area of 0.952 under the receiver operating characteristic curve (ROC).

A combination of intensity values and the Gabor wavelet output taken at multiple scales was used to create the feature vectors in (Soares et al., 2006). Gabor wavelet was chosen because of its ability to tune at specific frequencies. Classification of the pixels was done using Bayesian classifier with class conditional functions in order to obtain fast classification. False detection of vessels occurred in areas of high contrast such as optic disc, and lesions etc. The performance of the technique went down in the images that had non-uniform illumination/radiance. Another disadvantage associated with the method is its inability to detect thin vessels. The method's performance was evaluated on DRIVE and STARE datasets using three metrics, sensitivity (SN), specificity (SP), and accuracy (ACC). An accuracy of 0.9466 and 0.9480 was achieved on DRIVE and STARE datasets respectively. Gaussian mixture model (GMM) with varying  $k$  was applied on both the datasets and maximum area under the receiver operating characteristic curve (ROC) was obtained at  $k = 20$ . The area under ROC curve was 0.9614 for DRIVE and 0.9671 for STARE dataset. In depth working of this technique is discussed in section 3.3.4.

A novel method (Marín et al., 2011), based on the combination of grey level and moment invariant based features was proposed to construct a 7-D feature vector for pixel representation. The strength of the technique is its robust nature to different image conditions besides its efficiency and simplicity. Another important aspect of the proposed technique is its ability to process images with different resolutions. Central vessel reflex was removed by performing morphological operations using the disc shaped structuring element of 3 pixels diameter. Non-uniform illumination was addressed by applying background homogenization process. Prior to the homogenization process, salt and pepper noise was removed using a  $3 \times 3$  mean filter. Gaussian kernel was used to further remove the noise in the image. Vessel enhancement in the image was performed by applying top-hat morphological transformation

technique. The benefit of using top-hat operation is that vessels are enhanced while all the unwanted structures such as optic disc, and exudates etc. Classification of pixels was performed using a neural network (NN) scheme. The technique performed very well even when trained and tested on different datasets. Performance evaluation was done using five metrics, sensitivity (SN), specificity (SP), accuracy (ACC), positive predictive value (Ppv), and negative predictive value (Npv). An accuracy of 0.9452 and 0.9526 was obtained on DRIVE and STARE datasets respectively.

In (M.M. Fraz et al., 2012), an ensemble of bagged and boosted trees was used to classify the pixels of the image and obtain a binary vessel map. The 9-D feature vector was created from gradient orientations, line strength measures, Gabor filter responses, and morphological transformations. The strength of the technique lies with capability to handle pathological fundus images. The method does not involve any pre-processing step to avoid the removal of thin blood vessels. The important aspect of this technique is that the advance classification accuracy can be achieved in the training phase itself. Another advantage associated with this method is that a detailed analysis of various features depicting the amount of effect each feature has on the classification accuracy can be done in advance and on the basis of it only those features which have a significant effect on classification can be chosen. This not only increases the segmentation accuracy but also decreased the training and testing time. Ensemble classifier was used to classify the pixels into vessel and non-vessel pixels. The classifier was trained using 2000 weak learners and was trained on 275000 samples, out of which 200000 belonged to DRIVE database and the other 75000 belong to STARE database. Performance evaluation of the proposed technique was done using three metrics, sensitivity (SN), specificity (SP), and accuracy (ACC) on three databases, DRIVE, STARE, and CHASE. An accuracy of 0.9480, 0.9534, and 0.9469 was obtained on DRIVE, STARE and CHASE databases respectively.

Optical coherence tomography (OCT) data was used to extract the feature vectors in the work proposed by (Rodrigues et al., 2013). Forward selection approach was used to extract the features from the images. The feature vectors consisted of intensity based features, Gaussian based features, and local phase features. The classification of the pixels was done using support vector machine (SVM) classifier. Radial-basis-function

kernel was used alongside the SVM for better accuracy. The advantage of this method is its ability to work accurately on pathological images besides establishing itself as the starting technique in the direction of automatic 3D segmentation. In the case of pathological images, lower value of specificity was obtained. Performance evaluation was done using three metrics, sensitivity (SN), specificity (SP), and accuracy (ACC) on three different datasets, DS1, DS2, and DS3 (pathological images) with different level of resolution. An overall accuracy of 0.978, 0.974, and 0.974 was obtained on DS1, DS2, and DS3 datasets respectively.

Standard line operator and modified line operator were employed to generate binary vessel maps that were processed separately to create two feature sets in the method proposed by (Welikala et al., 2014). Crucial information was obtained from both the vessel maps created using different operators using dual classification approach. Two feature vectors were created using the morphological parameters from both the vessel maps and SVM classifier was applied on each of them. A combination of the two classification outcomes was then combined to produce the final outcome to classify a pixel into a vessel or non-vessel pixel. Performance evaluation was done using two metrics, Sensitivity and Specificity on MESSIDOR retinal database. Sensitivity of 0.862 and specificity of 0.944 was obtained on per batch basis and sensitivity of 1 and specificity of 0.90 was obtained on per image basis. In depth working of standard line operator is discussed in section 3.3.3.

In the paper (Rahebi & Hardalaç, 2014), the feature vectors were generated based on grey level co-occurrence matrix's specified characteristics, which were then used to train the neural network to classify the pixels. The grey level co-occurrence matrix contains the neighborhood transition intensities. Classification of the extracted features for vessels and non-vessels was done using the neural network (NN) classifier. Finally gaps in the blood vessels were filled in the post-processing step. Performance evaluation was done using four metrics, sensitivity, specificity, accuracy and area under curve (AUC) on DRIVE and STARE retinal databases. An average sensitivity of 0.6902, specificity of 0.9804, accuracy of 0.9527 and AUC of 0.9462 was obtained on the STARE database. In case of DRIVE database, an average sensitivity of 0.7365, specificity of 0.9707, accuracy of 0.9461 and AUC of 0.9564 was obtained.

Two binary images were generated, first by high pass filtering and second by morphological reconstruction from the green channel of the input image in (Roychowdhury et al., 2014). 8-D feature vectors constructed using first and second order gradients and neighborhood pixel intensities from both the images were used by Gaussian mixture model (GMM) to classify the pixels into vessel and non-vessel pixels. Post-processing combines missing portions of the blood vessels. The method has certain advantages associated with it such as low training and segmentation time. The method not only works well for normal images but also pathological images as the method outperforms most of the state of the art techniques in extracting blood vessels from the disease containing images. Performance evaluation was done using four metrics, Sensitivity, Specificity, Accuracy and Area under curve (AUC) on DRIVE and STARE retinal databases. An average sensitivity of 0.772, specificity of 0.973, accuracy of 0.951 and AUC of 0.969 was obtained on the STARE database. In case of DRIVE database, an average sensitivity of 0.725, specificity of 0.983, accuracy of 0.952 and AUC of 0.962 was obtained.

Lattice Neural Network with Dendritic Processing (LNNDP) was used for pixel classification and was compared with multilayer perceptron (MLP) and support vector machine (SVM) in the method proposed in (Vega et al., 2015). The advantage associated with this technique is that it requires no parameters. The feature vector dimensionality reduction was done using Hoteling T<sup>2</sup> chart which reduces the size of the feature vector from 7 to 5. Post-processing was done to remove noise and misclassified pixels to increase accuracy of the technique. The disadvantage associated with the technique is that as the training data is increased the performance of the technique degrades due to high variance among images. The advantage linked with this method is that it can create automatically as many dendrites as required during processing. Performance evaluation of the technique was done using five metrics, accuracy, sensitivity, specificity, F<sub>1</sub>Score, and Mathews Correlation Coefficient (MCC). An average accuracy of 0.9483, 0.9177, 0.9432, and 0.9336 was obtained using LNNDP, NN, SVM, and MLP respectively on the STARE database whereas an average accuracy of 0.9412, 0.9353, 0.9377, and 0.9073 was obtained on the DRIVE database.

Gumbel based matched filter was used in (N. P. Singh & Srivastava, 2016) to obtain a matched filter response (MFR) image which was further thresholded by an entropy based thresholding technique to obtain the binary vessel map. Length filtering was applied on the binary vessel map to remove the isolated and misclassified pixels by using 8-connected component neighborhood. To remove other unwanted artifacts, masking of the image was done using the mask generated from the image itself. Higher accuracy in terms of the extraction of the blood vessels was achieved because of the fact that gumbel based probability function better matched the cross-sectional profile of the blood vessels in the retina. Performance evaluation was done using three metrics, True positive rate (TPR), False positive rate (FPR), and accuracy on DRIVE and STARE retinal databases. In case of DRIVE database TPR of 0.7594, FPR of 0.0292, and accuracy of 0.9522 was obtained whereas TPR of 0.7939, FPR of 0.0624, and accuracy of 0.9270 was obtained on STARE database.

A combination of matched filter and AdaBoost classifier was used in (Memari et al., 2017) to extract blood vessels from the retina. A 35-D feature vector was constructed from intensity based features, Gray level co-occurrence based features, Gray level run length based features, and Gabor based features. Dimensionality reduction of the feature vector was done using the minimal redundancy maximal relevance method to reduce the size of the feature vector to 10-D. In the post-processing step all the unconnected regions comprising of less than 30 pixels are removed so as to increase the vessel extraction accuracy. The method provides high extraction accuracy with lesser artifacts and can work on pathological images. The proposed method achieved sensitivity of 0.8726, specificity of 0.9884, and accuracy of 0.9722 on DRIVE dataset whereas on the STARE dataset, sensitivity of 0.8085, specificity of 0.9798, and accuracy of 0.9514 was attained. The technique worked well on CHASE\_DB dataset as well and achieved sensitivity of 0.8192, specificity of 0.9591, and accuracy of 0.9482.

Discriminative dictionary learning (DDL) and sparse representation was used to extract blood vessels from the retina in (Javidi et al., 2017). The unique thing about this method is the construction of two separate dictionaries, where one dictionary is made from feature vectors corresponding to vessel pixels and the other dictionary is created from

feature vectors corresponding to the non-vessel pixels. The benefit associated with the technique is its ability to provide discriminative and reconstructive information about the retinal images. Vessel map is generated by applying Gaussian mixture model on vessel patches. To decide whether the pixels of the binary vessel map are 0 or 1 majority voting scheme is used. A sensitivity of 0.7201, specificity of 0.9702 and accuracy of 0.9450 was obtained on the DRIVE database whereas on the STARE database a sensitivity of 0.7780, specificity of 0.9653 and accuracy of 0.9517 was achieved.

To model the cross-modality transformation, a deep neural network was proposed to transform the fundus image into vascular map in (Q. Li et al., 2016). The neural network contains 5 layers with 400 units in the 3 hidden layers more than the units contained in the input layer which has 256 units. Training a neural network containing more units in the hidden layer is much more complex than training a simple neural network containing more units in the input layer. The model is trained using the backpropagation method. An annotated map of all the labels in a patch rather than the label of the center pixel of the patch was obtained using the neural network. The technique is robust in nature as it can be trained on different databases and still provides good overall accuracy. The other advantage associated with the technique is its strong inductive ability than the usual neural network models besides its effectiveness on pathological images. The proposed method attained sensitivity of 0.7569, specificity of 0.9816 and accuracy of 0.9527 was on the DRIVE database whereas on the STARE database a sensitivity of 0.7726, specificity of 0.9844 and accuracy of 0.9628 was achieved. On the CHASE\_DB database, sensitivity of 0.7507, specificity of 0.9793 and accuracy of 0.9581 was obtained.

A combination of second order derivatives of Gabor and Gaussian filters, along with dual Gaussian filters was used to generate feature vectors in (Muhammad Moazam Fraz, Rudnicka, Owen, & Barman, 2014). The strength of this approach lies with simultaneously extracting blood vessels from the retinal images as well handling central light reflex that occurs in the blood vessels. An ensemble classifier constructed from bootstrapped decision trees was used to classify the pixels into vessel/non-vessel pixels. The algorithm is fast than most of the other existing algorithms because of lower amount of training it needs. A generalized multi-scale filter was also employed to

minimize the false positives induced at crossovers of the vessels. The other advantage associated with the technique is its ability to handle both normal as well as pathological images that contains unwanted artifacts such as dark and bright lesions. The method achieved sensitivity of 0.7259, specificity of 0.9770, an accuracy of 0.9524, and Positive predictive value (Ppv) of 0.7732.

Two line detectors orthogonal in nature were used to create a feature vector corresponding to the target pixel for the extraction of the vessels in (Ricci & Perfetti, 2007). 12 different lines passing through the target pixel in 12 different orientations separated by  $15^0$  were used to calculate average grey values in all 12 orientations. The line that gave the highest grey value gave the direction of the vessel. Classification of the pixels into vessel/non-vessel pixels was done using linear Support Vector Machine (SVM) as comparative results were obtained on both linear as well as non-linear SVM and training a linear SVM in comparison to non-linear SVM was less demanding computationally. Performance evaluation was done on DRIVE and STARE databases. On the DRIVE database, an accuracy of 0.9595 and on STARE database an accuracy of 0.9646 was obtained.

A novel method based on semi-supervised radial projection approach to locate vessel centerlines was used to segment the thin blood vessels from the retinal images in (You, Peng, Yuan, Cheung, & Lei, 2011). Feature vector was constructed using the line strength. Thick vessels were extracted using the semi-supervised approach. Semi-supervised approach learned from manually annotated data and helped minimizing the detection of false vessel pixels. In case of radial projection, the peak of the projection indicates the presence of vessel. The output of the two approaches i.e. radial projection and semi-supervised approaches was combined to get the final vascular structure from the retina. The technique worked well for both the normal and pathological images. Still there are certain shortcomings of the technique such as vessel like noise, regions around optic disc, and several lesions are wrongly detected as vessels. The proposed method attained sensitivity of 0.7410, specificity of 0.9751, an accuracy of 0.9434 on the DRIVE database. On the STARE database, sensitivity of 0.7260, specificity of 0.9756, and an accuracy of 0.9497 was obtained.

Extreme Learning Machine (ELM) (Zhu et al., 2017) which is a feed forward neural network consisting of a single hidden layer used a 39-D feature vector comprising of features such as phase congruency, morphological features, local features, divergence of vector fields and Hessian values to extract the vessels from the retina. Isolated pixel set consisting of less than 30 pixels was considered as noise and was therefore removed in the post processing step. There are certain advantages associated with the approach such as the technique is robust to noise and is fast in segmenting the vascular structure. On the DRIVE database, sensitivity of 0.7140, specificity of 0.9868, an accuracy of 0.9607 was obtained. In case of RIS database, the values obtained were 0.7205, 0.9766, and 0.9628 for sensitivity, specificity, and accuracy respectively.

A 36-D feature vector consisting of features such as morphological features, local features, divergence of vector field, multiscale and multi-orientations features was used to train the classifier in (Zhu, Zou, Xiang, Cui, & Wu, 2016). Classification and Regression Trees (CART) along with Adaboost classifier were used to classify the pixels into vessel/non-vessel pixels. The strength of the method is its ability to extract vessels from pathological images containing lesions. In the post-processing step, the region containing less than 50 pixels was considered to be an isolated region and thus removed to increase the accuracy of the system. The proposed method attained sensitivity of 0.7462, specificity of 0.9838, an accuracy of 0.9618 on the DRIVE database. On the RIS database, sensitivity of 0.8319, specificity of 0.9607, and an accuracy of 0.9535 was obtained.

A combination of Gray voting and Gabor wavelets was used in (Dai et al., 2015) to preprocess the image. Gaussian mixture model (GMM) was used to extract the blood vessels from the preprocessed image where thin vessels were extracted using gray voting and main vessels were extracted using Gabor wavelets. In the post-processing step, the image was complemented as thin vessels or isolated fragments were clearly visible in the complemented image. All the fragments that were not associated with the vessels were removed on the basis of their shape from the complemented image. Sensitivity of 0.7359, specificity of 0.9720, and an accuracy of 0.9418 was obtained on the DRIVE database whereas on the STARE database, the values for sensitivity, specificity, and accuracy were 0.7769, 0.9550, and 0.9364 respectively.

Sparse representation based approach to extract vessels from the images was proposed in (B. Zhang, Karray, Li, & Zhang, 2012). Multiscale production of matched filter (MPMF) along with Sparse representation classifier (SRC) were used for the detection of blood vessels. MPMF filter, double thresholding, and scale production were used to detect pixels belonging to vessel centerlines which were then classified using the SRC. The method used two separate dictionaries where one dictionary contained vessel elements whereas other dictionary contained non-vessel elements in the classification process by sparse representation classifier. The method is good at extracting vessel centerlines even of small and thin vessels. The proposed method achieved False positive rate (FPR) of 0.0028, True positive rate (TPR) of 0.5766, and Positive predictive value (PPV) of 0.8467 on the DRIVE database.

In (Annunziata, Kheirkhah, Hamrah, & Trucco, 2015), highly irregular structures were segmented using a rotation, curvature and scale invariant filter. Classification was performed by Random Forest classifier. The technique was able to segment the vessel structure from low as well as high resolution images in the presence of unwanted artefacts. The benefit of using Random Forest is the low computational time in the classification process. Performance evaluation was done on three databases; IVCM, BF2D, and VC6. VC6 database was created from 3D images with very poor contrast and numerous artefacts.

The recent inception of deep learning algorithms for retinal vessel segmentation has been found to be very promising as they are highly accurate and can be used for both supervised and unsupervised learning. The accuracy of the deep learning techniques can be attributed to the employment of the vastly deep network architecture which can simulate very complex features present in the images. Among the diverse variants available for network architecture, convolutional neural networks (CNN) have been preferably used in the field of medical imaging.

A supervised deep learning technique in which the neural network was trained on a very large training sample data of approximately 4,00,000 samples was proposed by (Liskowski & Krawiec, 2016). All the samples were preprocessed with zero phase whitening, and contrast normalization. In order to obtain such large number of samples, the data was augmented by gamma corrections and geometric transformation. Rather

than classifying one pixel at a time multiple pixels were classified simultaneously. The method is resistant to the central vessel reflex problem and works well for pathological images. Training is computationally intensive as it requires approximately 8 hours to train the model on a single GPU. Performance evaluation was done using balanced-sp and no-pool-sp models. On balanced-sp models, sensitivity of 0.8149, specificity of 0.9749, and accuracy of 0.9530 whereas on no-pool-sp model sensitivity of 0.7811, specificity of 0.9807, and accuracy of 0.9535 were obtained for the DRIVE database. In case of STARE database, the values, 0.9075, 0.9771, and 0.97 were obtained on the balanced-sp model whereas on the no-pool-sp model, the values achieved were 0.8554, 0.9862, and 0.9928 for sensitivity, specificity, and accuracy respectively.

In (Fu, Xu, Lin, Kee Wong, & Liu, 2016), a multiscale CNN with side output layer and conditional random field-based approach was proposed to create a Deep Vessel network. The network consist of 3 layers where the first layer was used for discriminative representation, second for local companion output, and third layer for correlation of non-local pixels. The segmented binary map was obtained using Otsu's thresholding. The drawback of the technique is the large time consumption in the fine-tuning of the hyperparameters as it takes 2 days to perform optimizations and acquire the final values of the parameters on a single NVIDIA K40 GPU. Performance evaluation was done on three databases, DRIVE, STARE and CHASE\_DB. On DRIVE, sensitivity of 0.7603, and accuracy of 0.9523 were obtained whereas on the STARE database the values obtained were 0.7412 and 0.9585 for sensitivity and accuracy respectively. On the CHASE\_DB database, sensitivity of 0.7130 and accuracy of 0.9489 were obtained.

A supervised deep learning algorithm which used the combination of CNN and Random Forest (RF) for the classification of pixels was proposed in (S. Wang et al., 2015). CNN is used for feature learning and the learnt features were then fed in to the Random Forest classifier. The strong generalization capability of RF together with the scale and rotation invariance feature extraction by the CNN resulted in highly accurate segmentation of the blood vessels but training the algorithm is extremely time consuming and requires 8 days of training to find the right set of values for various hyper parameters using a set of 4 Intel Xeon CPUs with 256 GB of RAM. The approach

achieved an accuracy of 0.9767, sensitivity of 0.8173, and specificity of 0.9733 on the DRIVE database. On the STARE database, the values obtained for accuracy, sensitivity, and specificity were 0.9813, 0.8104, and 0.9791 respectively.

Despite the fact that the deep learning techniques are highly accurate they have certain limitations associated with them. The first and foremost is that they are computationally intensive and require a huge amount of time for training which may vary from days to weeks. Furthermore, executing the deep learning algorithms, require very expensive high-performance processors (GPU's) which performs an inherently large amount of matrix operations in comparison to the typical algorithms. These factors i.e. large computation time and high cost may sometimes become a bottleneck in choosing the deep learning algorithms to solve a particular problem.

The major drawback associated with deep learning techniques is that they are computationally intensive and require a huge amount of time and memory for training besides the expensive and dedicated graphical processors as discussed earlier.

### **2.3.3.2 Unsupervised Techniques**

The pioneering work under unsupervised techniques was done by (Chaudhuri et al., 1989). The technique exploited the fact, that the cross-sectional intensity profile of the blood vessels can best be represented by a 2-D Gaussian profile. Spatial and object properties based feature extraction operator was used to extract the piecewise segments of blood vessels in 12 different orientations separated by a uniform width from the retina. The technique performed well especially on fluorescein images of the retina but the drawback was high computational complexity.

In (Lam, Gao, & Liew, 2010), a multi concavity modeling approach was proposed in which the concavity measures were combined according to their statistical distributions to detect blood vessels from the retina. The technique converted the input image into perceptive space and worked well for pathological images which contain bright and dark lesions. Bright lesions were removed by using differentiable concavity measure whereas dark lesions were removed using line-shape concavity measures. The noise was taken care of by normalized concavity measures.

In the technique proposed by (Khan, Khaliq, Jalil, & Shahid, 2018), green channel was extracted from the retinal fundus image as it has a higher contrast between the background and the blood vessels. High boost filtering was applied on the green channel image to increase the contrast of the edges of the blood vessels. Another image was obtained by applying the Frangi filter on the enhanced image. Both the images were then thresholded using the improved thresholding technique to obtain the binary images. Post processing was then applied to remove isolated pixels and gaps were filled between vessel pixels to obtain Vessel location maps (VLM). These VLM's were then ANDed to obtain the final binary image of the retinal vascular structure. The technique is time efficient as it does not require ground truth images for training the model. Evaluation was done on three databases namely; DRIVE, STARE and HRF.

Key points which represent scale specific features were used to learn the parameters in (L. Zhang, Fisher, & Wang, 2015) to extract the blood vascular structure from the fundus images. SIFT algorithm was used to extract the key points by searching for local maxima using the parameterized Gabor filter bank. A texton dictionary was built using the k-means clustering algorithm based on the seed points derived from the key points.. The advantage of using texton dictionary is that it mitigates the variability that arises between intra and inter observers. Simple Neural Network (NN) was used to classify the pixels into vessel/non-vessel pixels. Performance evaluation was done on the DRIVE database.

Directional processing of each and every pixel in the image was performed in (Lázár & Hajdu, 2015). Various intensity values along different orientations between  $0^0$  to  $180^0$  separated by  $6^0$  were considered. 1-D multiscale matched filter (MMF) which is symmetric in nature along with 1-D grayscale bottom-hat operation was applied to obtain directional response vector maps (DRVM). Statistical measures such as mean, standard deviation, and maximal value were used to obtain the score of each and every pixel from the response vector maps. Both the score map and DRVM were used in the region growing approach to extract the blood vessel from the retina. The specialty of the technique is its ability to exclude seed points which belong to unwanted artifacts such as macula, fovea, lesions, or hemorrhages etc. The method's performance was evaluated on both DRIVE and STARE databases.

A novel technique based on trainable COSFIRE filters for vessel segmentation was proposed by (Azzopardi et al., 2015). A geometric mean calculated from the difference of Gaussians was used to select various orientations of the blood vessels. A rotational invariant filter, B-COSFIRE, was presented and used in the extraction of the blood vessels. Two variants of the filter, symmetric and asymmetric B-COSFIRE filters were used to detect the blood vessels and the outcome of two was combined to obtain the final vascular structure of the vessels. The strength of the technique is its robustness towards noise besides it can also be used to detect crossover and bifurcations in the vascular structures. The technique was applied on DRIVE, STARE and CHASE\_DB databases.

A multiresolution framework based on hysteresis thresholding to extract blood vessels was proposed by (Budai et al., 2013). Images with lesser resolutions were created from the original image to reduce the computational time while calculating the Hessian matrix for a small neighborhood in comparison to the larger neighborhood. Subsampling and low pass filtering was used for the reduction in the size of the images. In the post-processing step, the holes created by the central reflexed were filled. The advantage associated with the technique is its less computational complexity and robustness to noise and intensity changes between pixels of an image. The approach was applied to DRIVE, STARE datasets.

In (Qian Zhao et al., 2014), level set implementation in combination with the region-based contour model was used in parallel to the region growing method to extract blood vessels. The output of both the methods was used to generate the final binary vessel map. The purpose of using the combination of both the methods is their ability to detect both thin and thick vessels where thin vessels were detected by region growing method and thick vessels by level set method. The disadvantage associated with this method is its ineffectiveness to detect vessels in pathological images. Performance evaluation of the technique was done on publicly available DRIVE and STARE databases.

A 3-stage vessel extraction method was proposed by (Roychowdhury et al., 2014). In the first stage, two images, one as the output of high-pass filtering and other as the output of morphologically obtained image were obtained. Major vessels from the common areas of the both the images were then obtained as the last step in the first

stage of segmentation. In the second stage of extraction, all other pixels were extracted using Gaussian mixture model (GMM) using 8-D feature vectors which consist of intensity and gradient values. These features were selected using the maximal relevance and minimum redundancy (mRmR). The strength of the method is its low training and classification time since the thick vessels are extracted using the unsupervised technique and thin vessels by a supervised approach. Three databases, DRIVE, STARE and CHASE\_DB were used for performance evaluation of the proposed technique.

Multi-scale graph based segmentation was performed in (Al Shehhi et al., 2016). Vessel like patterns were extracted using the Gestalt principles such as continuity, closure, similarity, and proximity etc. Graph based features were used to detect non-neighbor nodes which act as part of the connected components so as to complete the vessel pattern contour. Low pass Gaussian-blurring was used to remove the noise in the fundus images. The approach lacks in finding the thin vessels from the retinal images. The drawback of this approach is its high computational time it takes in analyzing the graphs. Other algorithms used in this approach such as Dijkstra's algorithm and connected labelling also further increases the computational complexity of the approach.

Combination of Frangi's filter, Matched filter, and Gabor wavelet were used to extract blood vessels in (Oliveira et al., 2016). The combination was used to improve the vessel segmentation results. Frangi's filter is not affected by noise whereas Matched filter and Gabor wavelet are good at detecting thin vessels. The disadvantage associated with the technique is although the technique is good at detecting thin vessels but it is not good enough to detect majority of the thin vessels and vessels from the areas which are close to the border of the retina. The technique also proposed some new quantification metrics and showed their superiority over the existing evaluation metrics.

In (Jiong Zhang et al., 2016), new filters; Left invariant rotating derivative (LID) and Locally adaptive derivative (LAD), based on 3-D rotating frames were proposed. Eigen analysis of the Hessian matrix was used to create the LAD filter to make it adaptive to various line structures. 3-D orientation score was obtained from a 2-D image. LID and LAD filters were then used for multiscale filtering and the output was then reflected back in to the 2-D plane. Vessels at different orientations were unscrambled to their

corresponding orientation planes and segmentation was achieved. The technique works well for cases like closely parallel and tiny vessels, crossings, and central arterial reflex, etc. The technique has a very low computational complexity.

Cauchy distribution based filter was proposed in (Zolfagharnasab & Naghsh-Nilchi, 2014) to improve the accuracy of blood vessel segmentation in retinal images. The strength of the Cauchy filter is that it is more flexible than Gaussian filter and can fit the vessels better than other existing filters. It was further proposed in the paper to use the combination of matched filter and Cauchy distribution for better extraction of the blood vessels from the retina.

In (B. Zhang, Zhang, Zhang, & Karray, 2010), a novel approach First order derivative of Gaussian based matched filter (MF-FDOG) was used to extract the blood vessels from the retina. Response to matched filter was thresholded with a value selected on the basis of the FDOG response of the image. MF-FDOG is an improvement over simple matched filter as it reduces false edge detection besides extracting the thin vessels from the image. The technique can easily differentiate between vessel structure and non-vessel structures and is equally efficient on both normal as well as pathological images. Higher accuracy was achieved using multi-scale filters to extract both thin and thick vessels. Noise reduction was done using geometric features based post-processing.

A fast and efficient approach based on entropy and gray level co-occurrence matrix (GLCM) was used to extract the vascular map in (Villalobos-Castaldi et al., 2010). A statistical feature, calculated from GLCM was used as a threshold value to obtain the final binary vascular structure.

Green channel was used in (Kolar et al., 2013b) for the segmentation of the blood vessels using the Matched filter (MF) approach. Based on different cross-sectional intensity profiles corresponding to varying vessels widths ranging from thinnest to thickest blood vessels, 5 different filters were convolved with the image at 12 different orientations. The maximum response for each pixel was considered for classification of the pixel to generate a fused parametric image. This parametric image was then

thresholded to obtain the binary vessel map. Noise, isolated pixels, and unwanted artifacts were removed in the post-processing step.

A novel approach for vessel segmentation and measurement was proposed in (Bankhead, Scholfield, McGeown, & Curtis, 2012). With the tuning of only a few parameters, this technique can be applied on a variety of images such as low resolution, high resolution, and angiogram images. Vessel segmentation was done using wavelet coefficients thresholding and centerline extraction using graph based approach. Extracted vessels along with the calculated diameter of the vessels helped in achieving higher accuracy with lesser error rate. The technique enabled the rapid calculation of diameters throughout each vessel's length rather than at particular points of interest, resulting in more fine-grained outcomes than would be feasible manually or using computer-assisted interactive software. The technique is computationally less intensive in comparison to most of the other state of the art unsupervised methods.

An infinite active contour model to detect blood vessels was used in (Zhao, Rada, Chen, Harding, & Zheng, 2015). Local phase enhancement and intensity information were used for the segmentation of the vascular structure. The advantage of using local phase enhancement is better at preserving vessel edges whereas intensity information guarantees the extraction of correct features. An accurate vessel map can be obtained using the phase map while reducing the detection of potential outliers by using the intensity information. The approach showed good performance on both the fundus and angiogram images and worked well on normal as well as pathological images.

In (Yang et al., 2008) a hybrid approach was used for the extraction of the blood vessels. The hybrid approach is a combination of morphological approach and fuzzy clustering algorithm. Vessels were enhanced by the morphological algorithm by suppressing unwanted artifacts such as optic disc, fovea etc. Segmentation was done by applying the fuzzy clustering algorithm on the vessel enhanced image. Noise and weak edges were reduced by a purification procedure in the post-processing stage. The approach worked well only on normal images and pathological images were not taken in to account.

An adaptive local thresholding framework based on multithreshold probing scheme was used to extract the vascular structure from the retinal fundus images in (Jiang & Mojon, 2003). The object of interest related information was utilized to design the application dependent method. This application dependent approach was used to detect the vessels and is applicable to various other kinds of tasks such as the detection of micro aneurysms, lesions, and calcification in mammograms.

A new framework consisting of 3 components: local phase based vessel enhancement, retinex based inhomogeneity correction, and graph cut based active contour segmentation was used for the extraction of blood vessels from the retina in (Zhao, Liu, Wu, Harding, & Zheng, 2015). The low contrast between the blood vessels and the background along with inhomogeneity correction were taken care of by the retinex algorithm, vessel edges were preserved by the local phase algorithm, and graph cut method was used for the effective and efficient extraction of the blood vessels from the fundus images. The retinex algorithm specifically used bilateral filter because of the fact that it is a smoothing filter which can preserve edges. The technique worked well for both normal and pathological images.

## 2.4 Research Gaps

From the literature survey, it is observed that a lot of work has been done on vessel segmentation but still it is an open area of research because of various factors. Various factors such as noise, improper illumination, low contrast, and various artifacts such as optic disc, macula and fovea etc. make the extraction process very tedious. To the best of the authors knowledge, a lot of effort has been made by the researchers to extract the blood vessels from the retina but very less work has been done on the above said factors that affect the accuracy of segmentation of the blood vessels from the retina. Present research work focuses on addressing the issue of low and improper illumination in the images. The other problem is that a lot of samples are needed to be provided to the model for training in order to classify a pixel in to either a vessel or a non-vessel pixel. Higher number of samples results in large training time. In this work, a set of new features is proposed that can effectively train the model using lesser number of samples and still obtain better accuracy in terms of the extraction of the blood vessels. Another factor that affects the accurate segmentation of the blood vessels is the false

detection of the artefacts and the presence of lesions, exudates etc. in images. This work can handle pathological images that contain lesions etc. and can also differentiate between artifacts and actual blood vessels.

## 2.5 Research objectives

Based on Research Gaps following research objectives have been defined:

1. Analysis of different segmentation techniques used to extract blood vessels from retinal images.
2. To perform retinal image enhancement using image pre-processing techniques.
3. To develop an improved retinal blood vessel segmentation technique for the extraction of blood vessels.
4. To perform comparative analysis of various techniques both quantitatively as well as qualitatively.

## 2.6 Research Methodology

The following methodology was used to accomplish the objectives and obtain improved results in the research work.

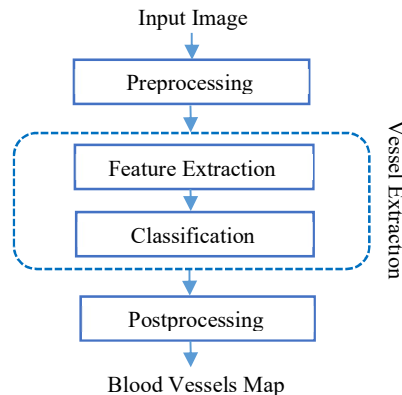


Fig 2.3 Flowchart of Blood Vessel Segmentation process

### 2.6.1 Pre-processing

Majority of the images suffer from low quality and are noisy in nature. In this step, the image quality is enhanced using a pre-processing technique to get a high quality image with reduced noise, better contrast, and uniform illumination.

### **2.6.2 Feature extraction**

Feature extraction is an important step for efficiently extracting the blood vessels from the retina. In this phase, features are extracted for each and every pixel of the image to create feature vectors. The choice of features plays a significant role in the accurate extraction of the vessels from the retina.

### **2.6.3 Classification**

In this step, the model is trained using the feature vectors created during feature extraction phase. A set of feature vectors and corresponding labels is provided to the classifier which learns weights by performing various optimizations. After training, the classifier will be able to classify the pixels of the retinal images into vessel and non-vessel pixels.

### **2.6.4 Post-processing**

Post-processing deals with the operations that are performed once the classification phase is over. All the isolated pixels or a set of a small number of pixels that have been incorrectly classified as vessel pixels are removed from the image obtained in the classification step so as to increase the overall accuracy of the system.

## **2.7 Image Quality Metrics**

The proposed techniques have been implemented in MATLAB. The performance evaluation of the techniques has been done both quantitatively and qualitatively. The algorithmic performance of the proposed methods has been measured in terms of Entropy, SSIM, PSNR and Euclidean distance. The metrics are defined as follows:

### **2.7.1 Entropy**

Entropy (Kim & Chung, 2008) measures the information content of the image. Mathematical equation for entropy is:

$$E[p] = - \sum_{j=0}^{L-1} p(j) \log_2 p(j). \quad (2.1)$$

where  $E[p]$  is the entropy,  $L$  is the number of intensity levels and  $p$  contains the normalized histogram counts.

### 2.7.2 Structure Similarity Index Measure (SSIM)

Structure similarity index measurement (SSIM) (Sim, Tso, & Tan, 2007) determines the change in the structural information of the image and is represented as following:

$$SSIM(x, y) = \frac{(2\mu_x\mu_y + c_1)(2\sigma_{xy} + c_2)}{(\mu_x^2 + \mu_y^2 + c_1)(\sigma_x^2 + \sigma_y^2 + c_2)}. \quad (2.2)$$

where  $\mu_x$  and  $\mu_y$  are the average of  $x$  and  $y$  respectively.  $\sigma_x^2$  and  $\sigma_y^2$  are variance of  $x$  and  $y$  respectively.  $\sigma_{xy}$  is the covariance of  $x$  and  $y$ .  $c_1$  and  $c_2$  are the two variables to stabilize the division with weak denominator where  $c_1 = (k_1 L)^2$  and  $c_2 = (k_2 L)^2$ ,  $k_1 = .001$  and  $k_2 = .003$ .  $L$  is the dynamic range of pixels.

### 2.7.3 Peak Signal to Noise Ratio (PSNR)

Peak signal to noise ratio (PSNR) (Chan, Chung-Wa, & Nikolova, 2005) is the maximum intensity that a signal can have and it is denoted as:

$$PSNR = 10 \log_{10} \frac{255^2}{\frac{1}{MN} \sum_{i,j} (g_{i,j} - f_{i,j})^2}. \quad (2.3)$$

where,  $g$  is the enhanced image and  $f$  is the original image.  $M$  and  $N$  denote number of pixels row-wise and column-wise respectively.

### 2.7.4 Euclidean Distance

Euclidean distance  $d_E(x, y)$  (Liwei Wang, Zhang, & Feng, 2005) is given by

$$d_E^2(x, y) = \sum_{k=1}^{MN} (x^k - y^k)^2. \quad (2.4)$$

$x^k$  and  $y^k$  are intensity values at corresponding locations  $(k, l)$  of the two images  $x$  and  $y$ .

## 2.8 Image segmentation metrics

The proposed segmentation techniques have been implemented in MATLAB. The performance evaluation of the techniques has been done both quantitatively and qualitatively. The algorithmic performance of the proposed methods has been measured in terms of Sensitivity, Specificity, and Accuracy. The metrics are defined as follows:

### 2.8.1 Sensitivity

Sensitivity (SN) is the ratio of correctly classified vessel pixels,

$$SN = \frac{TP}{TP + FN} \quad (2.5)$$

where TP is the number of correctly classified vessel pixels and FN is the number of incorrectly classified non-vessel pixels.

### 2.8.2 Specificity

Specificity (SP) is the ratio of correctly classified non-vessel pixels,

$$SP = \frac{TN}{TN + FP} \quad (2.6)$$

where TN is the number of correctly classified non-vessel pixels and FP is the incorrectly classified vessel pixels.

### 2.8.3 Accuracy

Accuracy (Acc) is the ratio of the correctly classified vessel and non-vessel pixels,

$$Acc = \frac{TP + TN}{TP + FN + TN + FP} \quad (2.7)$$

## 2.9 Datasets

To analyze the performance of the proposed methods, images from publicly available databases Digital retinal images for vessel extraction (DRIVE) (Staal et al., 2004), Structured analysis of the retina (STARE) (Hoover, Hoover, A;Kouznetsova, V;Goldbaum, & Hoover, 2000), Child Heart and Health study in England (CHASE\_DB1) (Muhammad Moazam Fraz et al., 2012) and Open access series of imaging studies (OASIS) (Marcus et al., 2007) have been used. DRIVE contains 40 colored fundus images taken by a Canon CR5 camera at  $45^0$  field of view (FOV) with a resolution of  $565 \times 584$  with 8 bits per color plane. The dataset is divided into test and training datasets with 20 images in each dataset. Training dataset contains manual annotations by an expert ophthalmologist whereas the test dataset contains annotations by two experts. STARE dataset contains 20 images of size  $700 \times 605$  with 8 bits per color plane, out of which 10 are pathological images captured at  $35^0$  FOV. There are no separate training and test datasets in the STARE database. CHASE\_DB1 database contains 28 retinal images of the children taken using the NM-200D fundus camera. Images were recorded in low light conditions using an illumination rating of 3. OASIS dataset contains both cross-sectional as well as longitudinal MRI images of young, middle aged, demented and non-demented older adults. The cross-sectional dataset contains images of 416 subjects whereas longitudinal dataset contains images of 150 subjects. While complete retinal databases have been used to find the overall results, only two images have been used from the OASIS database just to check the degree of robustness of the proposed enhancement techniques.

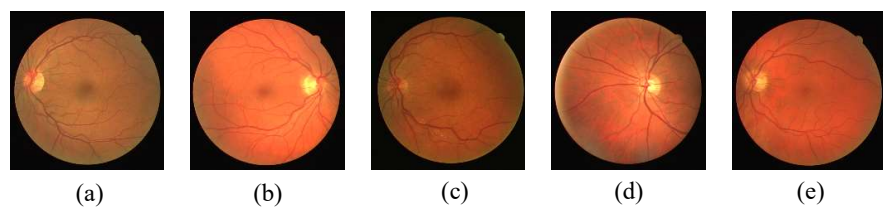


Fig 2.4 Sample images of DRIVE dataset

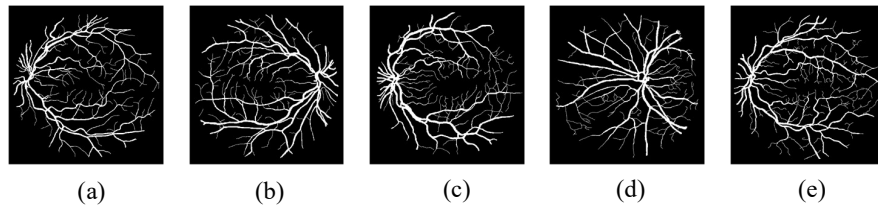


Fig 2.5 Manually annotated corresponding sample images of DRIVE dataset

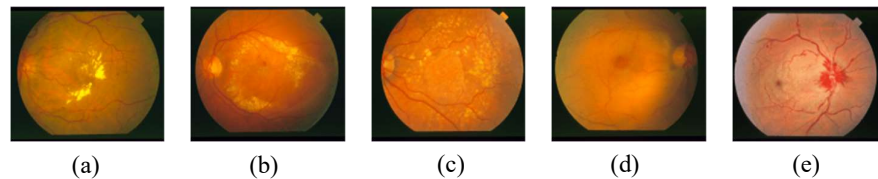


Fig 2.6 Sample images of STARE dataset

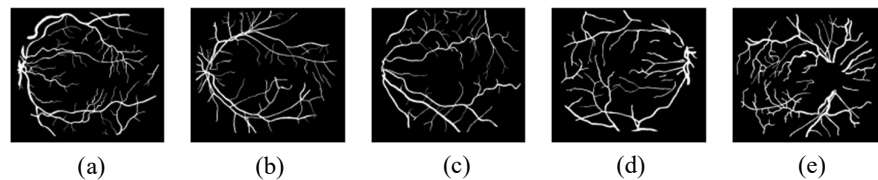


Fig 2.7 Manually annotated corresponding sample images of STARE dataset

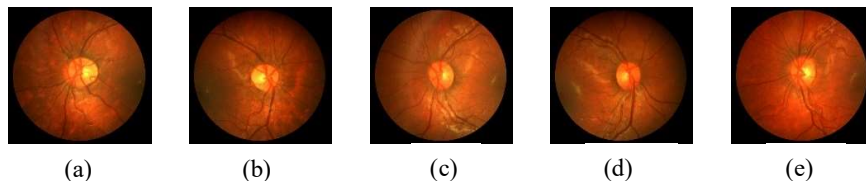


Fig 2.8 Sample images of CHASE dataset

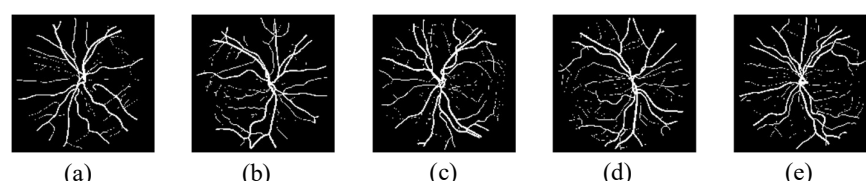


Fig 2.9 Manually annotated corresponding sample images of CHASE dataset

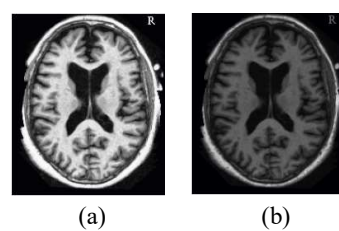


Fig 2.10 Sample images of OASIS dataset

## **2.10 Chapter summary**

An extensive study of both image enhancement and blood vessel segmentation methods has been presented in the chapter. The research gaps have been discussed and on the basis of the gaps the objectives of research work have been defined. A brief introduction to research methodology to achieve the objectives has also been discussed in the chapter. Depending on the relevance and need, some of the techniques which are more related with the proposed techniques have been described in greater detail than other techniques.



# **Chapter 3**

## **Comparative Analysis of Image Enhancement and Segmentation Techniques**

---

---

### **3.1 Introduction**

Image enhancement is a technique to enhance the quality of the images in order to make them suitable for processing. Interpreting an enhanced image is comparatively easier than the original image. Some common routines for enhancing the quality of images are contrast enhancement, spatial filtering, density slicing, image sharpening, and smoothing. In contrast enhancement, a linear transformation function is applied to expand the gray level range of the original image to cover a wider range of uniform values to use the whole available dynamic range of the output devices. Various natural features such as joints, branches, edges, shear zones etc. are enhanced in spatial filtering. In the case of density slicing, the range of gray values is divided into subgroups and different colors are assigned to the subgroups. Image sharpening focus on enhancing the high frequency components in an image whereas image smoothing deals with suppressing high frequency components. These image enhancement techniques can be applied to a variety of applications in order to improve their quality.

Segmentation deals with the extraction or segmentation of region of interest (ROI) from an image. In it an image is divided into various segments and the required segments are extracted from the image for further processing or use. Specifically, in image segmentation, similar pixels are assigned same label such that all the pixels sharing similar properties such as intensity, color, texture are grouped together. Every segment has its own set of characteristics and is significantly different from other segments. Segmentation can be done using both supervised and un-supervised techniques. The working of both the techniques has been discussed earlier.

In this chapter, a comparative analysis of both the enhancement and segmentation techniques has been performed with application towards retinal images.

## 3.2 Retinal image enhancement techniques

### 3.2.1 Histogram Equalization (HE)

Histogram equalization (Yu Wang, Qian Chen, & Baeomin Zhang, 1999) is the process of improving the contrast of an image by using the histogram of the image. There is a drastic change in the contrast of an image especially when the image has low contrast and most of its intensity values are confined to a smaller region in a histogram. With equalization the intensity values are uniformly distributed throughout the histogram.

#### **Basic steps for Retinal image enhancement using histogram equalization (HE)**

Step 1: Read the input image and convert it into grayscale image.

Step 2: Calculate the histogram of the image.

Step 3: Calculate the probability of occurrence of intensity value,  $i$  in the image

$$p_x(i) = \frac{n_i}{n}, 0 \leq i \leq 255 \quad (3.1)$$

where  $n_i$  the number of pixels with intensity is value  $i$  and  $n$  is the total number of pixels in the image.

Step 4: Calculate the cumulative distribution function (CDF) for different probabilities obtained in step 3.

$$cdf_x(i) = \sum_{j=0}^i p_x(j) \quad (3.2)$$

Step 5: Normalize the intensity values as follows to obtain an equalized image

$$img\_n = round(minval + (maxval - minval) \times cdf(img)) \quad (3.3)$$

where  $minval = 0$ ,  $maxval = 255$  and ‘img’ is the test image.

### 3.2.2 Brightness preserving bi-histogram equalization (BBHE)

Histogram equalization can improve the contrast of an image but the drawback associated with it is that it also increases the brightness in the image which happens due to the flattening property of the histogram obtained by applying the equalization process. Brightness preserving bi-histogram equalization (BBHE) (Yeong-Taeg Kim, 1997) addresses the problem of brightness by extending the histogram equalization technique.

#### **Basic steps for Retinal image enhancement using brightness preserving bi-histogram equalization (BBHE)**

Step 1: Read the input image and convert it into grayscale image.

Step 2: Calculate the histogram of the image.

Step 3: Find the mean,  $X_m$  of the image and split the histogram into two sub-histograms  $h_l$  and  $h_u$  at the obtained value of mean.

$$X_m = \frac{1}{M \times N} \sum_{i,j} img \quad (3.4)$$

$$h_l = x_i, 0 \leq i \leq X_m \quad (3.5)$$

and

$$h_u = x_i, X_{m+1} \leq i \leq 255 \quad (3.6)$$

where, M and N represent the number of pixels row-wise and column-wise respectively.

Step 4: Calculate the probability of occurrence of intensity value,  $i$  in the image

for both the sub-histograms,  $h_l$  and  $h_u$  separately.

$$p_x(i) = \frac{n_i}{n_l}, 0 \leq i \leq X_m \quad (3.7)$$

and

$$p_y(i) = \frac{n_i}{n_u}, X_{m+1} \leq i \leq 255 \quad (3.8)$$

where,  $n_l$  and  $n_u$  are the number of pixels contained in the first and second sub-image respectively.

Step 5: Calculate two cumulative distribution functions (CDFs) for the probabilities corresponding to the histograms  $h_l$  and  $h_u$  obtained in step 4.

$$cdf_x(i) = \sum_{j=0}^i p_x(j) \quad (3.9)$$

and

$$cdf_y(i) = \sum_{j=0}^i p_y(j) \quad (3.10)$$

Step 6: Apply histogram equalization technique on the two sub-histograms separately to obtain two sub-images,  $img\_x$  and  $img\_y$  which are then combined to obtain an overall image with improved contrast while preserving the mean brightness of the image. The effect of preservation leads to better preservation of the information content.

$$img\_x = round(minval\_x + (maxval\_x - minval\_x) \times cdf_x(img)) \quad (3.11)$$

and

$$img\_y = round(minval\_y + (maxval\_y - minval\_y) \times cdf_y(img)) \quad (3.12)$$

where  $minval\_x = 0$ ,  $maxval\_x = X_m$ ,  $minval\_y = X_{m+1}$ ,  $maxval\_x = 255$  and ‘img’ is the test image where  $X_m = 133$  and  $121$  for HE and BBHE respectively.

### 3.2.3 Bi-Histogram Equalization with a Plateau Limit (BHEPL)

Histogram Equalization (HE) suffers from the problem of over enhancement and also does not preserve the brightness of the image during the enhancement procedure. BBHE on the other hand is able to preserve the mean brightness of the image but it also

suffers from the problem of over enhancement. Bi-histogram equalization with a plateau limit (BHEPL) (Ooi, Pik Kong, & Ibrahim, 2009) not only addresses the problem of mean brightness but also resolve the problem of over enhancement in images. The other advantage associated with BHEPL is that it is computationally very fast in comparison to HE and BBHE approaches.

### **Basic steps for Retinal image enhancement using bi-histogram Equalization with Plateau Limit (BHEPL)**

Step 1: Read the input image and convert it into grayscale image.

Step 2: Calculate the histogram of the image.

Step 3: Find the mean,  $X_m$  of the image and split the histogram into two sub-histograms  $h_l$  and  $h_u$  at the obtained value of mean using Eq. 3.4.

Step 4: Find the plateau limit for each of the sub-histograms,  $h_l$  and  $h_u$  using the following equations:

$$T_l = \frac{1}{X_m + 1} \sum_{k=0}^{X_m} h_l(k) \quad (3.13)$$

and

$$T_u = \frac{1}{(L - 1) - X_m} \sum_{k=X_m+1}^{X_{L-1}} h_u(k) \quad (3.14)$$

It can be observed that both  $T_l$  and  $T_u$  are the averages, where  $T_l$  is the average of histogram  $h_l$  and  $T_u$  is the average of the histogram  $h_u$ .

Step 5: Using these plateau limits, clips both the sub-histograms as shown below:

$$h_{cl}(x) = \begin{cases} h_l(x) & \text{if } h_l(x) \leq T_l \\ T_l, & \text{elsewhere} \end{cases} \quad (3.15)$$

and

$$h_{ul}(x) = \begin{cases} h_u(x) & \text{if } h_u(x) \leq T_u \\ T_u, & \text{elsewhere} \end{cases} \quad (3.16)$$

Step 6: Calculate the probability of occurrence of intensity value,  $i$  in the image for both the clipped sub-histograms,  $h_l$  and  $h_u$  separately using the Eq. 3.7 and Eq. 3.8 respectively.

Step 7: Calculate two cumulative distribution functions (CDFs) for the probabilities corresponding to the clipped histograms  $h_l$  and  $h_u$  obtained in step 6 using Eq. 3.9 and Eq. 3.10.

Step 8: Apply histogram equalization technique on the two sub-histograms separately to obtain two sub-images,  $img_x$  and  $img_y$  which are then combined to obtain an overall image with improved contrast while preserving the mean brightness of the image using Eq. 3.11 and Eq. 3.12 respectively.

### **3.2.4 Dominant Orientation-based Texture Histogram Equalization (DOTHE)**

Histogram equalization based methods suffer from the problem of producing undesirable artefacts and this happens because the pixels belonging to non-texture regions dominate the pixels belonging to the texture regions. Dominant orientation-based texture histogram equalization (DOTHE) (K. Singh, Vishwakarma, Walia, & Kapoor, 2016) approach addresses this problem by constructing a histogram using only those patches of the image which have dominant orientation.

#### **Basic steps for Retinal image enhancement using dominant orientation-based texture histogram equalization**

Step 1: Read the input image and convert it into grayscale image.

Step 2: Extract overlapping patches of size  $5 \times 5$  from the image.

Step 3: Differentiate the patches into smooth and rough patches based on the variance threshold,  $\tau$  which is chosen to be 50. All the patches having  $variance \leq \tau$  are treated to be smooth patches and others as rough patches.

Step 4: Classify the patches into dominant and non-dominant patches based on the local orientation of the patches where local orientation is calculated based on singular value decomposition (SVD).

(a). Find the local gradients  $\nabla I(x, y)$  at each pixel location  $(x, y)$  in the patch. Padding is done with 0 values at the edges.

$$\nabla I(x, y) = \left\{ \frac{\partial I(x, y)}{\partial x}, \frac{\partial I(x, y)}{\partial y} \right\}$$

A gradient map  $G \in R^{N \times 2}$  is created from each patch where

$$G = \{\nabla I(x, y)_1, \nabla I(x, y)_2, \dots, \nabla I(x, y)_n\} \quad (3.17)$$

(b). Compute the SVD of gradient map

$$G = USV^T \quad (3.18)$$

Where  $U \in R^{N \times N}$  represents the contribution of each vector to singular vector;  $S \in R^{N \times 2}$  represents the strength of each vector; and  $V \in R^{2 \times 2}$  represents the orientation in which first vector and second vector represents the dominant orientation and sub-dominant orientation of the gradient fields.

(c). The diagonal values  $s_1$  and  $s_2$  of  $S$  are used to classify each patch into dominant or non-dominant patch by using the following equation;

$$R = \frac{s_1 - s_2}{s_1 + s_2} \quad (3.19)$$

The patches having  $R$  value less than the threshold  $R^* = 0.175$  are chosen to be dominant patches and all other patches as non-dominant patches.

Step 5: Create a histogram from intensity values belonging to the dominant patches using Eq. 3.1.

Step 6: Create a cumulative distribution function (CDF) using Eq. 3.2.

Step 7: Generate an equalized image,  $F$  by utilizing the CDF obtained in step 5

as shown below:

$$F = X_0 + (L - 1 - X_0) * CDF \quad (3.20)$$

where  $X_0$  represents the minimum intensity value and  $L$  is the total number of intensity levels.

### **3.2.5 Recursive sub-image histogram equalization (RSIHE)**

Recursive sub-image histogram equalization (RSIHE) (Sim et al., 2007) is a robust technique that preserve brightness in contrast to some other histogram equalization approaches. The other advantages associated with RSIHE are its ability to preserve image information (Entropy), better contrast, and high peak signal to noise ratio (PSNR) and Mean structural similarity index (MSSI). Generally the equalization techniques tend to change the structural information of the image which the RSIHE method is able to preserve. Strong dependencies are exhibited by the pixels especially when the pixels are spatially more proximate. An important information about the structure of various objects contained in a visual scene is carried by these dependencies.

#### **Basic steps for Retinal image enhancement using recursive sub-image histogram equalization**

Step 1: Read the input image and convert it into grayscale image.

Step 2: Calculate the histogram,  $h$  of the image.

Step 3: Calculate the probability of occurrence of intensity value,  $i$  in the image using the Eq. 3.1.

Step 4: Calculate the cumulative distribution functions (CDF),  $cdf_x$  and  $cdf_y$  for different probabilities obtained in step 3 using Eq. 3.2.

Step 5: An intensity value,  $I$  is found where cumulative probability is 0.5 in the CDF.

Step 6: Split the histogram,  $h$  into sub-histograms  $h_l$  and  $h_u$  based on the intensity value,  $I$  found in step 5. Both the histograms contain same number of pixels.

Step 7: Calculate the probability of occurrence of intensity value,  $i$  in the image for both the sub-histograms,  $h_l$  and  $h_u$  separately using Eq. 3.7 and Eq. 3.8 setting,  $X_m = I$ .

Step 8: Calculate two cumulative distribution functions (CDFs) for the probabilities corresponding to the histograms  $h_l$  and  $h_u$  obtained in step 7.

Step 9: Apply histogram equalization technique on the two sub-histograms separately to obtain two sub-images,  $F_l$  and  $F_u$  which are then combined to obtain an overall image with improved contrast.

$$F_l = X_0 + (X_m - X_0) \operatorname{cdf}_x \quad (3.21)$$

and

$$F_u = X_{m+1} + (X_{L-1} - X_{m+1}) \operatorname{cdf}_y \quad (3.22)$$

### **3.2.6 Quadrant Dynamic Histogram Equalization for Contrast Enhancement (QDHE)**

Quadrant dynamic histogram equalization (QDHE) (Ooi & Mat Isa, 2010) technique split the histogram into four sub-histograms based on the median value of the input image. Each of the sub-histogram is then clipped in order to address the problem of over-enhancement. Each clipped histogram is stretched to the available dynamic range to improve the overall contrast of the image. The advantage associated with this technique is that it is able to preserve the image details without over-enhancement and noise amplification.

#### **Basic steps for Retinal image enhancement using quadrant dynamic histogram equalization**

Step 1: Read the input image and convert it into grayscale image.

Step 2: Calculate the histogram,  $h$  of the image.

Step 3: Find the median intensity value of the histogram and partition the histogram,  $h$  into two histograms,  $h_l$  and  $h_u$  on the basis of the median intensity value. Both the sub-histograms have equal number of pixels.

Step 4: Find the median intensity value for each of the two sub-histograms  $h_l$  and  $h_u$  obtained in step 3. On the basis of the median intensity values, each sub-histogram is

further partitioned into two sub-histograms to obtain,  $h_{l1}$ ,  $h_{l2}$ ,  $h_{u1}$ and  $h_{u2}$ . Each sub-histogram has equal number of pixels.

Step 5: Perform histogram clipping to prevent over-enhancement using the Eq. 3.16.

Step 6: Even though all the sub-histograms have an equal number of pixels they may have different range of intensity values. Some ranges might be very small and it may not lead to good contrast in those sub-histograms. So four new ranges have been defined as follows:

$$span_i = m_{i+1} - m_i \quad (3.23)$$

and

$$range_i = (L - 1) \times span_i / \sum_{k=1}^4 span_k \quad (3.24)$$

where  $m_i$  is the  $i^{th}$ separating point in the histogram. Each  $range_i$  is represented by  $[i_{start}, i_{end}]$ .

Step 7: Calculate the probability of occurrence of intensity value,  $i$  in the image for all the four sub-histograms,  $h_{l1}$ ,  $h_{l2}$ ,  $h_{u1}$ and  $h_{u2}$  separately using Eq. 3.7 and Eq. 3.8 setting,  $X_m$  to the corresponding split value obtained in step 6.

Step 8: Calculate four cumulative distribution functions (CDFs) for the probabilities corresponding to the histograms,  $h_{l1}$ ,  $h_{l2}$ ,  $h_{u1}$ and  $h_{u2}$  obtained in step 7 where the cumulative distribution functions (CDFs) can be calculated using the Eq. 3.9 and 3.10.

Step 9: Perform equalization of each histogram with a new range as follows:

$$img = (i_{end} - i_{start}) \times cdf(X_k) + i_{start} \quad (3.25)$$

### 3.2.7 Recursively Separated and Weighted Histogram Equalization (RSWHE)

Recursively separated and weighted histogram equalization (RSWHE) (Kim & Chung, 2008) technique recursively partitions the histogram based on the mean or median into two or more histograms. Weighted normalized power law functions based modification

is done to the sub-histograms which are then equalized to obtain a high contrast image. The approaches discussed thus far have not used weighting process for contrast improvement and this method is a unique kind of method. The concept of weighing leads to a better control over each and every histogram. The technique is able to preserve the mean brightness of the image better than other methods while improving the contrast of the images.

### **Basic steps for Retinal image enhancement using recursively separated and weighted histogram equalization**

Step 1: Read the input image and convert it into grayscale image.

Step 2: Calculate the histogram,  $h$  of the image.

Step 3: Divide the histogram into  $2^r$  histograms depending on the recursion level,  $r$ . At  $r = 1$ , the histogram is separated into two sub-histograms, at  $r = 2$ , it leads to the creation of four histograms, and similarly at  $r = n$ , it creates  $2^n$  histograms. Segmentation of histogram is done in two ways; one using mean of the histogram and other using the median.

#### a. Segmentation using mean

In it, the histogram,  $h$  at recursion level,  $t$  is partitioned into two sub-histograms,  $h_l$  and  $h_u$  based on the mean of the histogram defined over intensity range  $[X_l, X_u]$  for the next recursion level  $t+1$  as follows:

$$X_m^t = \left( \sum_{k=l}^u k \cdot p(k) \middle/ \sum_{k=l}^u p(k) \right) \quad (3.26)$$

#### b. Segmentation using median

Consider a histogram,  $h$  at recursion level,  $t$  defined over intensity range  $[X_l, X_u]$ . Let the CDF of the histogram at the intensity level  $X_l$  is  $m_1$  and CDF at the intensity level  $X_u$  is  $m_2$ . Then the median  $X_D^t$  to partition the histogram  $h$  into two sub-histograms,  $h_l$  and  $h_u$  is calculated as follows:

$$X_D^t = \operatorname{argmin}_{l \leq k \leq u} \left| c(k) - \frac{m_1 + m_2}{2} \right| \quad (3.27)$$

Step 4: Perform the histogram weighing process as follows:

- a. Compute the maximum and minimum probability of each histogram as shown in Eq. 3.28 and Eq. 3.29.

$$p_{max} = \max_{0 \leq k \leq L-1} p(k) \quad (3.28)$$

and

$$p_{min} = \min_{0 \leq k \leq L-1} p(k) \quad (3.29)$$

- b. For every sub-histogram, compute the CDF as shown in the following equation:

$$CDF(x) = \sum_{k=l}^u p(k) \quad (3.30)$$

- c. For each sub-histogram modify the original probability values of  $p(k)$  into weighted  $p_w(k)$  by using,  $p_{max}$ ,  $p_{min}$ , and  $CDF(x)$  as shown below:

$$p_w(k) = p_{max} \cdot \left( \frac{p(k) - p_{min}}{p_{max} - p_{min}} \right) + \beta \quad (3.31)$$

where  $\beta$  is a constant used to control both the mean brightness and contrast of the image.

- d. Each weighted sub-histogram is then normalized using the Eq. 3.32 as shown below:

$$p_n = p_w(k) / \sum_{j=0}^{L-1} p_w(j) \quad (3.32)$$

Step 5: Equalize the normalized histogram to obtain a high contrast image.

### 3.3 Retinal Vessel Segmentation techniques

#### 3.3.1 2-D Matched Filter based vessel segmentation

Piecewise linear segments of the retinal blood vessels are detected by the matched filter proposed by (Chaudhuri et al., 1989). Twelve different templates of the matched filter have been used to detect the blood vessels in the image located at twelve different orientations. Two properties were taken into account while designing the filter; first is that the blood vessels have low intensity as we move from the edges towards the vessel center and it can be approximated by the Gaussian curve, and second is that the width of the vessels decreases as they move outward from the optic disk. In this work, the vessel width is taken to be a fixed value,  $2\sigma$ . The created filter is symmetrical in nature and has approximately the same shape as that of the intensity profile. The filter is applied to each and every pixel of the image.

#### Basic steps for retinal vessel segmentation using matched filter

Step 1: Choose the size of the filter, in this work it is chosen to be  $15 \times 15$  with the center of the filter at  $(0,0)$ .

Step 2: Choose the values of various parameters which are required to be used in the Gaussian distribution function as shown in the following equation:

$$K_i(x, y) = -e^{((u^2+v^2)/2\sigma^2)} \times 10 \quad (3.33)$$

where  $\sigma$  is the standard deviation and it is taken to be 2. The parameter  $i$  keeps the track of the sequence of the filter template. The values of  $u$  and  $v$  are decided on the basis of the following equation:

$$[u, v]x, y \begin{bmatrix} \cos\theta & \sin\theta \\ -\sin\theta & \cos\theta \end{bmatrix} \quad (3.34)$$

where both  $x, y$  varies between  $(-7, 7)$  considering  $(0, 0)$  the central pixel value for the filter. The filter must satisfy that  $|u| \leq 3\sigma$  and  $|v| \leq L/2$ . In this work  $L = 9$  where  $L$  represents the length of the piecewise linear segment of the vessel.

Step 3: Decide the number of orientations, in this work, 12 different orientations are decided each separated from other by an orientation of  $15^\circ$  based on which  $\theta$  is decided. The values obtained for  $\theta \in \{0^\circ, 15^\circ, 30^\circ, \dots, 165^\circ\}$ .

Step 4: Using the chosen parametric values, create 12 different filter templates. Subtract from each of the template values, the mean of the template to obtain a final set of filter templates.

Step 5: Read the input image and convert it into grayscale image.

Step 6: Smooth the image with  $5 \times 5$  mean filter to remove the effect of noise.

Step 7: Apply all the filter template on each and every pixel of the image. For every pixel, 12 different values will be obtained, choose the maximum value to obtain the vessel extracted image.

### **3.3.2 A hybrid filter of Matched and Difference of Gaussian filter based segmentation**

In this work, a combination of matched filter and difference of Gaussian filter is used to detect the blood vessels from the retina. Though matched filter alone can detect blood vessels, it suffers from the problem of misclassification of non-vascular structures as vessel pixels due to the fact that blood vessels have a Gaussian nature. Difference of Gaussian (DoG) filter is used to avoid such false detection. In the DoG filter, two versions of an image is created from the original image and later one more blurred version is subtracted from the less blurred version of the image. The effect of the combination can be observed from the images. Higher accuracy is achieved using the hybrid version of matched and DoG filter.

#### **Basic steps for retinal vessel segmentation using hybrid filter**

Step 1: Choose the size of the filter, in this work it is chosen to be  $15 \times 15$  with the center of the filter at  $(0,0)$ .

Step 2: Choose the values of various parameters which are required to be used in the Gaussian distribution function as shown in the equation 3.33.

Step 3: Decide the number of orientations, in this work, 12 different orientations are decided each separated from other by an orientation of  $15^\circ$  based on which  $\theta$  is decided. The values obtained for  $\theta \in \{0^\circ, 15^\circ, 30^\circ, \dots, 165^\circ\}$ .

Step 4: Using the chosen parametric values, create 12 different matched filter templates at  $\sigma = 2$ . Subtract from each of the template values, the mean of the template to obtain a final set of filter templates.

Step 5: Create 12 different matched filter templates separated at  $15^\circ$  for  $\sigma = 0.6$

Step 6: Subtract all the matched filters obtained at  $\sigma = 0.6$  from the corresponding matched filters obtained at  $\sigma = 2$  to obtain 12 different DoG filters.

Step 7: Read the input image and convert it into grayscale image.

Step 8: Smooth the image with  $3 \times 3$  mean filter to remove the effect of the noise.

Step 9: Apply all the 12 matched filters on the image and obtain 12 different values for each pixel. Choose the maximum value for each pixel to obtain the vessel detected image. Similarly create an image consisting of maximum values obtained from DoG filters. Now change the intensity value of all those pixels in the vessel detected image which have a value of 0 in the corresponding image obtained from DoG filters to obtain the final image.

### 3.3.3 Retinal Vessel Segmentation using Line Operator

In this approach, Line operators are used to differentiate between vessel and non-vessel pixels (Ricci & Perfetti, 2007). The proposed method has the same advantages as that of a matched filter but it avoids the drawbacks that occur in the case of the matched filter. Another benefit of using line operator is its low computational cost and better noise handling capability. Line operator is used in two ways, supervised and unsupervised learning, to classify pixels as vessel and non-vessel pixels. In both the cases, the line operator of length 15 is applied in 12 different directions and maximum modulus among these orientations is selected to decide.

### **Basic steps for retinal vessel segmentation using line operator**

Step 1: Choose the size of the filter, in this work it is chosen to be  $15 \times 15$  with the center of the filter at  $(0,0)$ .

Step 2: Find the average intensity value along the lines located at  $15^\circ$  from each other passing through the pixel under consideration as shown in the figure below.

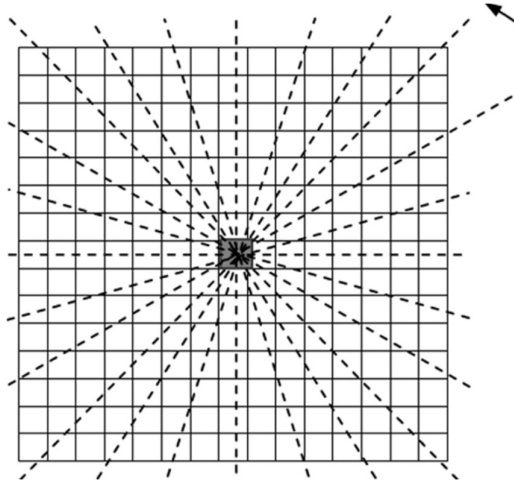


Fig. 3.1 Line operator

Step 3: Find the line having the maximum average intensity value,  $L(i,j)$ . From this value subtract the value,  $N(i,j)$  which is the intensity value obtained by averaging the intensity values of the  $15 \times 15$  window to obtain,  $S(i,j)$ .

Step 4: Use unsupervised learning to classify the pixel as a vessel pixel if the value,  $S(i,j) > T$ , where  $T$  is the threshold value otherwise the pixel is classified as a non-vessel pixel.

Step 5: In order to remove false positives occurring due to varying width and intensity of vessels, a new line 3 pixels wide and orthogonal to the main line lying at the center of the main line has also been considered. Strength,  $S_o(i,j)$  around this line is also calculated by subtracting the value,  $N(i,j)$  which is the intensity value obtained by averaging the intensity values of the  $15 \times 15$  window from  $L_o(i,j)$  where  $L_o(i,j)$  is the average intensity value of the new line.

Step 6: Form a feature vector consisting of 3 features,  $S_{\circ}(i,j)$ ,  $S(i,j)$  and  $I$  where  $S(i,j)$  is the line strength of the main line,  $S_{\circ}(i,j)$  is the line strength of the orthogonal line and  $I$  is the intensity value of the pixel under consideration.

Step 7: This feature vector  $X = [S_{\circ}(i,j), S(i,j), I]$  is provided to the support vector machine (SVM) classifier to classify pixel into vessel or non-vessel pixel.

### 3.3.4 Retinal Vessel Segmentation using Gabor wavelet and SVM

Multi-scale Gabor wavelet oriented at 18 different directions to detect blood vessels located at various angles is applied to the input image (Soares et al., 2006). The advantage of using the Gabor wavelet is its ability to be tuned to a particular frequency. Patches are extracted from the Gabor filtered real images and their corresponding original images to extract the Gabor values and intensity values respectively to create feature vectors. Feature vectors are created at two scales, in order to account for varying vessel diameter. Support vector machine (SVM) is used to classify the pixel into vessel/non-vessel pixel.

The technique although achieves high value for sensitivity suffers from high number of false positives, as a result of which the mean accuracy obtained for the technique is approximately 80% on the DRIVE dataset. Apart from high number of false positives, the techniques needs a very high training time of approximately 3 hours.

#### Basic steps for retinal vessel segmentation using Gabor wavelet

Step 1: Create a Gabor filter bank with each Gabor wavelet of the bank oriented at different angle,  $\theta$  where  $\theta = \{0^\circ, 10^\circ, \dots, 170^\circ\}$  as shown below:

$$G = \exp\left(-\frac{x'^2 + \gamma^2 y'^2}{2\sigma^2}\right) \exp\left(i(2\pi \frac{x' + y'}{\lambda} + \psi)\right) \quad (3.35)$$

where

$$x' = x\cos\theta + y\sin\theta \quad (3.36)$$

$$y' = -x\sin\theta + y\cos\theta \quad (3.37)$$

$\sigma$  is the standard deviation which represents the scale, here two scales are chosen,  $\sigma = 2$  and  $\sigma = 4$ .  $\gamma$  controls the filter elongation size. In this work,  $\gamma$  is chosen to be 3 and 2 for  $\sigma = 2$  and  $\sigma = 4$  respectively.  $\lambda$  which controls the width of the filter is chosen

to be 6 for  $\sigma = 2$  and 8 for  $\sigma = 4$ . Gabor filter (real valued) created for the parameters  $\sigma = 4, \lambda = 8, \gamma = 2$  is shown below:

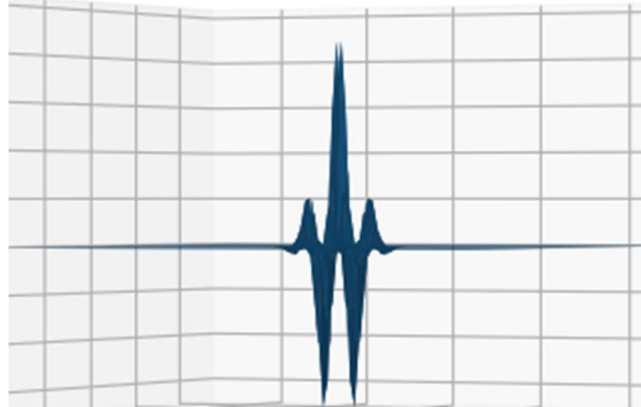


Fig. 3.2 Gabor filter

Step 2: The Gabor wavelet returns real, imaginary and modulus valued filters. Apply the real valued Gabor filter bank on each image to obtain 18 different convolved images for a single image.

Step 3: Create a maximum modulus image from the obtained eighteen different convolved images by choosing the maximum value for each pixel location from corresponding locations of all the 18 images. This is done for multiple scales  $\sigma = 2$  and  $\sigma = 4$ .

Step 4: Create patches of size  $7 \times 7$  around the pixel under consideration from the maximum modulus images and the corresponding original image to obtain three patches, where first two patches consist of the Gabor features obtained at different scales and the third patch consists of intensity values. The three patches are flattened and concatenated to create a feature vector. This process is repeated for all the images of the training dataset to create a set of feature vectors.

Step 5: Normalize the feature vectors to zero mean and unit variance and train the support vector machine (SVM) classifier with the created feature vectors along with the labels obtained from the ground truth images.

Step 6: Apply the trained SVM on the test dataset obtained the DRIVE dataset to classify pixels into vessel and non-vessel pixels.

### **3.4 Results and Discussion**

Majority of the techniques have been implemented in Matlab except one technique which has been implemented using Python and OpenCv library. To evaluate the performance of the techniques, the techniques have been applied to publicly available DRIVE and STARE datasets. The last technique under this section has only been applied to the DRIVE dataset as the technique fails to give encouraging results.

#### **3.4.1 Performance Analysis of Image Enhancement techniques**

Various image enhancement techniques discussed earlier in this chapter have been applied to all the images of the DRIVE, STARE, and CHASE\_DB datasets and the results have been computed in terms of Entropy, Peak signal to noise ratio (PSNR), Structured similarity index (SSIM), and Euclidean distance. Average results in terms of each metric have also been calculated to understand the overall performance of the technique on each dataset.

##### **3.4.1.1 Quantitative results**

The quantitative results for image enhancement techniques have been presented in Tables 3.1 to 3.21. The best technique should be able to achieve higher value of Entropy, SSIM, and PSNR besides lower value of Euclidean distance. Average results to analyze the performance of the techniques on various datasets have been presented in Fig. 3.3 – 3.6. Fig. 3.3 reveals that Bi-histogram equalization based on plateau limit (BHEPL) is able to achieve highest entropy on all the three datasets whereas Retinal image enhancement using recursively separated and weighted histogram equalization (RSWHE) is the worst performer in case of DRIVE and STARE datasets while Histogram Equalization (HE) performs poorly on CHASE dataset. RSWHE is able to achieve highest SSIM values in case of both DRIVE and STARE datasets whereas BHEPL performs better on the CHASE dataset as can be seen from Fig. 3.4. Again from Fig. 3.5 it can be inferred that RSWHE performs better in terms of PSNR on DRIVE and STARE datasets whereas it lags behind the BHEPL approach on the CHASE dataset. A low value of Euclidean distance is always desirable, and in this case QDHE performs better than the other techniques on DRIVE and CHASE datasets,

while it has comparable performance on the STARE dataset as can be observed in Fig. 3.6.

Table 3.1 Performance metrics obtained on DRIVE dataset using HE

<b>Image</b>	<b>Entropy</b>	<b>SSIM</b>	<b>PSNR</b>	<b>Euclidean</b>
Image 1	5.230	0.446	13.001	0.247
Image 2	5.205	0.497	15.494	0.245
Image 3	5.043	0.391	10.422	0.286
Image 4	5.301	0.578	13.785	0.242
Image 5	5.173	0.429	12.183	0.254
Image 6	5.071	0.410	12.479	0.259
Image 7	5.327	0.581	14.413	0.237
Image 8	5.262	0.478	13.204	0.248
Image 9	5.102	0.442	14.624	0.256
Image 10	5.271	0.476	11.358	0.250
Image 11	5.330	0.595	15.585	0.238
Image 12	5.219	0.450	13.564	0.250
Image 13	5.247	0.512	14.156	0.245
Image 14	5.256	0.487	13.948	0.254
Image 15	5.285	0.513	11.270	0.245
Image 16	5.234	0.486	14.646	0.247
Image 17	5.194	0.458	15.382	0.249
Image 18	5.326	0.521	15.180	0.239
Image 19	5.161	0.404	10.671	0.272
Image 20	5.199	0.449	12.498	0.252
<b>Average</b>	<b>5.222</b>	<b>0.480</b>	<b>13.393</b>	<b>0.251</b>

Table 3.2 Performance metrics obtained on STARE dataset using HE

<b>Image</b>	<b>Entropy</b>	<b>SSIM</b>	<b>PSNR</b>	<b>Euclidean</b>
Image 1	5.896	0.778	13.409	0.146
Image 2	5.938	0.810	13.169	0.135
Image 3	5.920	0.731	15.338	0.147
Image 4	5.916	0.809	14.234	0.142
Image 5	5.924	0.740	16.626	0.141
Image 6	5.974	0.873	22.056	0.126
Image 7	5.965	0.781	16.662	0.135
Image 8	5.921	0.779	13.818	0.139
Image 9	5.922	0.755	16.369	0.141
Image 10	5.794	0.669	11.926	0.158
Image 11	5.871	0.670	14.833	0.151
Image 12	5.880	0.697	16.469	0.148
Image 13	5.925	0.780	16.683	0.134
Image 14	5.953	0.783	16.336	0.134
Image 15	5.915	0.722	17.135	0.145
Image 16	5.939	0.764	12.066	0.141
Image 17	5.841	0.645	12.075	0.155
Image 18	5.933	0.842	15.086	0.135
Image 19	5.897	0.775	17.071	0.148
Image 20	5.933	0.777	17.058	0.148
<b>Average</b>	<b>5.913</b>	<b>0.759</b>	<b>15.421</b>	<b>0.142</b>

Table 3.3 Performance metrics obtained on CHASE dataset using HE

<b>Image</b>	<b>Entropy</b>	<b>SSIM</b>	<b>PSNR</b>	<b>Euclidean</b>
Image 1	4.703	0.481	9.483	0.423
Image 2	4.700	0.423	8.683	0.428
Image 3	4.714	0.528	10.340	0.423
Image 4	4.695	0.436	8.858	0.426
Image 5	4.707	0.485	9.677	0.421
Image 6	4.703	0.477	9.535	0.423
Image 7	4.707	0.497	9.569	0.424
Image 8	4.715	0.511	9.815	0.419
Image 9	4.716	0.548	11.281	0.421
Image 10	4.700	0.518	10.917	0.424
Image 11	4.693	0.425	8.607	0.427
Image 12	4.703	0.463	9.224	0.427
Image 13	4.704	0.490	10.297	0.422
Image 14	4.707	0.497	10.051	0.420
Image 15	4.456	0.425	8.543	0.485
Image 16	4.438	0.367	7.896	0.489
Image 17	4.719	0.578	12.186	0.423
Image 18	4.700	0.562	12.300	0.424
Image 19	4.638	0.426	9.487	0.422
Image 20	4.693	0.411	8.656	0.430
Image 21	4.765	0.555	13.101	0.413
Image 22	4.702	0.591	12.645	0.424
Image 23	4.720	0.494	9.644	0.423
Image 24	4.711	0.513	10.175	0.419
Image 25	4.729	0.412	8.580	0.426
Image 26	4.716	0.363	8.055	0.429
Image 27	4.699	0.566	11.490	0.422
Image 28	4.705	0.434	8.755	0.425
<b>Average</b>	<b>4.681</b>	<b>0.482</b>	<b>10.094</b>	<b>0.430</b>

Table 3.4 Performance metrics obtained on DRIVE dataset using BBHE

<b>Image</b>	<b>Entropy</b>	<b>SSIM</b>	<b>PSNR</b>	<b>Euclidean</b>
Image 1	5.503	0.442	12.496	0.256
Image 2	5.567	0.508	13.802	0.249
Image 3	5.199	0.381	10.725	0.285
Image 4	5.970	0.573	13.617	0.245
Image 5	5.374	0.420	11.936	0.265
Image 6	5.348	0.400	12.105	0.269
Image 7	5.991	0.575	14.327	0.240
Image 8	5.546	0.470	12.656	0.257
Image 9	5.369	0.449	13.287	0.261
Image 10	5.590	0.467	11.576	0.260
Image 11	5.944	0.594	14.300	0.238
Image 12	5.444	0.449	12.770	0.259
Image 13	5.674	0.508	13.290	0.253
Image 14	5.623	0.488	12.996	0.245
Image 15	5.884	0.524	12.382	0.252
Image 16	5.542	0.488	13.379	0.253
Image 17	5.449	0.472	13.689	0.253
Image 18	5.628	0.524	13.604	0.244
Image 19	5.379	0.392	11.021	0.271
Image 20	5.417	0.440	12.167	0.263
<b>Average</b>	<b>5.572</b>	<b>0.478</b>	<b>12.806</b>	<b>0.256</b>

Table 3.5 Performance metrics obtained on STARE dataset using BBHE

<b>Image</b>	<b>Entropy</b>	<b>SSIM</b>	<b>PSNR</b>	<b>Euclidean</b>
Image 1	6.589	0.795	13.602	0.122
Image 2	6.902	0.866	14.715	0.101
Image 3	6.431	0.730	14.017	0.132
Image 4	6.671	0.830	14.753	0.121
Image 5	6.700	0.736	14.995	0.117
Image 6	7.131	0.902	23.446	0.085
Image 7	6.818	0.777	15.947	0.108
Image 8	6.698	0.788	13.927	0.113
Image 9	6.665	0.753	15.229	0.115
Image 10	6.265	0.680	11.974	0.146
Image 11	6.391	0.661	13.461	0.136
Image 12	6.521	0.687	14.566	0.130
Image 13	6.869	0.785	16.592	0.105
Image 14	6.824	0.786	16.285	0.106
Image 15	6.526	0.722	15.389	0.125
Image 16	6.567	0.797	13.472	0.119
Image 17	6.297	0.647	11.900	0.143
Image 18	6.802	0.863	15.689	0.106
Image 19	6.453	0.755	15.062	0.126
Image 20	6.446	0.756	15.254	0.130
<b>Average</b>	<b>6.628</b>	<b>0.766</b>	<b>15.014</b>	<b>0.119</b>

Table 3.6 Performance metrics obtained on CHASE dataset using BBHE

<b>Image</b>	<b>Entropy</b>	<b>SSIM</b>	<b>PSNR</b>	<b>Euclidean</b>
Image 1	5.575	0.536	13.077	0.411
Image 2	5.467	0.492	12.292	0.413
Image 3	5.619	0.549	13.149	0.408
Image 4	5.479	0.497	12.238	0.413
Image 5	5.462	0.504	12.211	0.411
Image 6	5.514	0.509	12.373	0.411
Image 7	5.561	0.539	12.572	0.412
Image 8	5.529	0.534	12.304	0.409
Image 9	5.508	0.548	12.703	0.408
Image 10	5.439	0.514	12.512	0.409
Image 11	5.430	0.479	11.750	0.413
Image 12	5.623	0.537	13.045	0.412
Image 13	5.496	0.499	12.522	0.410
Image 14	5.472	0.504	12.073	0.409
Image 15	5.364	0.521	13.311	0.467
Image 16	5.134	0.434	11.658	0.470
Image 17	5.482	0.583	13.770	0.409
Image 18	5.454	0.566	13.807	0.411
Image 19	5.325	0.435	11.570	0.419
Image 20	5.393	0.455	11.726	0.417
Image 21	5.429	0.561	13.270	0.408
Image 22	5.553	0.596	13.339	0.407
Image 23	5.652	0.559	13.388	0.408
Image 24	5.534	0.522	12.368	0.409
Image 25	5.358	0.471	11.763	0.421
Image 26	5.204	0.419	11.081	0.424
Image 27	5.539	0.570	12.693	0.406
Image 28	5.561	0.530	12.781	0.411
<b>Average</b>	<b>5.447</b>	<b>0.515</b>	<b>12.557</b>	<b>0.417</b>

Table 3.7 Performance metrics obtained on DRIVE dataset BHEPL

<b>Image</b>	<b>Entropy</b>	<b>SSIM</b>	<b>PSNR</b>	<b>Euclidean</b>
Image 1	5.590	0.589	14.797	0.254
Image 2	5.668	0.631	15.293	0.251
Image 3	5.277	0.516	11.407	0.287
Image 4	6.092	0.761	17.014	0.240
Image 5	5.465	0.573	14.179	0.265
Image 6	5.468	0.602	15.145	0.269
Image 7	6.113	0.805	16.852	0.239
Image 8	5.667	0.636	14.832	0.257
Image 9	5.465	0.619	16.778	0.258
Image 10	5.675	0.621	14.340	0.257
Image 11	6.043	0.718	15.879	0.238
Image 12	5.546	0.589	15.212	0.256
Image 13	5.763	0.664	14.212	0.256
Image 14	5.710	0.635	15.127	0.249
Image 15	6.045	0.795	16.695	0.245
Image 16	5.632	0.621	15.521	0.253
Image 17	5.548	0.620	16.591	0.251
Image 18	5.708	0.638	16.288	0.242
Image 19	5.468	0.546	12.705	0.272
Image 20	5.490	0.574	13.928	0.263
<b>Average</b>	<b>5.672</b>	<b>0.638</b>	<b>15.140</b>	<b>0.255</b>

Table 3.8 Performance metrics obtained on STARE dataset BHEPL

<b>Image</b>	<b>Entropy</b>	<b>SSIM</b>	<b>PSNR</b>	<b>Euclidean</b>
Image 1	6.679	0.889	16.524	0.105
Image 2	6.984	0.932	17.535	0.086
Image 3	6.512	0.831	15.456	0.133
Image 4	6.788	0.927	15.451	0.117
Image 5	6.771	0.868	18.338	0.106
Image 6	7.256	0.957	27.082	0.077
Image 7	6.874	0.879	16.651	0.106
Image 8	6.764	0.864	15.512	0.102
Image 9	6.725	0.841	15.715	0.113
Image 10	6.349	0.781	13.590	0.143
Image 11	6.461	0.787	16.071	0.129
Image 12	6.626	0.838	18.684	0.113
Image 13	6.927	0.876	18.634	0.095
Image 14	6.877	0.860	17.935	0.099
Image 15	6.573	0.823	15.651	0.130
Image 16	6.620	0.825	13.178	0.120
Image 17	6.378	0.773	14.687	0.137
Image 18	6.873	0.915	16.455	0.097
Image 19	6.503	0.825	15.439	0.129
Image 20	6.495	0.836	17.238	0.126
<b>Average</b>	<b>6.702</b>	<b>0.856</b>	<b>16.791</b>	<b>0.113</b>

Table 3.9 Performance metrics obtained on CHASE dataset using BHEPL

<b>Image</b>	<b>Entropy</b>	<b>SSIM</b>	<b>PSNR</b>	<b>Euclidean</b>
Image 1	5.702	0.840	17.521	0.403
Image 2	5.661	0.826	16.642	0.406
Image 3	5.762	0.844	16.818	0.402
Image 4	5.697	0.828	15.936	0.406
Image 5	5.577	0.736	16.083	0.406
Image 6	5.714	0.838	16.265	0.403
Image 7	5.730	0.849	16.272	0.405
Image 8	5.604	0.754	15.856	0.405
Image 9	5.647	0.771	15.681	0.405
Image 10	5.576	0.743	14.828	0.406
Image 11	5.553	0.807	15.891	0.406
Image 12	5.855	0.880	17.693	0.404
Image 13	5.645	0.781	17.024	0.407
Image 14	5.582	0.760	16.414	0.404
Image 15	5.595	0.870	17.105	0.463
Image 16	5.338	0.822	16.213	0.465
Image 17	5.702	0.820	17.032	0.406
Image 18	5.677	0.824	17.689	0.408
Image 19	5.508	0.765	17.594	0.413
Image 20	5.547	0.818	16.801	0.408
Image 21	5.590	0.811	17.694	0.405
Image 22	5.676	0.816	17.540	0.403
Image 23	5.882	0.866	16.288	0.401
Image 24	5.656	0.757	16.300	0.405
Image 25	5.480	0.824	16.908	0.412
Image 26	5.334	0.801	16.407	0.414
Image 27	5.653	0.777	16.250	0.402
Image 28	5.797	0.868	16.504	0.403
<b>Average</b>	<b>5.615</b>	<b>0.809</b>	<b>16.693</b>	<b>0.412</b>

Table 3.10 Performance metrics obtained on DRIVE dataset using DOTHE

<b>Image</b>	<b>Entropy</b>	<b>SSIM</b>	<b>PSNR</b>	<b>Euclidean</b>
Image 1	5.264	0.448	14.586	0.282
Image 2	5.351	0.512	14.859	0.292
Image 3	4.976	0.443	12.581	0.328
Image 4	5.781	0.593	16.152	0.269
Image 5	5.139	0.466	14.105	0.306
Image 6	5.179	0.482	14.132	0.292
Image 7	5.789	0.601	15.846	0.283
Image 8	5.342	0.507	15.123	0.299
Image 9	5.164	0.489	14.451	0.289
Image 10	5.353	0.531	14.174	0.302
Image 11	5.707	0.605	15.793	0.282
Image 12	5.201	0.469	14.504	0.301
Image 13	5.439	0.518	15.295	0.296
Image 14	5.378	0.464	14.434	0.279
Image 15	5.706	0.597	14.641	0.293
Image 16	5.298	0.483	14.536	0.295
Image 17	5.147	0.466	14.242	0.305
Image 18	5.283	0.515	14.536	0.306
Image 19	5.160	0.461	12.972	0.309
Image 20	5.306	0.504	14.379	0.273
<b>Average</b>	<b>5.348</b>	<b>0.508</b>	<b>14.567</b>	<b>0.294</b>

Table 3.11 Performance metrics obtained on STARE dataset using DOTHE

<b>Image</b>	<b>Entropy</b>	<b>SSIM</b>	<b>PSNR</b>	<b>Euclidean</b>
Image 1	6.576	0.788	17.276	0.124
Image 2	6.772	0.787	18.162	0.108
Image 3	6.215	0.528	14.846	0.142
Image 4	6.690	0.797	12.982	0.127
Image 5	6.303	0.602	16.676	0.158
Image 6	6.974	0.737	16.282	0.102
Image 7	6.355	0.576	16.028	0.155
Image 8	6.514	0.637	15.105	0.123
Image 9	6.273	0.604	15.848	0.157
Image 10	6.232	0.679	12.925	0.144
Image 11	5.986	0.536	15.678	0.173
Image 12	5.942	0.576	16.782	0.213
Image 13	6.310	0.613	16.550	0.188
Image 14	6.282	0.592	16.101	0.178
Image 15	6.022	0.484	14.512	0.178
Image 16	6.556	0.781	13.005	0.122
Image 17	6.075	0.521	14.179	0.157
Image 18	6.713	0.820	17.357	0.109
Image 19	6.268	0.759	16.298	0.143
Image 20	6.239	0.754	16.219	0.143
<b>Average</b>	<b>6.365</b>	<b>0.659</b>	<b>15.640</b>	<b>0.147</b>

Table 3.12 Performance metrics obtained on CHASE dataset using DOTHE

<b>Image</b>	<b>Entropy</b>	<b>SSIM</b>	<b>PSNR</b>	<b>Euclidean</b>
Image 1	5.564	0.792	15.300	0.079
Image 2	5.448	0.742	14.494	0.080
Image 3	5.616	0.772	15.406	0.077
Image 4	5.437	0.726	14.338	0.081
Image 5	5.428	0.748	14.471	0.089
Image 6	5.468	0.734	14.884	0.083
Image 7	5.526	0.779	15.181	0.078
Image 8	5.489	0.774	14.384	0.085
Image 9	5.491	0.736	14.835	0.089
Image 10	5.380	0.702	14.279	0.098
Image 11	5.409	0.746	13.906	0.087
Image 12	5.544	0.760	15.682	0.074
Image 13	5.464	0.722	14.840	0.095
Image 14	5.443	0.742	14.587	0.092
Image 15	5.400	0.812	15.722	0.063
Image 16	5.168	0.753	13.807	0.085
Image 17	5.604	0.831	18.231	0.087
Image 18	5.544	0.833	18.854	0.089
Image 19	5.345	0.711	14.814	0.102
Image 20	5.374	0.734	14.184	0.091
Image 21	5.496	0.742	16.286	0.099
Image 22	5.573	0.857	18.670	0.080
Image 23	5.561	0.763	15.301	0.073
Image 24	5.513	0.741	14.769	0.084
Image 25	5.371	0.782	15.304	0.090
Image 26	5.227	0.759	14.487	0.099
Image 27	5.534	0.787	15.026	0.088
Image 28	5.447	0.742	15.118	0.077
<b>Average</b>	<b>5.444</b>	<b>0.763</b>	<b>15.435</b>	<b>0.087</b>

Table 3.13 Performance metrics obtained on DRIVE dataset using RSIHE

<b>Image</b>	<b>Entropy</b>	<b>SSIM</b>	<b>PSNR</b>	<b>Euclidean</b>
Image 1	5.489	0.435	13.695	0.256
Image 2	5.581	0.493	14.745	0.251
Image 3	5.185	0.398	11.895	0.285
Image 4	5.966	0.574	14.742	0.245
Image 5	5.364	0.418	13.050	0.266
Image 6	5.362	0.397	13.286	0.270
Image 7	5.983	0.569	14.830	0.240
Image 8	5.549	0.464	13.837	0.257
Image 9	5.368	0.435	14.103	0.263
Image 10	5.602	0.485	12.986	0.259
Image 11	5.941	0.587	15.608	0.239
Image 12	5.447	0.440	13.777	0.259
Image 13	5.663	0.497	14.186	0.254
Image 14	5.613	0.477	13.997	0.243
Image 15	5.901	0.553	13.746	0.248
Image 16	5.545	0.475	14.270	0.254
Image 17	5.449	0.455	14.489	0.255
Image 18	5.626	0.509	14.702	0.247
Image 19	5.366	0.408	12.328	0.270
Image 20	5.390	0.437	13.296	0.264
<b>Average</b>	<b>5.570</b>	<b>0.475</b>	<b>13.878</b>	<b>0.256</b>

Table 3.14 Performance metrics obtained on STARE dataset using RSIHE

<b>Image</b>	<b>Entropy</b>	<b>SSIM</b>	<b>PSNR</b>	<b>Euclidean</b>
Image 1	6.581	0.813	14.809	0.119
Image 2	6.904	0.869	15.240	0.100
Image 3	6.422	0.743	15.553	0.133
Image 4	6.656	0.827	15.078	0.122
Image 5	6.700	0.751	16.610	0.119
Image 6	7.134	0.901	23.422	0.085
Image 7	6.811	0.783	16.811	0.109
Image 8	6.695	0.799	15.004	0.111
Image 9	6.660	0.766	16.542	0.115
Image 10	6.248	0.685	13.067	0.146
Image 11	6.387	0.681	15.271	0.136
Image 12	6.521	0.700	16.437	0.132
Image 13	6.874	0.801	17.835	0.104
Image 14	6.828	0.799	17.301	0.105
Image 15	6.507	0.728	16.757	0.129
Image 16	6.558	0.794	13.798	0.119
Image 17	6.286	0.679	13.456	0.140
Image 18	6.814	0.867	16.263	0.105
Image 19	6.447	0.779	16.697	0.130
Image 20	6.436	0.777	16.827	0.133
<b>Average</b>	<b>6.623</b>	<b>0.777</b>	<b>16.139</b>	<b>0.120</b>

Table 3.15 Performance metrics obtained on CHASE dataset using RSIHE

<b>Image</b>	<b>Entropy</b>	<b>SSIM</b>	<b>PSNR</b>	<b>Euclidean</b>
Image 1	5.582	0.542	13.423	0.411
Image 2	5.472	0.498	12.601	0.412
Image 3	5.632	0.549	13.612	0.408
Image 4	5.485	0.501	12.573	0.412
Image 5	5.477	0.515	12.982	0.410
Image 6	5.512	0.514	12.967	0.411
Image 7	5.568	0.545	13.094	0.412
Image 8	5.523	0.543	13.064	0.409
Image 9	5.511	0.543	13.371	0.407
Image 10	5.437	0.508	13.079	0.408
Image 11	5.418	0.490	12.300	0.413
Image 12	5.634	0.540	13.326	0.412
Image 13	5.494	0.497	13.045	0.409
Image 14	5.476	0.514	13.116	0.408
Image 15	5.378	0.522	13.316	0.467
Image 16	5.119	0.438	11.870	0.469
Image 17	5.482	0.582	13.444	0.409
Image 18	5.455	0.565	13.405	0.411
Image 19	5.340	0.453	12.808	0.418
Image 20	5.385	0.472	12.375	0.417
Image 21	5.431	0.556	13.613	0.408
Image 22	5.533	0.592	13.805	0.407
Image 23	5.639	0.560	13.633	0.408
Image 24	5.538	0.529	13.273	0.409
Image 25	5.372	0.484	12.306	0.420
Image 26	5.214	0.445	11.819	0.422
Image 27	5.547	0.570	13.725	0.406
Image 28	5.569	0.531	12.869	0.411
<b>Average</b>	<b>5.449</b>	<b>0.520</b>	<b>13.025</b>	<b>0.417</b>

Table 3.16 Performance metrics obtained on DRIVE dataset using QDHE

<b>Image</b>	<b>Entropy</b>	<b>SSIM</b>	<b>PSNR</b>	<b>Euclidean</b>
Image 1	5.458	0.555	14.376	0.198
Image 2	5.556	0.589	15.704	0.146
Image 3	5.163	0.569	12.056	0.268
Image 4	5.980	0.735	15.876	0.111
Image 5	5.324	0.526	13.639	0.219
Image 6	5.318	0.510	13.813	0.227
Image 7	5.987	0.692	16.029	0.180
Image 8	5.531	0.606	14.680	0.140
Image 9	5.359	0.539	15.099	0.161
Image 10	5.539	0.589	13.319	0.214
Image 11	5.940	0.692	16.951	0.119
Image 12	5.398	0.546	14.528	0.206
Image 13	5.638	0.513	15.264	0.190
Image 14	5.611	0.606	14.864	0.161
Image 15	5.906	0.658	13.806	0.209
Image 16	5.502	0.570	14.878	0.194
Image 17	5.447	0.530	15.442	0.158
Image 18	5.612	0.615	15.658	0.138
Image 19	5.334	0.516	12.434	0.246
Image 20	5.376	0.589	13.931	0.148
<b>Average</b>	<b>5.549</b>	<b>0.587</b>	<b>14.617</b>	<b>0.182</b>

Table 3.17 Performance metrics obtained on STARE dataset using QDHE

<b>Image</b>	<b>Entropy</b>	<b>SSIM</b>	<b>PSNR</b>	<b>Euclidean</b>
Image 1	6.584	0.792	13.441	0.121
Image 2	6.925	0.822	13.271	0.104
Image 3	6.425	0.744	15.343	0.133
Image 4	6.700	0.814	14.216	0.121
Image 5	6.697	0.749	16.635	0.119
Image 6	7.140	0.906	22.897	0.085
Image 7	6.814	0.783	16.587	0.109
Image 8	6.716	0.786	13.842	0.113
Image 9	6.661	0.765	16.321	0.115
Image 10	6.276	0.673	11.892	0.147
Image 11	6.381	0.673	14.800	0.137
Image 12	6.525	0.700	16.509	0.131
Image 13	6.872	0.790	16.807	0.105
Image 14	6.825	0.789	16.402	0.106
Image 15	6.505	0.724	17.049	0.129
Image 16	6.598	0.775	12.243	0.121
Image 17	6.304	0.650	12.087	0.143
Image 18	6.823	0.851	15.194	0.107
Image 19	6.447	0.781	17.024	0.130
Image 20	6.439	0.782	17.110	0.132
<b>Average</b>	<b>6.633</b>	<b>0.767</b>	<b>15.484</b>	<b>0.120</b>

Table 3.18 Performance metrics obtained on CHASE dataset using QDHE

<b>Image</b>	<b>Entropy</b>	<b>SSIM</b>	<b>PSNR</b>	<b>Euclidean</b>
Image 1	5.636	0.798	12.808	0.081
Image 2	5.619	0.778	11.816	0.083
Image 3	5.732	0.833	13.619	0.076
Image 4	5.664	0.798	12.127	0.080
Image 5	5.531	0.769	12.620	0.089
Image 6	5.676	0.807	12.668	0.081
Image 7	5.698	0.831	12.734	0.078
Image 8	5.586	0.803	12.729	0.086
Image 9	5.603	0.800	14.498	0.087
Image 10	5.531	0.788	13.762	0.094
Image 11	5.508	0.756	12.352	0.089
Image 12	5.818	0.841	13.029	0.071
Image 13	5.620	0.787	13.241	0.093
Image 14	5.547	0.777	12.746	0.093
Image 15	5.555	0.861	13.657	0.064
Image 16	5.286	0.765	12.589	0.085
Image 17	5.631	0.875	15.981	0.090
Image 18	5.592	0.855	16.187	0.095
Image 19	5.419	0.719	12.092	0.106
Image 20	5.492	0.734	11.539	0.094
Image 21	5.525	0.843	16.018	0.097
Image 22	5.643	0.877	15.747	0.086
Image 23	5.868	0.868	13.524	0.067
Image 24	5.623	0.804	13.028	0.083
Image 25	5.406	0.742	12.087	0.097
Image 26	5.264	0.691	11.166	0.109
Image 27	5.610	0.827	14.434	0.084
Image 28	5.777	0.837	12.542	0.072
<b>Average</b>	<b>5.588</b>	<b>0.802</b>	<b>13.262</b>	<b>0.086</b>

Table 3.19 Performance metrics obtained on DRIVE dataset using RSWHE

<b>Image</b>	<b>Entropy</b>	<b>SSIM</b>	<b>PSNR</b>	<b>Euclidean</b>
Image 1	4.354	0.864	25.282	0.269
Image 2	4.636	0.853	24.711	0.212
Image 3	4.134	0.877	28.906	0.250
Image 4	4.843	0.837	23.806	0.232
Image 5	4.226	0.859	25.943	0.284
Image 6	4.243	0.835	24.823	0.300
Image 7	4.959	0.798	23.037	0.216
Image 8	4.444	0.843	24.656	0.260
Image 9	4.382	0.821	23.464	0.251
Image 10	4.367	0.888	27.615	0.282
Image 11	4.928	0.863	24.508	0.232
Image 12	4.361	0.852	24.747	0.267
Image 13	4.715	0.846	25.492	0.217
Image 14	4.556	0.840	25.210	0.234
Image 15	4.710	0.827	25.441	0.252
Image 16	4.476	0.836	24.306	0.238
Image 17	4.475	0.810	23.106	0.237
Image 18	4.552	0.852	23.900	0.242
Image 19	4.241	0.859	27.823	0.294
Image 20	4.327	0.860	25.695	0.270
<b>Average</b>	<b>4.497</b>	<b>0.846</b>	<b>25.124</b>	<b>0.252</b>

Table 3.20 Performance metrics obtained on STARE dataset using RSWHE

<b>Image</b>	<b>Entropy</b>	<b>SSIM</b>	<b>PSNR</b>	<b>Euclidean</b>
Image 1	5.277	0.865	24.767	0.199
Image 2	5.528	0.872	24.255	0.166
Image 3	5.129	0.861	25.484	0.184
Image 4	5.530	0.904	24.804	0.148
Image 5	5.286	0.857	23.598	0.198
Image 6	5.866	0.833	20.353	0.151
Image 7	5.627	0.842	23.144	0.140
Image 8	5.425	0.863	25.022	0.171
Image 9	5.487	0.853	23.712	0.150
Image 10	4.939	0.852	26.409	0.232
Image 11	4.985	0.883	25.825	0.227
Image 12	5.146	0.881	23.923	0.219
Image 13	5.708	0.810	21.923	0.143
Image 14	5.650	0.812	21.989	0.149
Image 15	5.360	0.862	24.335	0.156
Image 16	5.276	0.881	26.439	0.168
Image 17	4.872	0.857	26.520	0.251
Image 18	5.528	0.871	23.528	0.156
Image 19	5.233	0.915	25.726	0.170
Image 20	5.231	0.921	25.803	0.172
<b>Average</b>	<b>5.354</b>	<b>0.865</b>	<b>24.378</b>	<b>0.177</b>

Table 3.21 Performance metrics obtained on CHASE dataset using RSWHE

<b>Image</b>	<b>Entropy</b>	<b>SSIM</b>	<b>PSNR</b>	<b>Euclidean</b>
Image 1	5.636	0.798	12.808	0.081
Image 2	5.619	0.778	11.816	0.083
Image 3	5.732	0.833	13.619	0.076
Image 4	5.664	0.798	12.127	0.080
Image 5	5.531	0.769	12.620	0.089
Image 6	5.676	0.807	12.668	0.081
Image 7	5.698	0.831	12.734	0.078
Image 8	5.586	0.803	12.729	0.086
Image 9	5.603	0.800	14.498	0.087
Image 10	5.531	0.788	13.762	0.094
Image 11	5.508	0.756	12.352	0.089
Image 12	5.818	0.841	13.029	0.071
Image 13	5.620	0.787	13.241	0.093
Image 14	5.547	0.777	12.746	0.093
Image 15	5.555	0.861	13.657	0.064
Image 16	5.286	0.765	12.589	0.085
Image 17	5.631	0.875	15.981	0.090
Image 18	5.592	0.855	16.187	0.095
Image 19	5.419	0.719	12.092	0.106
Image 20	5.492	0.734	11.539	0.094
Image 21	5.525	0.843	16.018	0.097
Image 22	5.643	0.877	15.747	0.086
Image 23	5.868	0.868	13.524	0.067
Image 24	5.623	0.804	13.028	0.083
Image 25	5.406	0.742	12.087	0.097
Image 26	5.264	0.691	11.166	0.109
Image 27	5.610	0.827	14.434	0.084
Image 28	5.777	0.837	12.542	0.072
<b>Average</b>	<b>5.566</b>	<b>0.802</b>	<b>13.511</b>	<b>0.088</b>

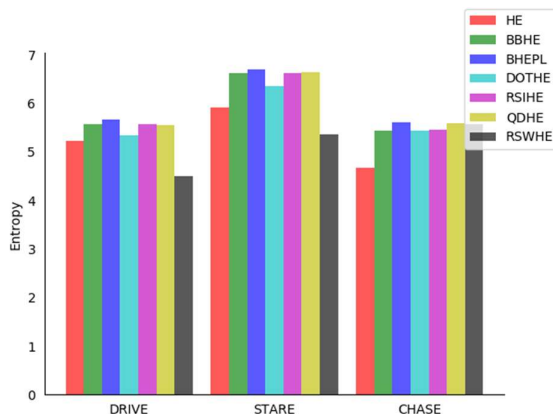


Fig. 3.3 Average Entropy results obtained using various image enhancement techniques on DRIVE, STARE, and CHASE datasets

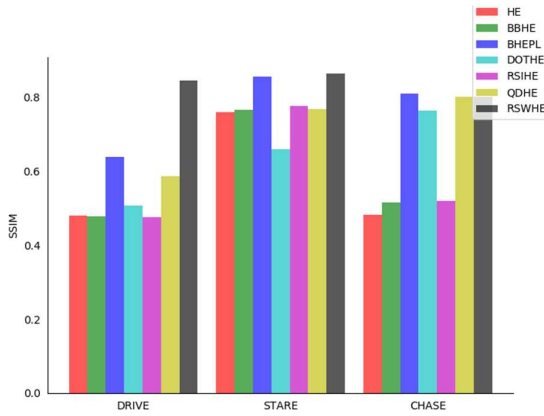


Fig. 3.4 Average SSIM results obtained using various image enhancement techniques on DRIVE, STARE, and CHASE datasets

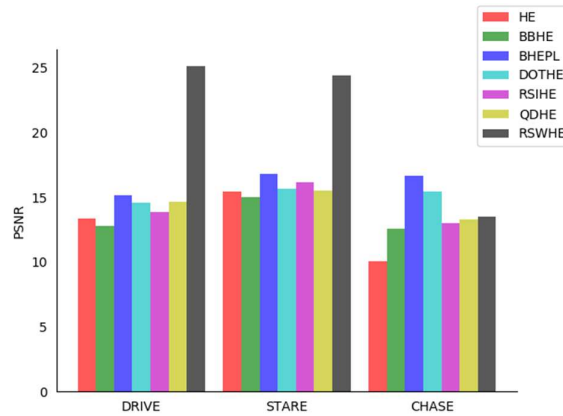


Fig. 3.5 Average PSNR results obtained using various image enhancement techniques on DRIVE, STARE, and CHASE datasets

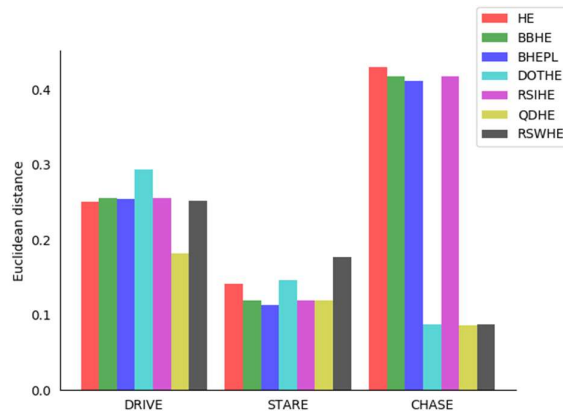


Fig. 3.6 Average Euclidean distance results obtained using various image enhancement techniques on DRIVE, STARE, and CHASE datasets

### 3.4.1.2 Qualitative results

The capability of the techniques can be observed on DRIVE, STARE, and CHASE datasets in the Fig. 3.7 to 3.9 respectively. As can be seen from figures, the enhanced images have higher quality than the original images in respective figures. Among these images, the images enhanced by BHEPL approach in all the three datasets have more uniform illumination than the other images in all the datasets. Also the mean intensity of the images enhanced by BHEPL approach is comparatively closer to the original image and thus has higher entropy than the other images. The images enhanced by RSWHE have higher SSIM and PSNR values but they suffer from over-enhancement at the center of the images and under-enhancement as we move towards the image boundary and this can be observed from the dark shades at the edges of the retina. Therefore overall, BHEPL exhibits better performance over other techniques.

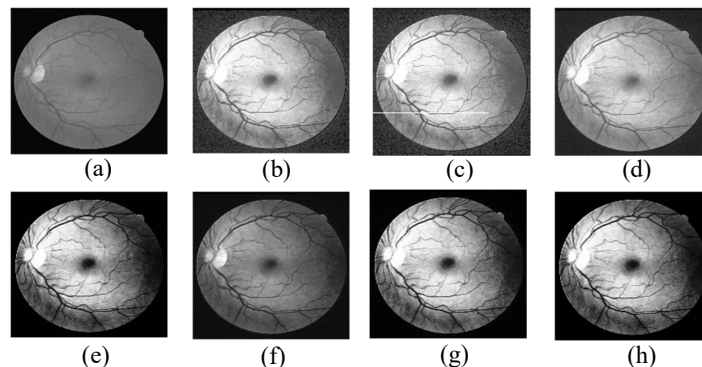


Fig. 3.7 Enhanced images obtained after applying various techniques on the image obtained from DRIVE dataset. (a) Original image (DRIVE) (b) HE (c) BBHE (d) BHEPL (e) DOTHE (f) RSIHE (g) QDHE (h) RSWHE

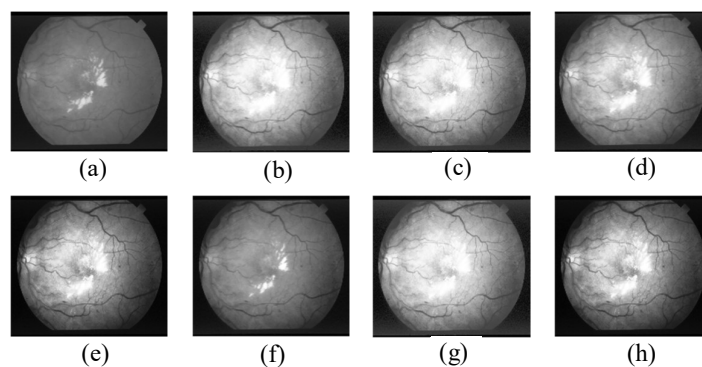


Fig. 3.8 Enhanced images obtained after applying various techniques on the image obtained from STARE dataset. (a) Original image (STARE) (b) HE (c) BBHE (d) BHEPL (e) DOTHE (f) RSIHE (g) QDHE (h) RSWHE

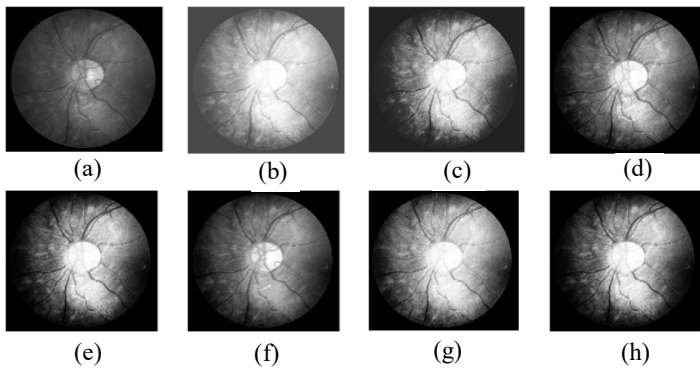


Fig. 3.9 Enhanced images obtained after applying various techniques on the image obtained from CHASE dataset. (a) Original image (CHASE) (b) HE (c) BBHE (d) BHEPL (e) DOTHE (f) RSIHE (g) QDHE (h) RSWHE

### 3.4.2 Performance Analysis of Vessel Segmentation techniques

Various vessel segmentation techniques discussed earlier in this chapter have been applied to all the images of the DRIVE and STARE datasets and the results have been computed in terms of Sensitivity, Specificity, and Accuracy. Average results in terms of each metric have also been calculated to understand the overall performance of the technique on each dataset.

#### 3.4.2.1 Quantitative results

The quantitative results for vessel segmentation techniques have been presented in Tables 3.22 to 3.29. The best technique should have higher sensitivity, specificity, and accuracy. The average results to analyze performance in terms of sensitivity, specificity, and accuracy have been presented in Fig. 3.10 – 3.12. From Fig. 3.10, we can observe that Gabor wavelet technique is better at detecting vessel pixels as it gives the highest sensitivity of 0.978 and 0.947 for DRIVE and STARE datasets respectively. The drawback of Gabor wavelet technique is that it is very poor at detecting non-vessel pixels as it exhibits a specificity of 0.420 and 0.491 for DRIVE and STARE respectively and same can be observed from Fig. 3.11. The technique using line operator performs better in identifying the non-vessel pixels and achieves specificity of 0.980 and 0.965 for DRIVE and STARE datasets respectively as shown in Fig. 3.11. Further, it can be perceived from Fig. 3.12 that line operator is not only better at detecting non-vessel pixels but also attains the best overall accuracy of 0.959 and 0.954 for DRIVE and STARE respectively.

Table 3.22 Performance metrics obtained on DRIVE dataset using Matched Filter approach

<b>Image</b>	<b>Sensitivity</b>	<b>Specificity</b>	<b>Accuracy</b>
Image 1	0.926	0.836	0.847
Image 2	0.896	0.850	0.857
Image 3	0.853	0.850	0.850
Image 4	0.869	0.828	0.833
Image 5	0.887	0.870	0.872
Image 6	0.864	0.858	0.859
Image 7	0.874	0.822	0.829
Image 8	0.872	0.832	0.837
Image 9	0.889	0.851	0.855
Image 10	0.891	0.858	0.862
Image 11	0.879	0.826	0.833
Image 12	0.896	0.828	0.836
Image 13	0.871	0.837	0.841
Image 14	0.913	0.815	0.827
Image 15	0.920	0.808	0.820
Image 16	0.921	0.841	0.851
Image 17	0.913	0.817	0.829
Image 18	0.926	0.830	0.841
Image 19	0.947	0.850	0.862
Image 20	0.929	0.855	0.863
<b>Average</b>	<b>0.897</b>	<b>0.838</b>	<b>0.845</b>

Table 3.23 Performance metrics obtained on STARE dataset using Matched Filter approach

<b>Image</b>	<b>Sensitivity</b>	<b>Specificity</b>	<b>Accuracy</b>
Image 1	0.897	0.785	0.797
Image 2	0.931	0.799	0.810
Image 3	0.941	0.706	0.725
Image 4	0.851	0.888	0.885
Image 5	0.904	0.752	0.771
Image 6	0.946	0.741	0.761
Image 7	0.934	0.787	0.804
Image 8	0.944	0.792	0.808
Image 9	0.923	0.814	0.826
Image 10	0.936	0.778	0.795
Image 11	0.950	0.816	0.830
Image 12	0.939	0.823	0.837
Image 13	0.909	0.818	0.830
Image 14	0.915	0.821	0.833
Image 15	0.910	0.798	0.812
Image 16	0.896	0.855	0.860
Image 17	0.937	0.815	0.830
Image 18	0.923	0.831	0.837
Image 19	0.869	0.859	0.860
Image 20	0.894	0.858	0.861
<b>Average</b>	<b>0.917</b>	<b>0.807</b>	<b>0.819</b>

Table 3.24 Performance metrics obtained on DRIVE dataset using Hybrid Filter approach

<b>Image</b>	<b>Sensitivity</b>	<b>Specificity</b>	<b>Accuracy</b>
Image 1	0.882	0.889	0.888
Image 2	0.836	0.900	0.892
Image 3	0.797	0.899	0.888
Image 4	0.822	0.883	0.877
Image 5	0.811	0.915	0.904
Image 6	0.784	0.908	0.895
Image 7	0.814	0.878	0.871
Image 8	0.788	0.889	0.879
Image 9	0.789	0.907	0.897
Image 10	0.833	0.906	0.899
Image 11	0.801	0.886	0.877
Image 12	0.830	0.888	0.882
Image 13	0.803	0.893	0.883
Image 14	0.861	0.876	0.875
Image 15	0.895	0.861	0.864
Image 16	0.839	0.896	0.890
Image 17	0.811	0.883	0.876
Image 18	0.854	0.893	0.889
Image 19	0.909	0.898	0.899
Image 20	0.875	0.905	0.903
<b>Average</b>	<b>0.832</b>	<b>0.893</b>	<b>0.886</b>

Table 3.25 Performance metrics obtained on STARE dataset using Hybrid Filter approach

<b>Image</b>	<b>Sensitivity</b>	<b>Specificity</b>	<b>Accuracy</b>
Image 1	0.836	0.849	0.848
Image 2	0.840	0.865	0.863
Image 3	0.905	0.784	0.792
Image 4	0.686	0.930	0.916
Image 5	0.863	0.817	0.822
Image 6	0.922	0.819	0.827
Image 7	0.918	0.846	0.853
Image 8	0.927	0.851	0.857
Image 9	0.893	0.871	0.873
Image 10	0.909	0.835	0.841
Image 11	0.914	0.873	0.876
Image 12	0.919	0.878	0.882
Image 13	0.878	0.872	0.873
Image 14	0.881	0.874	0.875
Image 15	0.839	0.867	0.864
Image 16	0.835	0.903	0.896
Image 17	0.906	0.870	0.873
Image 18	0.816	0.897	0.893
Image 19	0.751	0.918	0.911
Image 20	0.745	0.913	0.902
<b>Average</b>	<b>0.859</b>	<b>0.867</b>	<b>0.867</b>

Table 3.26 Performance metrics obtained on DRIVE dataset using Line operator

<b>Image</b>	<b>Sensitivity</b>	<b>Specificity</b>	<b>Accuracy</b>
Image 1	0.793	0.982	0.965
Image 2	0.739	0.988	0.963
Image 3	0.715	0.978	0.952
Image 4	0.665	0.991	0.961
Image 5	0.703	0.986	0.960
Image 6	0.700	0.979	0.952
Image 7	0.688	0.980	0.953
Image 8	0.666	0.977	0.950
Image 9	0.730	0.977	0.957
Image 10	0.734	0.982	0.962
Image 11	0.696	0.984	0.958
Image 12	0.767	0.976	0.958
Image 13	0.706	0.982	0.955
Image 14	0.787	0.973	0.958
Image 15	0.774	0.976	0.962
Image 16	0.747	0.983	0.962
Image 17	0.755	0.978	0.959
Image 18	0.803	0.975	0.961
Image 19	0.858	0.983	0.973
Image 20	0.816	0.974	0.962
<b>Average</b>	<b>0.742</b>	<b>0.9810</b>	<b>0.9580</b>

Table 3.27 Performance metrics obtained on STARE dataset using Line operator

<b>Image</b>	<b>Sensitivity</b>	<b>Specificity</b>	<b>Accuracy</b>
Image 1	0.754	0.952	0.936
Image 2	0.709	0.946	0.930
Image 3	0.861	0.928	0.924
Image 4	0.792	0.955	0.943
Image 5	0.754	0.963	0.944
Image 6	0.853	0.957	0.950
Image 7	0.888	0.975	0.968
Image 8	0.901	0.970	0.965
Image 9	0.874	0.977	0.969
Image 10	0.853	0.951	0.943
Image 11	0.877	0.974	0.967
Image 12	0.888	0.982	0.974
Image 13	0.823	0.978	0.964
Image 14	0.824	0.978	0.964
Image 15	0.826	0.969	0.957
Image 16	0.731	0.977	0.951
Image 17	0.816	0.985	0.970
Image 18	0.811	0.978	0.969
Image 19	0.874	0.959	0.955
Image 20	0.802	0.950	0.940
<b>Average</b>	<b>0.825</b>	<b>0.966</b>	<b>0.9510</b>

Table 3.28 Performance metrics obtained on DRIVE dataset using Gabor wavelet

<b>Image</b>	<b>Sensitivity</b>	<b>Specificity</b>	<b>Accuracy</b>
Image 1	0.983	0.549	0.924
Image 2	0.975	0.562	0.916
Image 3	0.968	0.360	0.842
Image 4	0.982	0.141	0.474
Image 5	0.978	0.392	0.864
Image 6	0.972	0.419	0.874
Image 7	0.974	0.516	0.913
Image 8	0.983	0.136	0.491
Image 9	0.967	0.760	0.953
Image 10	0.983	0.342	0.854
Image 11	0.986	0.142	0.489
Image 12	0.976	0.537	0.923
Image 13	0.967	0.519	0.907
Image 14	0.980	0.511	0.922
Image 15	0.980	0.175	0.713
Image 16	0.974	0.743	0.953
Image 17	0.972	0.602	0.936
Image 18	0.979	0.667	0.951
Image 19	0.992	0.200	0.684
Image 20	0.992	0.132	0.540
<b>Average</b>	<b>0.978</b>	<b>0.420</b>	<b>0.806</b>

Table 3.29 Performance metrics obtained on STARE dataset using Gabor wavelet

<b>Image</b>	<b>Sensitivity</b>	<b>Specificity</b>	<b>Accuracy</b>
Image 1	0.961	0.569	0.934
Image 2	0.955	0.572	0.926
Image 3	0.948	0.380	0.865
Image 4	0.982	0.231	0.424
Image 5	0.934	0.452	0.887
Image 6	0.943	0.479	0.835
Image 7	0.920	0.586	0.924
Image 8	0.934	0.246	0.467
Image 9	0.951	0.800	0.965
Image 10	0.904	0.452	0.835
Image 11	0.916	0.242	0.456
Image 12	0.945	0.647	0.935
Image 13	0.923	0.629	0.913
Image 14	0.967	0.671	0.923
Image 15	0.957	0.245	0.721
Image 16	0.934	0.823	0.901
Image 17	0.952	0.762	0.912
Image 18	0.965	0.457	0.911
Image 19	0.976	0.340	0.578
Image 20	0.978	0.242	0.523
<b>Average</b>	<b>0.947</b>	<b>0.491</b>	<b>0.792</b>

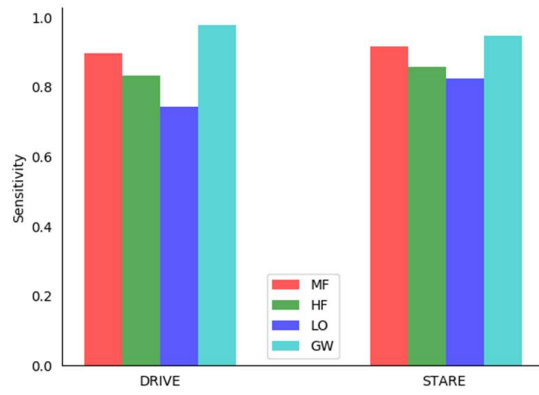


Fig. 3.10 Average Sensitivity results obtained using various vessel segmentation techniques on DRIVE and STARE datasets.

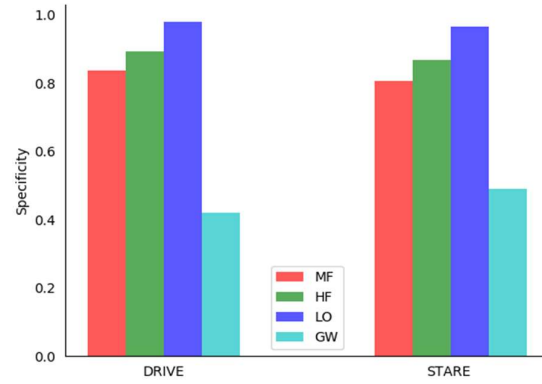


Fig. 3.11 Average Specificity results obtained using various vessel segmentation techniques on DRIVE and STARE datasets.

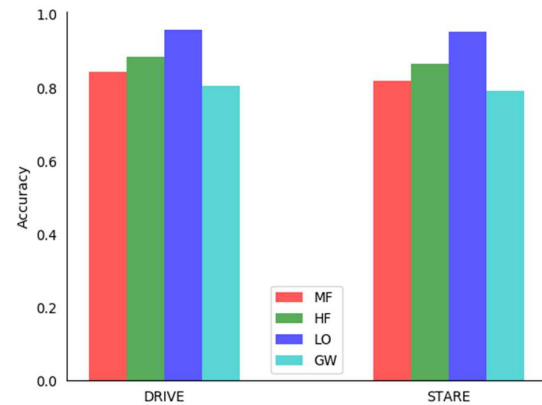


Fig. 3.12 Average Accuracy results obtained using various vessel segmentation techniques on DRIVE and STARE datasets.

### 3.4.2.2 Qualitative results

The effectiveness of the vessel segmentation techniques can be observed in Fig. 3.13 – 3.17. For visual inspection, one image from both the DRIVE and STARE dataset has been chosen and the same have been used by all the techniques to assess the capability of various techniques. As can be seen in Fig. 3.13 – 3.17, the techniques perform efficiently while extracting the vessels from the DRIVE image but their performance degrades while performing vessel extraction from the STARE image as the STARE dataset contain images which are affected by certain pathology. In case of Matched filter, Hybrid filter and Line operator, filters with various orientations are considered and then maximum modulus filter is chosen for each technique. One such filter (in case of matched filter) oriented at a particular angle is shown in Fig. 3.14.

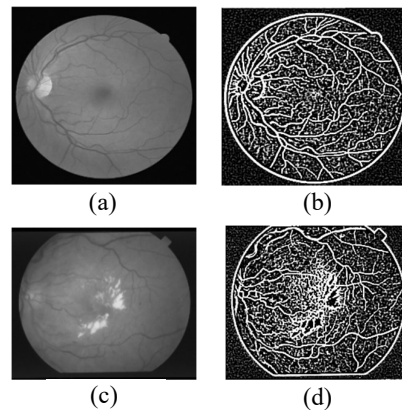


Fig. 3.13 Matched Filter (a) DRIVE image (b) Vessel segmented DRIVE image (c) STARE image (d) Vessel segmented STARE image

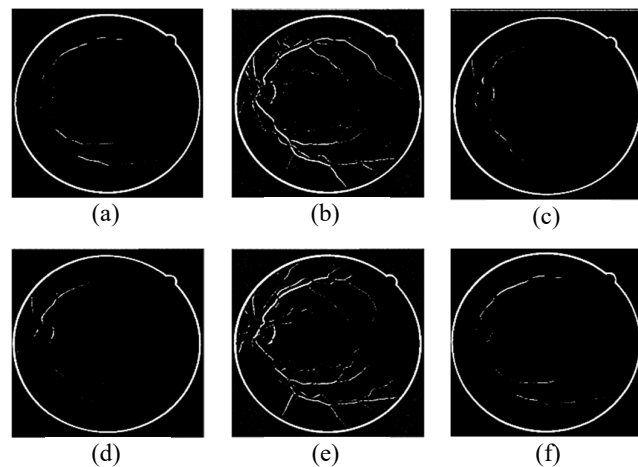


Fig. 3.14 Matched filter technique shows vessels extracted at (a)  $15^\circ$  (b)  $45^\circ$  (c)  $75^\circ$  (d)  $105^\circ$  (e)  $135^\circ$  (f)  $165^\circ$

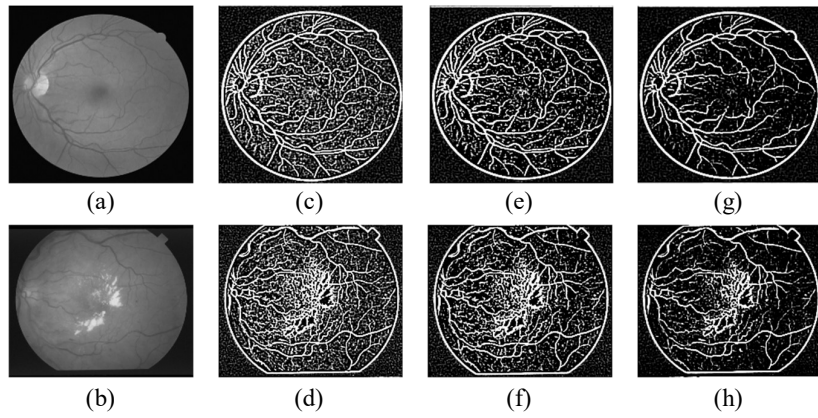


Fig. 3.15 (a), (b) Original images (DRIVE and STARE respectively), (c), (d) Corresponding vessel segmented images using matched filter, (e), (f) Corresponding vessel segmented images using DoG filter, (g), (h) Corresponding vessel segmented images using hybrid filter

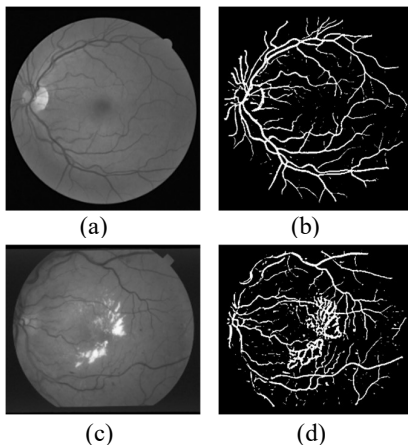


Fig. 3.16 Line Operator (a) DRIVE image (b) Vessel segmented DRIVE image (c) STARE image (d) Vessel segmented STARE image

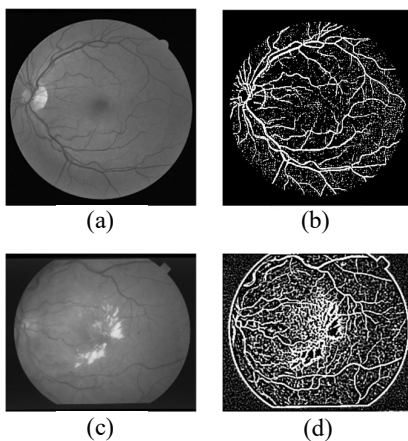


Fig. 3.17 (a) Original image (b) Gabor filter convolved maximum modulus image (c) Vessel segmented image

### **3.5 Chapter summary**

This chapter presents the comparative analysis of various image enhancement and vessel segmentation techniques. The performance comparison of various enhancement techniques such as HE, BBHE, BHEPL, DOTHE, RSIHE, QDHE, RSWHE has been done in terms of Entropy, SSIM, PSNR, and Euclidean distance whereas the evaluation of vessel extraction techniques has been done in terms of Sensitivity, Specificity, and Accuracy. Among various enhancement techniques, BHEPL exhibits superiority in terms of uniform illumination and entropy persistence over other techniques whereas more desirable results in terms of metrics such as SSIM and PSNR have been achieved in RSWHE. In the case of vessel segmentation techniques, Gabor wavelet demonstrate higher efficiency in the detection of vessel pixels but it suffers from very low detection rate of non-vessel pixels. Line operator performs better in terms of sensitivity, specificity, and accuracy than various other techniques discussed.



# **Chapter 4**

## **Development of Retinal Image Enhancement Technique**

---

---

### **4.1 Introduction**

As discussed earlier, there are various factors that affect the quality of the retinal image and as a result it gets affected by blurriness, low contrast, low and non-uniform radiance. Various techniques have been employed to address these consequences that happen in the retinal image. To the best of the authors knowledge and evident from the related work, very less work has been done to address the issue of low and improper illumination in retinal images that happens during image acquisition. These techniques just focuses on making the radiance uniform without taking into consideration the amount of radiance and the information content (entropy) already present in the image. It has been observed that even though the techniques succeed in getting a uniform radiance image but it comes at a cost of a high level loss of the entropy which is never desired especially in medical images as even a small loss of information content may lead to a totally different diagnosis. Also majority of the existing techniques suffer from over enhancement as a result of which the information content is badly affected. The proposed methods makes a conscious effort to take into account both the level of radiance and information content while enhancing the quality of retinal images to make them suitable for segmentation.

### **4.2 Proposed work**

This work focusses on the preprocessing step that deals with the improvement in the quality of the image in terms of illumination. In this work, a new histogram clipping algorithm has been proposed that takes care of the over enhancement. On the basis of the histogram clipping algorithm, two more techniques, RIHE-RVE (Radiance indicator based histogram equalization for retinal vessel enhancement) and RIHE-

RRVE (Radiance indicator based histogram equalization for recursive retinal vessel enhancement) have also been proposed to enhance the quality of images. In both the techniques, histogram is split based on the value of the tunable parameter,  $\psi$ , that controls the level of enhancement. RIHE-RVE separates the histogram into two sub-histograms, equalizes both the histograms and then integrates them. This is done repeatedly depending on the difference between radiance values obtained from successive enhanced images. RIHE-RRVE recursively divides the histogram into multiple number of sub-histograms depending on the level decided by the parameter,  $r$ . In addition to the above techniques, a new technique for clipping the histogram has also been proposed. Just by changing the value of the tunable parameter, level of enhancement can be controlled. The proposed techniques efficiently enhance the quality of low and non-uniformly illuminated images without any information loss. The techniques do not produce any unwanted artefacts, are robust in nature and can be applied to images of various types.

#### 4.2.1 Proposed Algorithms

The proposed algorithms determine the amount of under radiance that an image has and based on that performs the appropriate level of enhancement which results in a uniformly illuminated image with a very high value of entropy close to the original image. The techniques take care that under exposed regions are enhanced more than already high radiance regions. In the proposed work, a simple technique has been devised that can easily control the level of enhancement. For this purpose, a tunable parameter  $\psi$  is used to determine the split value that separates the histogram into sub histograms.

The split value,  $B_\psi$  is calculated as depicted in Eq. (4.1) – (4.4).

$$p_c(i) = h(i)/N \quad \text{for } 0 \leq i \leq L - 1. \quad (4.1)$$

$$C(k) = \sum_{i=0}^k p_c(i) \quad \text{for } 0 \leq k \leq L - 1. \quad (4.2)$$

$h$  is the histogram of the image,  $N$  is the total number of pixels in the image,  $L$  is the total number of intensity levels,  $p_c$  and  $C$  contains the normalized histogram counts and

cumulative normalized histogram counts respectively of the input image. The value of the controlling parameter,  $C_p$  is needed to be found such that

$$\sum_{j=0}^{C_p} C(j) \approx \psi \quad \text{for any } 0.1 \leq \psi \leq 0.9. \quad (4.3)$$

$$B_v = (L - 1) - C_p - 1. \quad (4.4)$$

The value of tunable parameter,  $\psi$  decides the level of enhancement needed for an image. Lesser the value of  $\psi$ , more is the enhancement. This holds true because lesser value of  $\psi$  will result in lower value of  $C_p$  as can be seen in Eq. (4.3). From Eq. (4.4), it can be induced that low  $C_p$  will produce large split value,  $B_v$  that separates the histogram into sub histograms. This process can be understood from the fact that for a low radiance image, pixel density of an image is more towards the lower intensity range of the histogram. Consequently, Eq. (3). can be satisfied with much lesser value of  $C_p$  for a particular value of  $\psi$  resulting in an extended first sub histogram. The first sub histogram is then equalized separately from the second sub histogram. Because of the extendedness of the sub histogram, a smaller intensity range of pixels of an input image is mapped to a much larger intensity range enhancing the low radiance region effectively. On the contrary, the second sub histogram has much lesser range and contains pixels that belong to the higher intensity range in an image. Because of the much smaller range, high end intensity pixels are therefore equalized in a much smaller range thus restricting over enhancement. In this work, three techniques have been proposed:

- Histogram Clipping
- RIHE-RVE
- RIHE-RRVE

#### 4.2.1.1 Histogram Clipping

Enhancing images often leads to the problem of over enhancement. In histogram clipping, a threshold value is used as the limiting value. The bin count greater than the

threshold value is reduced to the threshold value to reduce the effect of over enhancement and get a more natural image. In this work, a new histogram clipping algorithm is proposed. Histogram is clipped based on the averaged median value which better reduces the effect of over enhancement.

### ***Pseudocode for Histogram Clipping***

- (1) Rearrange histogram values in the ascending order.
- (2) Find unique values from the sorted list of values.
- (3) Calculate median value,  $M$  from the set of unique values where median is the middle value if the number of unique values are odd or it is the mean value of the middle two values if the number of unique values are even.
- (4) Calculate threshold value,

$$T_v = M/C_p \quad (4.5)$$

where  $C_p$  is the controlling parameter found in Eq. (4.3). The value of  $T_v$  must be rounded off to the nearest integer.

- (5) The threshold value,  $T_v$  found in Eq. (4.5) is used for clipping the histogram. All the values of the histogram,  $h$  higher than  $T_v$  are clipped to the value  $T_v$  to create a new histogram,  $h_N$ . The values lower than the value of the threshold value,  $T_v$  are not modified. This operation is shown in Eq. (4.6)

$$\text{Set } h_N = T_v \text{ if } h(i) \geq T_v \text{ else } h_N = h(i). \quad (4.6)$$

#### **4.2.1.2 Radiance indicator based histogram equalization for retinal vessel enhancement (RIHE-RVE)**

The algorithm calls itself recursively until the absolute difference between the successive radiance values,  $\chi_1$  and  $\chi_2$  (calculated using Eq. (4.7)) for input image and enhanced image respectively is less than the threshold error,  $s$ . In this work, value of  $s$  is chosen to be 0.001. The threshold value,  $s$ , should be chosen carefully such that it should not be too high which might lead to high computational time and should not be too less to avoid under enhancement. Fig. 4.1. shows the flow chart of RIHE-RVE.

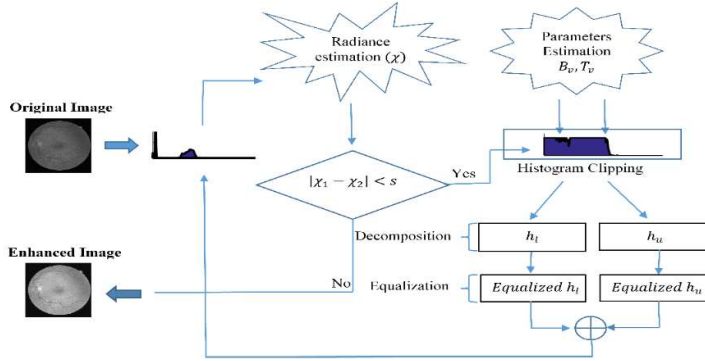


Fig. 4.1. Flowchart of RIHE-RVE technique

### **Algorithm for RIHE-RVE**

- (1) Compute the histogram,  $h$  for the input image,  $f$ , where a histogram contains the frequency of occurrence of each intensity level.
- (2) Compute the radiance value,  $\chi_1 = \frac{\sum_{i=0}^{L-1} h(i) \cdot i}{L \sum_{i=0}^{L-1} h(i)}$ . (4.7)  
where  $i$  represents the intensity value,  $h(i)$  is the frequency of occurrence of the intensity value  $i$  and  $L$  is the total number of intensity levels, here  $L = 256$ . This equation determines the amount of exposure present in the image.
- (3) Calculate the split value,  $B_v$  from Eq. (4.3) and (4.4) to divide the histogram in to sub histograms.
- (4) Calculate the threshold value,  $T_v$  from Eq. (4.5) for clipping the histogram to avoid over enhancement.
- (5) Clip the histogram  $h$  at threshold value  $T_v$  to obtain clipped histogram  $h_N$  from Eq. (6).
- (6) Separate the clipped histogram  $h_N$  into two sub-histograms  $h_l$  and  $h_u$  of intensity ranges  $0$  to  $B_v$  and  $B_v+1$  to  $L - 1$  respectively based on the split value  $B_v$  calculated in step 3 of the algorithm.
- (7) Equalize the two histograms  $h_l$  and  $h_u$  individually in their respective range of intensity. The darker regions will be enhanced more than the brighter regions.
- (8) Integrate  $h_l$  and  $h_u$  to re-create the histogram,  $h$ .
- (9) Repeat Step 2 to find the radiance value,  $\chi_2$  of the equalized image.
- (10) Apply steps 1-9 until the absolute difference between two consecutive radiance levels is less than the threshold error,  $s$  as shown in  $|\chi_1 - \chi_2| < s$ .

#### 4.2.1.3 Radiance indicator based histogram equalization for recursive retinal vessel enhancement (RIHE-RRVE)

RIHE-RRVE works by sub dividing the histogram into sub-histograms up to the chosen level of splitting,  $r$ . For  $r = 1$ ,  $2^1 = 2$  sub-histograms will be obtained at level 1, for  $r = 2$ ,  $2^2 = 4$  histograms will be obtained at level 2 and for  $r = n$ ,  $2^n$  sub-histograms will be obtained at level  $n$  (maximum value of  $n$  is chosen to be 7). The split values  $B_{vl}$  and  $B_{vu}$  for each of the sub-histograms are calculated as shown in Eq. (8) and Eq. (9)

$$B_{vl} = B_v - (C_p * (1 - \chi_1)) - 1. \quad (4.8)$$

$$B_{vu} = h_{u\_max} - (C_p * (1 - \chi_2)) - 1. \quad (4.9)$$

where  $h_{u\_max}$  denotes the maximum intensity value for the sub-histogram  $h_u$ . Fig. 4.2. shows the flow chart of RIHE-RRVE.

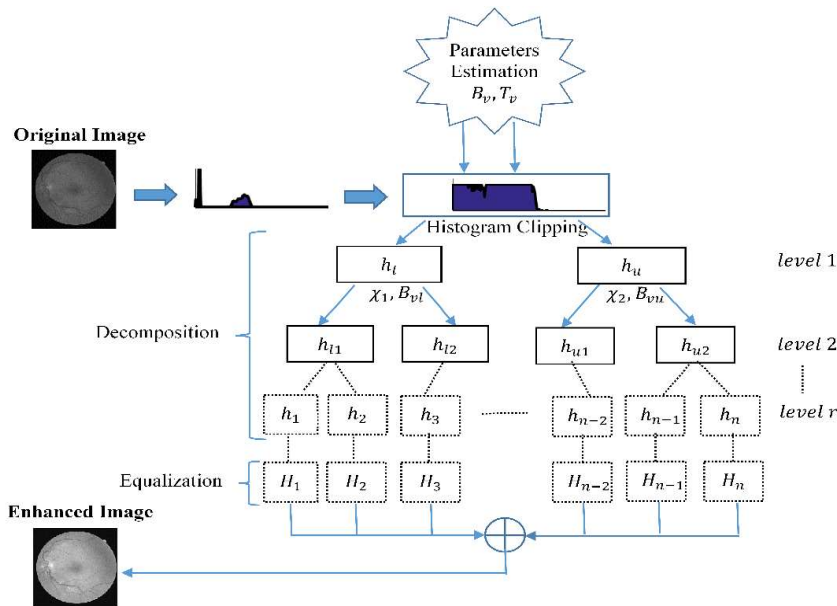


Fig. 4.2. Flowchart of RIHE-RRVE technique

#### Algorithm for RIHE-RRVE

- (1) Compute the histogram,  $h$  for the input image,  $f$ , where a histogram contains the frequency of occurrence of each intensity level.
- (2) Choose the level of splitting,  $r$ . Each histogram will be divided into two sub histograms iteratively upto the chosen level of decomposition. For the level,  $r$ , the

number of sub histograms generated will be  $2^r$ . Each histogram will be divided as shown in steps 3 – 9 of this algorithm.

- (3) Calculate the split value,  $B_v$  using Eq. (3) and (4) to divide the histogram in to sub histograms.
- (4) Calculate the threshold value,  $T_v$  using Eq. (5) for clipping the histogram to avoid over enhancement.
- (5) Clip the histogram  $h$  at threshold value  $T_v$  to obtain clipped histogram  $h_N$  from Eq. (6).
- (6) Divide the clipped histogram into two sub-histograms  $h_l$  and  $h_u$  based on  $B_v$  and compute newer split values  $B_{vl}$  and  $B_{vu}$  for  $h_l$  and  $h_u$  respectively from Eq. (8) and (9). These split values are used to further divide the histograms  $h_l$  and  $h_u$  into sub histograms.
- (7) Set  $B_v = B_{vl}$  to further sub divide  $h_l$  in to  $h_{l1}$  and  $h_{l2}$ . Once  $h_l$  is divided into  $h_{l1}$  and  $h_{l2}$  sub histograms, compute  $B_{vl}$  and  $B_{vu}$  for  $h_{l1}$  and  $h_{l2}$  respectively from Eq. (8) and (9) which will be further used to sub divide  $h_{l1}$  and  $h_{l2}$  into their respective sub histograms.
- (8) Set  $B_v = B_{vu}$  to further sub divide  $h_u$  in to  $h_{u1}$  and  $h_{u2}$ . Once  $h_u$  is divided into  $h_{u1}$  and  $h_{u2}$  sub histograms, compute  $B_{vl}$  and  $B_{vu}$  for  $h_{u1}$  and  $h_{u2}$  respectively from Eq. (8) and (9) which will be further used to sub divide  $h_{u1}$  and  $h_{u2}$  into their respective sub histograms.
- (9) Repeat the steps 7 and 8 to recursively separate the histograms in to sub-histograms up to the required level of splitting.
- (10) Equalize all the sub-histogram individually in their respective range of intensities and integrate them to get the final equalized histogram.

The performance of both the techniques is affected by the change in the values of the parameters. RIHE-RVE depends on the tuneable parameter,  $\psi$  whereas RIHE-RRVE depends on both the tuneable parameter,  $\psi$  and level of splitting,  $r$ . The effect can be seen in Fig. 4.3.

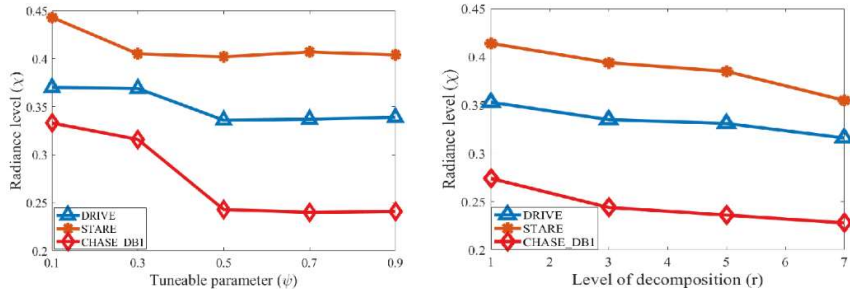


Fig. 4.3. (a) Effect of tunable parameter ' $\psi$ ' on the amount of radiance (RIHE-RVE) (b) Effect of split level ' $r$ ' on the amount of radiance (RIHE-RRVE). The mean of radiance values obtained for different values of ' $\psi$ ' for each level is used to calculate it.

### 4.3 Experimental Results

In this section the results of the proposed methods are compared with the existing techniques i.e. BBHE (Yeong-Taeg Kim, 1997), BHEPL (Ooi et al., 2009), DOTHE (K. Singh et al., 2016), RESIHE (K. Singh, Kapoor, & Sinha, 2015) and MARIN (Marín et al., 2011). All the methods are robust in nature in the sense that they can be applied to any type of image except the last one which works specifically for retinal images.

#### 4.3.1 Dataset used

Performance evaluation of the techniques has been done on the publicly available datasets namely, DRIVE, STARE, CHASE\_DB1 and OASIS. Detailed information about these datasets has already been provided earlier and can be found under section 2.9.

#### 4.3.2 Performance evaluation based on visual inspection

The effectiveness of the methods can be seen in Fig. 4.4 – 4.7. Visual analysis shows that the images enhanced by the proposed methods have a high and uniform radiance such that the details are clearly visible. On the other hand, BBHE, RESIHE, BHEPL, DOTHE and MARIN are able to increase the radiance of the images to a certain extent but the radiance is not uniform which can be easily seen in the seen images. There is a high level of radiance at the center of the images which gradually decreases towards the image boundary thus making the identification of pixel content impossible. MARIN is able to provide uniform radiance but at the cost of high degree of information loss which is not acceptable in the medical domain. Therefore we can conclude that the

proposed techniques not only perform better than the other state-of-the-art techniques but also better than BHEPL which achieved best overall performance when various image enhancement techniques were analyzed in the earlier chapter.

#### 4.3.3 Performance evaluation based on objective information

The algorithmic performance of the proposed methods has been measured in terms of Entropy, SSIM, PSNR and Euclidean distance. It has been empirically found that RIHE-RVE gives a highly illuminated image with uniform radiance at  $\psi = 0.1$  whereas for RIHE-RRVE, the optimal values are  $r = 1$  and  $\psi = 0.2$ . Fig. 4.2 shows the effect of ' $\psi$ ' and ' $r$ ' on the level of radiance for different retinal databases. It can be observed from Fig. 4.4 – 4.7 that there is no over enhancement in images enhanced by the proposed techniques in contrary to some of the existing techniques. Results of various methods using two random images from each database are tabulated in Tables 4.1 – 4.4 (where 1<sup>st</sup> pair of images belongs to the CHASE dataset, 2<sup>nd</sup> pair belongs to DRIVE, 3<sup>rd</sup> to STARE and 4<sup>th</sup> to OASIS dataset).

Table 4.1: Performance comparison based on Entropy

Images	Original	BBHE	RESIHE	BHEPL	DOTHE	MARIN	RIHE-RVE	RIHE-RRVE
Image 1	5.752	5.467	5.654	5.661	5.448	4.006	<b>5.719</b>	<b>5.719</b>
Image 2	5.782	5.575	5.678	5.702	5.564	4.168	<b>5.758</b>	<b>5.758</b>
Image 3	5.302	5.199	5.264	5.277	4.976	3.991	<b>5.302</b>	<b>5.302</b>
Image 4	5.510	5.379	5.453	5.468	5.160	4.259	<b>5.509</b>	<b>5.509</b>
Image 5	6.549	6.453	6.493	6.503	6.268	3.993	<b>6.544</b>	<b>6.546</b>
Image 6	6.530	6.446	6.490	6.495	6.239	4.247	<b>6.523</b>	<b>6.526</b>
Image 7	6.182	5.809	6.077	<b>6.093</b>	5.921	-	6.060	6.060
Image 8	6.416	6.124	6.345	6.343	6.257	-	<b>6.380</b>	<b>6.408</b>

Table 4.2: Performance comparison based on SSIM

Images	BBHE	RESIHE	BHEPL	DOTHE	MARIN	RIHE-RVE	RIHE-RRVE
Image 1	0.492	0.787	<b>0.826</b>	0.742	0.784	0.786	0.787
Image 2	0.536	0.821	0.840	0.792	0.820	<b>0.847</b>	<b>0.848</b>
Image 3	0.381	0.657	0.516	0.443	0.635	<b>0.790</b>	<b>0.801</b>
Image 4	0.392	0.738	0.546	0.461	0.638	<b>0.933</b>	<b>0.934</b>
Image 5	0.755	0.836	0.825	0.759	0.596	<b>0.967</b>	<b>0.983</b>
Image 6	0.756	0.836	0.836	0.754	0.575	<b>0.939</b>	<b>0.963</b>
Image 7	0.514	0.723	<b>0.795</b>	0.567	-	0.606	0.608
Image 8	0.530	0.625	0.789	0.525	-	0.591	<b>0.793</b>

Table 4.3: Performance comparison based on PSNR

Images	BBHE	RESIHE	BHEPL	DOTHE	MARIN	RIHE-RVE	RIHE-RRVE
Image 1	12.292	<b>16.839</b>	16.642	14.494	13.715	16.444	16.537
Image 2	13.077	<b>21.784</b>	17.521	15.300	14.771	21.477	21.616
Image 3	10.725	16.370	11.407	12.581	<b>23.275</b>	12.724	12.840
Image 4	11.021	19.619	12.705	12.972	<b>20.308</b>	19.510	19.651
Image 5	15.062	17.300	15.439	16.298	12.754	<b>26.953</b>	<b>29.875</b>
Image 6	15.254	18.443	17.238	16.219	12.032	<b>23.138</b>	<b>25.088</b>
Image 7	13.284	14.745	<b>16.298</b>	12.092	-	11.214	11.277
Image 8	12.002	13.381	16.964	10.495	-	12.763	<b>18.073</b>

Table 4.4: Performance comparison based on Euclidean distance

Images	BBHE	RESIHE	BHEPL	DOTHE	MARIN	RIHE-RVE	RIHE-RRVE
Image 1	0.413	0.411	0.406	<b>0.080</b>	0.191	0.411	0.411
Image 2	0.411	0.407	0.403	<b>0.079</b>	0.166	0.406	0.406
Image 3	0.285	<b>0.281</b>	0.287	0.328	0.394	0.292	0.292
Image 4	0.271	<b>0.262</b>	0.272	0.309	0.374	0.263	0.263
Image 5	0.126	0.132	0.129	0.143	0.363	<b>0.095</b>	<b>0.085</b>
Image 6	0.130	0.125	0.126	0.143	0.351	<b>0.109</b>	<b>0.094</b>
Image 7	0.313	0.309	<b>0.307</b>	0.321	-	0.311	0.311
Image 8	<b>0.154</b>	0.174	0.156	0.168	-	0.177	0.166

Average results in terms of Entropy, SSIM, PSNR and Euclidean distance are presented in Table 4.5 – 4.7. The average results are obtained only for retinal images using all the test images of various retinal datasets. A high value of entropy as close as possible to the original image is desired. Higher value of SSIM and lower value of Euclidean distance indicates that the image is closer to the original image. A higher value of PSNR indicates the presence of lesser noise. The running time comparison of various algorithms has been made in Table 4.8. The time has been calculated by executing each algorithm 10 times and taking the average of the time taken to execute the algorithm. RIHE\_RRVE records the lowest running time of 17 ms whereas RIHE\_RVE records high running time of 38 ms. Large running time of RIHE\_RVE is due to the iterative nature of the algorithm as the algorithm goes on equalizing the image until the difference between consecutive radiance levels becomes greater than the threshold error.

Table 4.5: Average results for DRIVE database

Statistical Index	BBHE	RESIHE	BHEPL	DOTHE	MARIN	RIHE-RVE	RIHE-RRVE
Entropy	5.572	5.648	5.672	5.348	4.316	<b>5.717</b>	<b>5.727</b>
SSIM	0.478	0.775	0.638	0.508	0.627	<b>0.964</b>	<b>0.968</b>
PSNR	12.806	20.263	15.140	14.567	19.491	<b>29.336</b>	<b>30.474</b>
Euclidean	0.256	0.236	0.255	0.294	0.372	<b>0.198</b>	<b>0.194</b>

Table 4.6: Average results for STARE database

Statistical Index	BBHE	RESIHE	BHEPL	DOTHE	MARIN	RIHE-RVE	RIHE-RRVE
Entropy	6.628	6.672	6.702	6.365	4.370	<b>6.733</b>	<b>6.761</b>
SSIM	0.766	0.893	0.856	0.659	0.633	<b>0.967</b>	<b>0.976</b>
PSNR	15.014	22.304	16.791	15.640	16.256	<b>26.435</b>	<b>27.789</b>
Euclidean	0.119	0.097	0.113	0.147	0.322	<b>0.082</b>	<b>0.071</b>

Table 4.7: Average results for CHASE database

Statistical Index	BBHE	RESIHE	BHEPL	DOTHE	MARIN	RIHE-RVE	RIHE-RRVE
Entropy	5.479	5.610	5.634	5.459	4.061	<b>5.665</b>	<b>5.665</b>
SSIM	0.516	0.808	0.811	0.761	0.805	0.806	<b>0.814</b>
PSNR	12.548	<b>20.615</b>	16.616	15.256	16.271	17.671	17.783
Euclidean	<b>0.415</b>	0.411	0.410	0.086	0.173	0.412	0.412

Table 4.8: Comparison of average running time of various methods

Method	Running time (ms)
BBHE	30
RESIHE	18
BHEPL	29
DOTHE	53
MARIN	29
RIHE-RVE	38
RIHE-RRVE	<b>17</b>

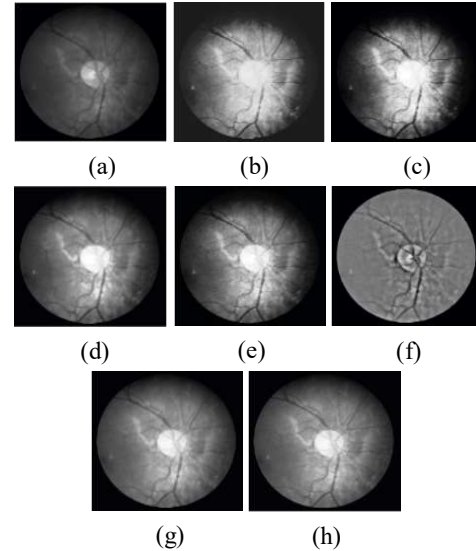


Fig. 4.4. (a) Original image (CHASE) (b) BBHE (c) DOTHE (d) RESIHE (e) BHEPL (f) MARIN (g) RIHE-RVE ( $\psi = 0.1$ ) (h) RIHE-RRVE ( $r = 1, \psi = 0.2$ )

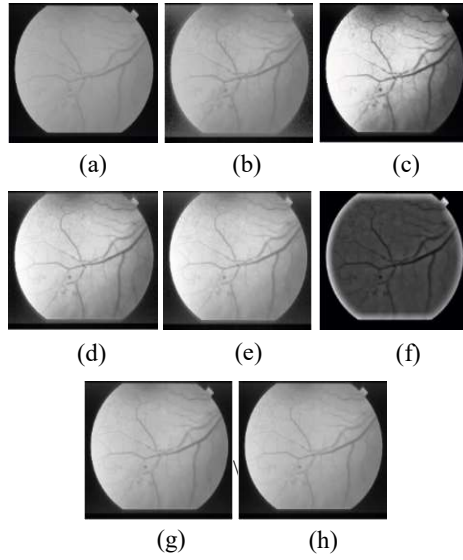


Fig. 4.5. (a) Original image (STARE) (b) BBHE (c) DOTHE (d) RESIHE (e) BHEPL (f) MARIN (g) RIHE-RVE ( $\psi = 0.1$ ) (h) RIHE-RRVE ( $r = 1, \psi = 0.2$ )

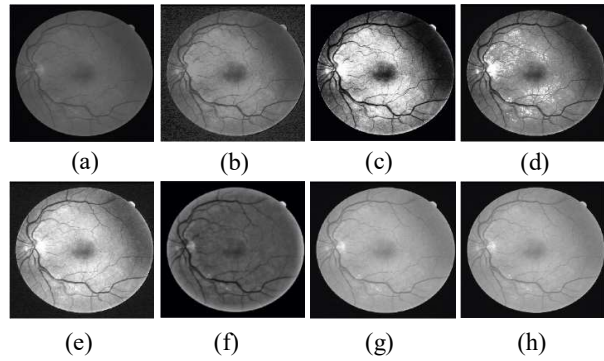


Fig. 4.6. (a) Original image (DRIVE) (b) BBHE (c) DOTHE (d) RESIHE (e) BHEPL (f) MARIN (g) RIHE-RVE ( $\psi = 0.1$ ) (h) RIHE-RRVE ( $r = 1, \psi = 0.2$ )

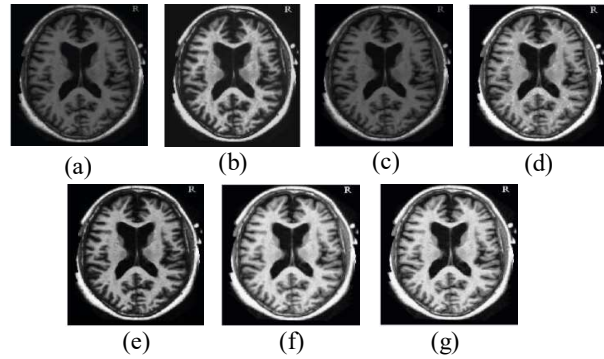


Fig. 4.7. MRI images have been taken to test the robustness of the proposed techniques. (a) Original image (OASIS) (b) BBHE (c) DOTHE (d) RESIHE (e) BHEPL (f) RIHE-RVE ( $\psi = 0.1$ ) (g) RIHE-RRVE ( $r = 1, \psi = 0.2$ ). (MARIN work only for retinal images).

The proposed techniques work using divide and conquer algorithm, separating the histogram into sub histograms which are then equalized locally to avoid over enhancement. The techniques can effectively enhance the quality of an image and this high quality image is used in computer aided diagnosis (CAD) of diabetic retinopathy. In CAD, the vessels are automatically extracted from the enhanced image. The blood vascular structure is then studied to ascertain the severity of the disease. If the vascular structure has bulges in it and has high tortuosity, it gives an early indication of the beginning of diabetic retinopathy which if not treated timely can lead to severe diabetic retinopathy which may even cause permanent blindness. The proposed work focusses on the enhancement of retinal images and there are certain important aspects associated with it. Among them, the most important is choosing the correct split value to separate the histogram into sub histograms for illuminating the under exposed regions. The most significant aspect associated with the techniques is that not all the portions of the image are equally enhanced rather the darker regions are illuminated more in comparison to the already illuminated regions. Experimental results demonstrate that a higher level of radiance can be achieved for lower values of the parameter  $\psi$  but the amount of illumination attained in the image comes at the cost of information. A higher level of illumination results in higher information loss and this loss in information can be reduced by fine tuning the parameter,  $\psi$ . It has been observed that a higher value of the tuneable parameter results in minimum information loss. Further, it has been observed that the proposed techniques not only provide better uniform illumination but also retains maximum information than the existing state of the art methods even at the lowest value of the tunable parameter. The threshold error,  $s$  also plays a very important role in controlling the amount of radiance in the image. A higher value of  $s$  results in over enhancement of the image and a lower values results in under enhancement. Therefore, an optimal value needs to be chosen to perform the right amount of enhancement in the image. A sincere effort has been made to ascertain the effect of the level of decomposition on the amount of illumination and it has been observed that as the level of decomposition increases the amount of illumination decreases. Furthermore, the information loss also decreases with the increase in the level of decomposition of the histogram. It has been observed that the techniques are affected by the variation in the amount of intensity levels in the background of the image. This effect can be seen on the CHASE\_DB1 dataset (it contains images of persons belonging

to different ethnicity with highly varied background images) as shown in the Table 4.7. Still the proposed techniques are able to perform better in terms of two metrics, Entropy and SSIM. No existing technique exhibit superior performance on this dataset in terms of the majority of metrics. We are highly motivated to address this issue in the future work. The results support the fact that the techniques are robust in nature and are efficient in handling different types of images.

#### **4.4 Chapter summary**

In order to inspect the vascular structure, first of all it needs to be extracted from the retina through an automatic process as manual segmentation is a very time consuming process. Accurate segmentation or extraction of the retinal vascular structure can only be done if the image is of high quality. Generally, retinal images are affected with improper illumination which occurs during image acquisition and it leads to improper extraction of the blood vessels from the retina. Inappropriate extraction sometimes leads to wrong diagnosis of the disease which can be life threatening. In this paper, two tunable enhancement techniques, RIHE-RVE and RIHE-RRVE have been proposed to address the problem of non-uniform illumination in retinal images to make the images better suited for computer aided diagnosis (CAD). To avoid over enhancement a new histogram clipping algorithm has also been proposed. Performance metrics show that the proposed techniques outperforms most of the state of the art techniques. The future work will focus on the extension of the proposed techniques for 3D retinal and MRI scans.

# **Chapter 5**

## **Development of an improved retinal blood vessel segmentation technique**

---

---

### **5.1 Introduction**

Retinal blood vessel segmentation is an important topic of research as it is directly related with the diagnosis and treatment of various serious diseases. Although a lot of progress has been made in this direction, segmentation of the retinal blood vessels still remains a challenge. This is due to various factors such as improper illumination, low contrast between blood vessels and the background, varying tortuosity and diameters of blood vessels and presence of various pathological features such as lesions, micro aneurysms, and exudates, etc. that may produce unwanted artifacts during segmentation. In this work, a novel supervised blood vessel segmentation technique to extract blood vessels from a retinal image has been proposed. The novelty of the work is the use of feature-oriented dictionary learning (FDL) and sparse coding in the accurate classification of the pixels of an image.

### **5.2 Proposed work**

The proposed work consists of three steps; In the first step, the image is split into patches, then for each patch, Gabor features are extracted at multiple scales and orientations to create a set of feature vectors (it is done for the whole training set) and an overcomplete feature-oriented dictionary is learned from the obtained Gabor features (selected on the basis of standard deviation) using KSVD dictionary learning technique. In the final step, Sparse representations are subsequently calculated for the corresponding features from the dictionary. A combination of feature vectors and sparse representations is then used by the ensemble classifier for the classification of pixels into either blood vessel pixels or non-blood vessel pixels.

### 5.2.1 Sparse representation model

In order for the readers to better understand the proposed technique, we first describe the basic idea of sparse representation. The fundamental aim of sparse representation is to represent a signal by a linear combination of a few atoms(Elad & Aharon, 2006). An overcomplete dictionary containing more number of atoms than the signal dimension is created from the patches of the image. Overlapping patches of size  $\sqrt{n} \times \sqrt{n}$  are ordered lexicographically in the dictionary,  $D$ , to create column vectors,  $\psi_i$  (atoms) where  $\psi_i \in \mathbb{R}^n$ . The main idea of sparse modelling is to represent the patch  $\phi_p$  sparsely over the learned dictionary  $D = \{\psi_1, \psi_2, \psi_3, \dots, \psi_m\}$  where  $D \in \mathbb{R}^{n \times m}$  such that the sparse representation,  $\alpha$  where  $\alpha \in \mathbb{R}^m$  is indeed very sparse,  $\|\alpha\|_0 \ll m$ , that is

$$\hat{\alpha} = \arg \min_{\alpha} \|\alpha\|_0 \text{ subject to } D\alpha \approx \phi_p \quad (5.1)$$

The constraint  $D\alpha \approx \phi_p$  can be defined by fixing the amount of error,  $\epsilon$  allowed between observed and recovered signal i.e.  $\|D\alpha - \phi_p\|_2 \leq \epsilon$ . Thus  $l_0 - norm$  in (1) can be replaced with  $l_2 - norm$  to get,

$$\hat{\alpha} = \arg \min_{\alpha} \|\alpha\|_0 \text{ subject to } \|D\alpha - \phi_p\|_2^2 \leq \epsilon \quad (5.2)$$

A simplified optimization task corresponding to Eq. (2) is

$$\hat{\alpha} = \arg \min_{\alpha} \|D\alpha - \phi_p\|_2 + \beta \|\alpha\|_0 \quad (5.3)$$

where  $\|\alpha\|_0$  is the penalty term and  $\beta$  is the lagrange constant.

A lot of work has been done in the field of image processing and computer vision using the sparse representation of the signals especially in the field of image denoising (K. Singh, Gupta, & Kapoor, 2015) (K. Singh, Kapoor, & Nayar, 2015)(K. Singh, Vishwakarma, & Walia, 2019). In this work, sparse representation has been used for retinal vessel segmentation.

### 5.2.2 Proposed Technique

The technique proposed in this paper belongs to the category of supervised classification. It mainly consists of pre-processing, patch extraction, Gabor feature calculation, dictionary learning and sparse coding besides post-processing in which the impulse noise is removed. The block diagram of the proposed methodology is presented in Fig. 5.1.

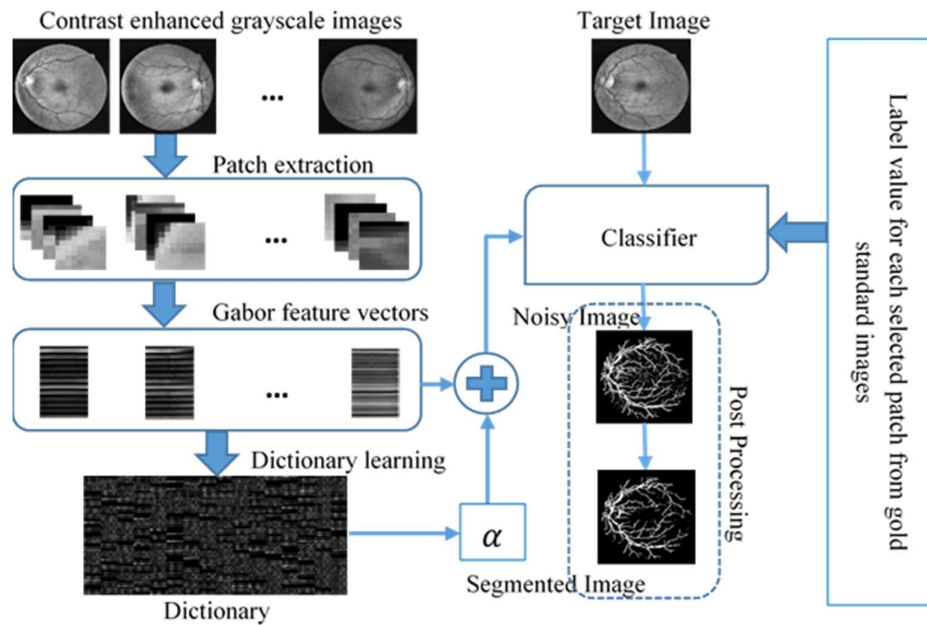


Fig. 5.1. Block diagram of the proposed technique

#### 5.2.2.1 Pre-processing

The dominant factor that affects the segmentation of blood vessels in the retinal images is the low contrast between the blood vessels and the background. The problem of low contrast is taken care of in two steps. First, the image is converted into the grayscale image and then a combination of RIHE-RVE (Radiance indicator based histogram equalization for retinal vessel enhancement) (N. Singh, Kaur, & Singh, 2019) and Contrast limited adaptive histogram equalization (CLAHE) (Zuiderveld, 1994) is applied on the image to increase its contrast (Please see Fig. 5.2). Sometimes some noise is present in the non-fundus area of the image which is removed by masking the

image with the mask of the corresponding image so that unwanted artefacts are not produced during the segmentation of blood vessels.

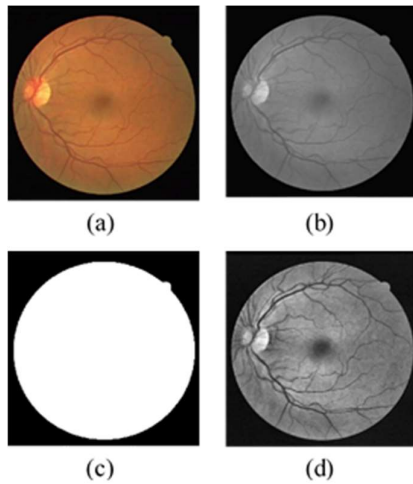


Fig. 5.2. (a) Original image, (b) Grayscale image, (c) Image mask and (d) Contrast-enhanced image

### 5.2.2.2 Patch and feature extraction

Image patches are the sub-regions of an image that forms the basis of various approaches under computer vision and have wide applicability ranging from object detection to texture classification. In patch extraction, a large number of overlapping patches of size  $p \times p$  (where patch size,  $p = 9$ ) chosen using a grid-search and cross-validation on the training sets are randomly extracted from various images of the training sets of both the datasets. Fig. 5.3 shows various patches extracted from the images. Once the patches are extracted, the filtering operation is applied on each patch to obtain a feature vector corresponding to it. There are several multi-scale filters that have been extensively used in image processing. In the present work, the Gabor filter has been chosen to extract the features because of its strong discriminatory power, orientation selectiveness, and fine-tuning capability to specific scales and frequencies. The most important thing about Gabor filters is that they are robust in nature in a sense that photometric effects such as improper illumination do not affect them(Haghigat, Zonouz, & Abdel-Mottaleb, 2015). The 2-D Gabor filter can be defined as a Gaussian modulated kernel which is modulated by a complex sine wave as follows(Haghigat et al., 2015):

$$G(x, y) = \frac{f^2}{\pi\gamma\eta} \exp\left(-\frac{1}{2}\left(\frac{x'^2}{\sigma_x^2} + \frac{y'^2}{\sigma_y^2}\right)\right) \exp(j2\pi f x' + \phi) \quad (5.4)$$

$$x' = x\cos\theta + y\sin\theta \quad (5.5)$$

$$y' = -x\sin\theta + y\cos\theta \quad (5.6)$$

where  $\theta$  is the orientation,  $f$  is the frequency,  $\sigma$  is the standard deviation,  $\gamma$  is the aspect ratio,  $\eta$  is the orthogonal width and  $\phi$  is the phase offset. In this work, 2 scales and 6 orientations are used to obtain 12 Gabor filters of size  $7 \times 7$ . Fig. 5.4 shows Gabor filters created at different scales and orientations. The combination of 12 Gabor filters (with 6 Gabor filters obtained at each scale, as there are 2 scales) is applied to each of the extracted patches to obtain a feature image. Since there is a high correlation between adjacent pixels in an image, the downsampling of the feature image is done to reduce the information redundancy(Chengjun Liu & Wechsler, 2002)(Shen, Bai, & Fairhurst, 2007). Each feature image is down sampled by a factor of 4 in both the horizontal and vertical direction, which means now the size of feature image will be reduced by a factor of 16 ( $= 4 \times 4$ ) to obtain a feature vector,  $G_f$ , where  $G_f \in \mathbb{R}^g$ . The standard deviation of each of the obtained Gabor feature vector is determined and only those feature vectors are retained which have a non-zero standard deviation. A non-zero value of standard deviation is used to select only those vectors which correspond to the fundus region of the image. All the feature vectors that correspond to the non-fundus region of the image are ignored. In this work, the value for the standard deviation is chosen to be 0.001. Among these feature vectors, a total of  $2N$  feature vectors are chosen randomly in such a way that  $N$  feature vectors corresponds to vessel class and the other  $N$  feature vectors corresponds to non-vessel class, where  $N$  is set to 140000. The feature vectors whose central pixel is marked as vessel pixel in the corresponding location of the corresponding ground truth images belong to vessel class otherwise to non-vessel class. Further, it has been ensured that among  $N$  features, half features ( $\frac{N}{2}$ ) belongs to DRIVE dataset and half to STARE dataset so as to provide balanced training on both the datasets(Birgui Sekou, Hidane, Olivier, & Cardot, 2017). The feature vectors thus obtained are normalized to zero mean and unit standard deviation to get a data matrix,  $d_t \in \mathbb{R}^{g \times \gamma}$ , where  $\gamma = 2N$ . Various parametric values used for Gabor filtering operation are presented in Table 5.1.

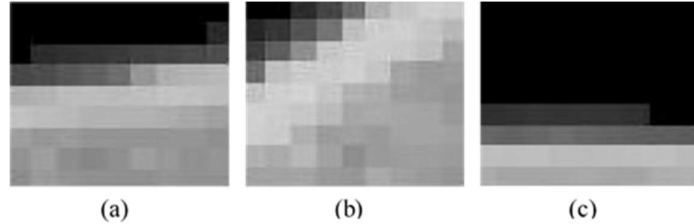


Fig. 5.3. Patches extracted from the images (patch size,  $p = 9$ )

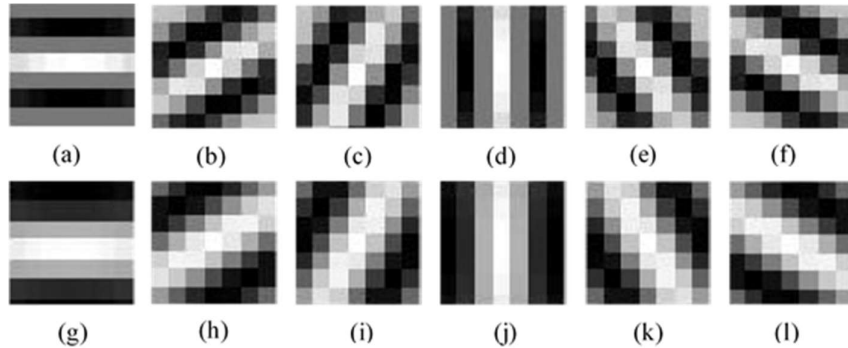


Fig. 5.4. Gabor filters in six orientations and two scales

Table 5.1: The values of parameters employed for Gabor filter

Parameter	Value
$\theta$	$0^\circ, 30^\circ, 60^\circ, 90^\circ, 120^\circ, 150^\circ$
$\phi$	0
$\gamma$	$\sqrt{2}$
$\eta$	$\sqrt{2}$
$f$	$0.25/(\sqrt{2}^{s-1})$
$s(\text{scale})$	{1,3}
$\sigma_x, \sigma_y$	$\sqrt{2}/f$

### 5.2.2.3 Dictionary Learning

A dictionary,  $D = \{\psi_1, \psi_2, \psi_3 \dots \psi_m\} \in \mathbb{R}^{g \times m}$  is learned from a set of Gabor feature vectors, contained in the data matrix,  $d_t = \{\phi_{p1}, \phi_{p2}, \dots \phi_{pk}\}$ . Each column of  $d_t$  contains the Gabor features of a patch obtained by applying the Gabor filter at different scales and orientations. KSVD (Elad & Aharon, 2006) (Rubinstein, Zibulevsky, & Elad, 2010) algorithm is used in this work for dictionary learning because of its simplicity and ease of implementation. Another advantage of using the KSVD technique is that it has a strong noise rejection capability. The KSVD Matlab

code used in the proposed technique for dictionary learning is taken from <http://www.cs.technion.ac.il/~elad/software>. KSVD has two modes of operation: sparsity-based and error-based optimization mode (Rubinstein, Zibulevsky, & Elad, 2008). The optimization for sparsity constrained coding problem is given by (Rubinstein et al., 2008):

$$\min_{D,\alpha} |\phi_{pi} - D\alpha|_2^2 \quad \text{subject to} \quad |\alpha_i|_0 \leq T \quad (5.7)$$

where  $T$  is the target sparsity.

Error constrained coding problem is given by [1]:

$$\min_{D,\alpha} |\alpha_i|_0 \quad \text{subject to} \quad |\phi_{pi} - D\alpha_i|_2^2 \leq \epsilon \quad (5.8)$$

where  $\epsilon$  is the target error.

In this work, error constrained optimization is used for dictionary learning. A typical dictionary learned from Gabor features is shown in Fig. 5.1. The three parameters i.e. dictionary size (the number of atoms) in the dictionary, target error ( $\epsilon$ ) and a number of iterations play a very important part in dictionary learning and therefore must be chosen very carefully. Though larger dictionaries better represent the data still smaller dictionaries are preferred as learning is a computationally intensive process and secondly with the use of smaller dictionaries overall image treatment is simplified as smaller dictionaries entail a locality of the resulting algorithm. Target error should not be too large so that it affects the overall learning of the dictionary resulting in a partially or inappropriately learned dictionary. On the other hand, it should not be too small that a huge amount of time is involved in dictionary learning. A number of iterations control the level of relearning. A more optimized dictionary is obtained with a higher number of iterations but on the other hand, increasing the number of iterations increases time consumption. For these reasons, the size of the dictionary is purposely chosen to be 256, target error is set to  $1e - 15$  and only 1 iteration of the dictionary is deployed (Rubinstein et al., 2008) (Tropp & Gilbert, 2007).

#### 5.2.2.4 Sparse coefficient calculation

Once the dictionary is learned from the Gabor features of various patches, the next step is to perform  $l^2$  – normalization of the atoms to zero mean and unit standard deviation. Calculation of sparse coefficient vector,  $\hat{\alpha}$ , for each of the data feature vector using the dictionary, D, follows normalization of the atoms. Solving Eq. (3) gives the required sparse coefficient vector,  $\hat{\alpha}$ . There are various efficient and tractable solutions to calculate the sparse representation,  $\hat{\alpha}$  such as basis pursuit (BP), Cholesky decomposition, orthogonal matching pursuit (OMP) (Tropp & Gilbert, 2007) and batch orthogonal matching pursuit (B-OMP). In the present work, OMP is chosen because of its simplicity, efficiency and easy parameter tuning. OMP is a greedy algorithm that uses the linear combination of the best fit atoms to represent the data vector,  $\phi_{p_k}$ . An atom is said to be a best fit if it is strongly correlated to the data vector as denoted by Eq (9).

$$\vartheta = \arg \max_{i=1,2,\dots,m} |\langle \phi_{p_k}, \psi_i \rangle| \quad (5.9)$$

where  $\psi_i$  represents an atom of the dictionary, D and  $\vartheta$  is the index of the chosen atom,  $\psi_i$ . Once the atom,  $\psi_\vartheta$  is selected based on the index,  $\vartheta$ , its contribution is subtracted from the data vector to obtain the residual,  $r$  as represented in Eq. (10).

$$r = \phi_{p_k} - \psi_\vartheta \hat{\alpha}_k \quad (5.10)$$

such that

$$\hat{\alpha}_k = \arg \min_{\alpha} |\psi_\vartheta \alpha - \phi_{p_k}| \quad (5.11)$$

The next atom which is close to the residual,  $r$  is then found and this process is repeated until a complete sparse representation,  $\alpha$  corresponding to the training data,  $d_t$  is obtained.

#### 5.2.2.5 Feature vector generation

The sparse coefficient vector,  $\hat{\alpha}_k$ , calculated from the dictionary using OMP, is concatenated with the Gabor feature vector,  $G_f$ , obtained in section 4.3 to obtain a full feature vector,  $F_v$  i.e

$$F_v = G_f + \hat{\alpha}_k \quad (5.12)$$

where  $G_f \in \mathbb{R}^g$ , and each coefficient vector  $\hat{\alpha}_k \in \mathbb{R}^m$ , the size of which depends on the size of the dictionary,  $D$ . So for the dictionary,  $D \in \mathbb{R}^{g \times m}$ , and data matrix,  $d_t \in \mathbb{R}^{g \times \gamma}$ , we obtain a complete sparse representation matrix,  $\alpha \in \mathbb{R}^{m \times \gamma}$ . Overall, the training matrix,  $T_m$ , obtained for the data matrix,  $d_t$  is

$$T_m = \begin{bmatrix} G_{f1}, G_{f1}, G_{f13}, \dots \dots \dots & G_{f1\gamma} \\ G_{f21}, G_{f22}, G_{f23}, \dots \dots \dots & G_{f2\gamma} \\ G_{fg1}, G_{fg}, G_{fg3}, \dots \dots \dots & G_{fg\gamma} \\ \vdots & \ddots & \vdots \\ \vdots & \ddots & \vdots \\ \alpha_{11}, \alpha_{12}, \alpha_{13}, \dots \dots \dots \dots & \alpha_{1\gamma} \\ \alpha_{21}, \alpha_{22}, \alpha_{23}, \dots \dots \dots \dots & \alpha_{2\gamma} \\ \alpha_{m1}, \alpha_{m2}, \alpha_{m3}, \dots \dots \dots & \alpha_{m\gamma} \end{bmatrix}$$

where  $T_m \in \mathbb{R}^{(g+m) \times 2N}$ .

### 5.2.2.6 Classification and post-processing

The classification of pixels is done by training the classifier using the given training matrix,  $T_m = \{\varphi_1, \varphi_2, \dots \dots \varphi_\gamma\}$  where  $\varphi_i \in \mathbb{R}^{(g+m)}$  and the corresponding labels,  $L = \{l_1, l_2, \dots \dots, l_\gamma\}$  where  $l_{i=1,2,\dots,\gamma} \in \{0, 255\}$ . Once the classifier is trained, a patch of size  $p \times p$  (where  $p = 9$ ), around each and

every pixel of the query image is extracted and its Gabor feature vector,  $G_f \in \mathbb{R}^g$  is determined. If the standard deviation of the feature vector,  $G_f$  is non-zero, it forms the part of the query matrix,  $Q_m$ , where  $Q_m \in \mathbb{R}^{g \times q}$  and  $q$  is the number of feature vectors.  $Q_m$  is then normalized to zero mean and unit standard deviation using the  $l^2$  – norm. Using the already learned dictionary,  $D$  and the query matrix,  $Q_m$ , a test sparse matrix,  $T_s \in \mathbb{R}^{m \times q}$  is calculated. The test sparse matrix,  $T_s$ , is vertically concatenated (as done earlier in the case of  $T_m$ ) to  $Q_m$  to obtain test data matrix,  $Te_m$ .  $Te_m$  is supplied to the trained classifier, which designates each and every pixel of the query image as either a vessel pixel ( $V_p$ ) or a non-vessel pixel ( $NV_p$ ). Each of this classified value i.e. a vessel pixel ( $V_p$ ) or a non-vessel pixel ( $NV_p$ ) corresponds to the center pixel of the patch in the query image. It is important to note, that the padding of boundary pixels of the

query image is needed to be done with 0's. Ensemble classifier is used in this work for classification purposes, as it employs multiple models to give better prediction results than using a single model for prediction (Woźniak, Graña, & Corchado, 2014) (Ren, Zhang, & Suganthan, 2016). There are various ensemble learning techniques such as bagging, boosting and stacking, etc., each having its own advantages and limitations. In this work, a decision tree based model has been chosen as the classification model. The output of various weak learners is combined using the boosting learning technique as it is lesser prone to bias error and helps to build strong models for prediction (Woźniak et al., 2014). Two boosting learning techniques; AdaBoostM1 (Freund & Schapire, 1996) along with its variant LogitBoost (Friedman, Hastie, & Tibshirani, 2000b) have been employed in this work as they are less susceptible to the problem of overfitting which affects most of the other algorithms(Dietterich, 2000). Given a set of training examples  $(x_1, y_1), (x_2, y_2), \dots, (x_m, y_m)$  where labels  $y_i \in \{-1, +1\}$  and  $\mathbb{N}$ , number of iterations, a distribution is computed at each iteration to find the weak hypothesis,  $h_t$ . A weighted majority vote of the computed hypothesis,  $h_t$  is then calculated to obtain the overall hypothesis,  $H$ .

$$H(x) = \sum_{t=1}^{\mathbb{N}} w_t h_t(x). \quad (5.13)$$

where  $w_t$  is the weight assigned to each hypothesis,  $h_t$ . Adaboost greedily minimizes the loss  $\mathcal{L}$ , where

$$\mathcal{L} = \frac{1}{m} \sum_{i=1}^m \exp(-y_i H(x_i)). \quad (5.14)$$

The loss,  $\mathcal{L}$ , can be solved very effectively, however, a small classification error can cause an exponential change in the loss function making the AdaBoost algorithm a little vulnerable in the presence of the noise. This problem has been taken care of by the LogitBoost algorithm where instead of the exponential loss function, binomial log-likelihood loss function has been used(Friedman, Hastie, & Tibshirani, 2000a).

$$\mathcal{L} = \frac{1}{m} \sum_{i=1}^m -\log(1 + \exp(-y_i H(x_i))). \quad (5.15)$$

Table 5.2 shows various parameter settings for both the classifiers. Classification image produced by each of the classifiers is affected by impulse noise. In order to remove the noise, TV- $l_1$  denoising algorithm (Nikolova, 2004) has been applied in this work.

Table 5.2: The values of parameters employed for AdaBoost and LogitBoost classifiers

Parameter	Value
NumLearningCycles	100
Learners	‘tree’
Prior	‘empirical’
MaxNumSplits	10
LearnRate	1

## 5.3 Experimental Results

### 5.3.1 Material used

Performance evaluation of the techniques has been done on the publicly available datasets namely, DRIVE and STARE. Detailed information about these datasets has already been provided earlier and can be found under section 2.9.

### 5.3.2 Performance evaluation

During patch selection, only those patches of the query image corresponding to Gabor feature vectors having a non-zero standard deviation will be selected. The pixels of the query image corresponding to the patches, which are not selected, are directly marked as non-vessel pixels. The classified binary image obtained is affected by noise as shown in Fig. 5.5(c). Image denoising is done using TV- $l_1$  denoising algorithm to recover a high-quality image, free from unwanted data. The TV- $l_1$  Matlab code for denoising has been taken from <https://in.mathworks.com/matlabcentral/fileexchange/57604-tv-l1-image-denoising-algorithm>. The parameters used in the algorithm,  $\lambda$ , and  $\theta$ , are set to 1 and 0.5 respectively after extensive experimentation with different parameter values. The output of TV- $l_1$  is a normalized denoised image whose intensity values lie in the range [0, 1] where each value is the probability that the pixel belongs to the vessel but prior to denoising, the noisy image is eroded with a disk-shaped structuring element of size 10, to nullify the boundary effects as can be seen the Fig. 5.5(d). Once the boundary has been removed, the image is denoised using the TV- $l_1$  denoising algorithm discussed

earlier to obtain a noise-free image as shown in Fig. 5.5 (e). Although the image has now been denoised, it still contains some unwanted artefacts. In order to remove these artefacts, post-processing of the image is done. In post-processing, all the pixels which have an intensity value 1 (or 100% probability that they belong to the vessel) in the denoised image are marked as vessel pixels and all other pixels are marked as non-vessel pixels to obtain a binary image,  $I_{bin}$  as shown in Fig. 5.5(f).

Mathematically,

$$I_{bin} = \begin{cases} 0 (NV_p), & \text{if } I_l < 1 \\ 255 (V_p), & \text{otherwise} \end{cases} \quad (5.16)$$

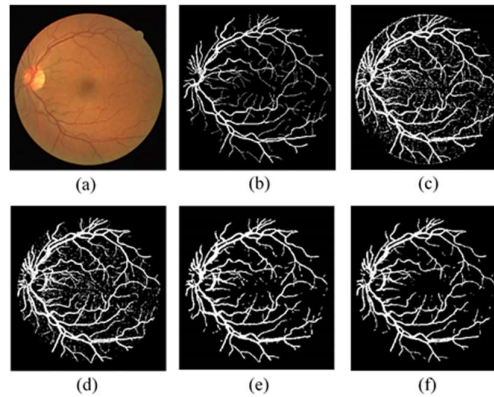


Fig 5.5 (a) Original image, (b) Gold standard image, (c) Segmented image obtained by the proposed technique, (d) Boundary effect removal, (e) Denoised Image, (f) Image obtained after applying post-processing ( $I_{bin}$ )

The average of the selected metrics was used to evaluate the performance of the proposed technique on both the datasets and it was found that the proposed method achieves higher accuracy values than the second human observer for both the classifiers as shown in Table 5.3 and 5.4. Further analysis shows, that though both the classifiers are able to produce similar results there is a fractional difference between their performances on different datasets. The LogitBoost algorithm produces better results in comparison to the AdaBoost algorithm for DRIVE dataset, whereas AdaBoost performs better for STARE dataset. The images, with the best and worst case accuracy for both DRIVE and STARE datasets are shown in Fig. 5.6 (using LogitBoost as it works better for DRIVE dataset) and Fig. 5.7 (using AdaBoost as it works better for STARE dataset) respectively along with the images by the first human observer. The

best and worst case accuracy achieved in case of AdaBoost for DRIVE dataset is 0.9657 and 0.9504 respectively whereas for LogitBoost it is 0.9663 and 0.9493. Best and worst case accuracy achieved for STARE dataset using the AdaBoost classifier is 0.9749 and 0.9226 respectively and for LogitBoost, it is 0.9756 and 0.9158 respectively. Overall the accuracy achieved using LogitBoost classifier for DRIVE dataset is 0.9595 which is slightly higher than 0.9592 obtained using AdaBoost classifier. Not only accuracy, but there is also a considerable difference in sensitivity obtained using both the classifiers. The sensitivity obtained using LogitBoost is 0.7914 which is significantly higher than 0.7821 obtained using the AdaBoost classifier. This implies that LogitBoost is better at classifying the vessel pixels than the AdaBoost classifier for the DRIVE dataset. In contrast, AdaBoost classifier works better for STARE dataset, in which case the overall accuracy achieved by AdaBoost classifier is 0.9529 which is higher than 0.9518 obtained using LogitBoost classifier.

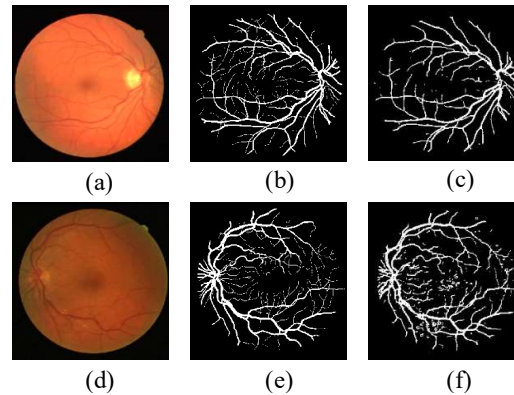


Fig 5.6 Best and Worst Case accuracy for the DRIVE dataset using LogitBoost classifier. (a), (d) Original image, (b), (e) Gold standard image by the 1<sup>st</sup> observer, (c), (f) Segmentation achieved by the proposed technique.

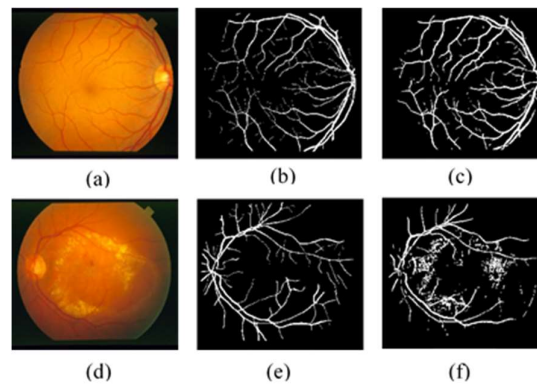


Fig 5.7 Best and Worst Case accuracy for the STARE dataset using AdaBoost classifier. (a), (d) Original image, (b), (e) Gold standard image by the 1<sup>st</sup> observer, (c), (f) Segmentation achieved by the proposed technique.

Comparative analysis of the proposed technique with the other state of the art techniques is presented in Table 5.3 and 5.4. Results show that the proposed technique performs better than the majority of the methods published in the last ten years. The proposed technique also performs better than the Ricci et al. technique, which achieved best overall performance towards vessel extraction as discussed in the earlier chapter (Chapter-3). The proposed technique performed better than the Ricci et al. technique on the DRIVE dataset in achieving higher overall accuracy besides detecting higher number of vessel pixels whereas it performed comparatively similar in terms of accuracy on the STARE dataset though it underperformed in the case of vessel pixels detection.

Table 5.3: Comparative analysis of vessel segmentation techniques on DRIVE dataset

<b>Method</b>	<b>Year</b>	<b>Sensitivity</b>	<b>Specificity</b>	<b>Accuracy</b>
2 <sup>nd</sup> observer	-	0.7796	0.9717	0.9470
<b>Unsupervised methods</b>				
Budai et al. [2]	2013	0.6440	0.9870	0.9572
Zhao at al. [3]	2014	0.7354	0.9789	0.9477
Roychowdhury et al.	2015	0.7390	0.9780	0.9490
Shehhi et al. [5]	2016	0.8500	0.9440	0.9340
<b>Deep learning method</b>				
Wang et al. [6]	2015	0.8173	0.9733	0.9767
Liskowski et al. [7]	2016	0.8460	0.9673	0.9507
Fu et al. [8]	2016	0.7603	N.A	0.9523
<b>Supervised methods</b>				
Staal [9]	2004	N.A	N.A	0.9441
Soares [10]	2006	0.7332	0.9782	0.9461
Ricci [11]	2007	0.742	0.9810	0.9580
Lupascu et al. [12]	2010	0.7200	N.A	0.9597
Marin et al. [13]	2011	0.7067	0.9801	0.9452
Zhang et al. [14]	2015	0.7812	0.9668	0.9504
Vega et al. [15]	2015	0.7444	0.9600	0.9412
Lazar et al. [16]	2015	0.7646	N.A	0.9458
Singh et al. [17]	2016	0.7594	N.A	0.9522
Javidi et al. [18]	2017	0.7201	0.9702	0.9450
Memari et al. [19]	2017	0.8726	0.9884	0.9722
Bahadar et al. [20]	2018	0.7300	0.9790	0.9580
Wang et al. [21]	2018	0.7236	0.9810	0.9449
<b>Proposed method</b>	<b>2018</b>	<b>0.7821</b>	<b>0.9747</b>	<b>0.9592</b>
<b>Proposed method</b>	<b>2018</b>	<b>0.7914</b>	<b>0.9741</b>	<b>0.9595</b>

Table 5.4: Comparative analysis of vessel segmentation techniques on STARE dataset

<b>Method</b>	<b>Year</b>	<b>Sensitivity</b>	<b>Specificity</b>	<b>Accuracy</b>
2 <sup>nd</sup> observer	-	0.8951	0.9384	0.9348
<b>Unsupervised methods</b>				
Budai et al. [2]	2013	0.5800	0.9820	0.9386
Zhao at al. [3]	2014	0.7187	0.9767	0.9509
Roychowdhury et al.	2015	0.7320	0.9840	0.9560
Shehhi et al. [5]	2016	0.6330	0.9500	0.9240
<b>Deep learning method</b>				
Wang et al [6]	2015	0.8104	0.9791	0.9813
Liskowski et al. [7]	2016	0.9289	0.9710	0.9667
Fu et al. [8]	2016	0.7412	N.A	0.9585
<b>Supervised methods</b>				
Staal [9]	2004	N.A	N.A	0.9516
Soares [10]	2006	0.7207	0.9747	0.9479
Ricci [11]	2007	0.825	0.965	0.9530
Lupascu et al. [12]	2010	N.A	N.A	N.A
Marin et al. [13]	2011	0.6944	0.9819	0.9526
Zhang et al. [14]	2015	N.A	N.A	N.A
Vega et al. [15]	2015	0.7019	0.9671	0.9483
Lazar et al. [16]	2015	0.7248	N.A	0.9492
Singh et al. [17]	2016	0.7939	N.A	0.9270
Javidi et al. [18]	2017	0.7780	0.9653	0.9517
Memari et al. [19]	2017	0.8085	0.9798	0.9514
Bahadar et al. [20]	2018	0.7900	0.9650	0.9510
Wang et al. [21]	2018	0.7486	0.9680	0.9460
<b>Proposed method</b>	<b>2019</b>	<b>0.7689</b>	<b>0.9652</b>	<b>0.9529</b>
<b>Proposed method</b>	<b>2019</b>	<b>0.7840</b>	<b>0.9629</b>	<b>0.9518</b>

It has been observed to the best of the knowledge of the authors, that the only methods that perform better than the proposed technique are deep learning based techniques but the major drawback associated with deep learning techniques is that they are computationally intensive and require a huge amount of time and memory for training besides the expensive and dedicated graphical processors as discussed earlier. The average training time (available) comparison of various traditional and deep learning techniques along with the proposed technique has been made in Table 5.5. Comparative analysis shows that the proposed technique has a less computational burden in comparison to other techniques.

Table 5.5: Comparison of average training time of various methods

Method	Time (hours)	Hardware
Wang et al [6]	192	4 Intel Xeon CPUs at 2 GHz with 256 GB RAM
Liskowski et al. [7]	8	NVIDIA GTX Titan
Fu et al. [8]	24	NVIDIA K40
Soares et al. [10]	9	AMD Athlon XP (2167 MHZ)
Memari et al. [19]	8.66	Core i7-3370 3.4GHZ with 8GB RAM
Proposed Method (AdaBoost)	1.83	NVIDIA GTX 1080
Proposed Method (LogitBoost)	1.67	NVIDIA GTX 1080

It has been further perceived that the number of training samples (patches) has a profound impact on computational time. Experimentally it has been found, that while training the model, each additional sample increases the computational cost by 10.29 ms. The only method that uses a comparable number of samples in regard to the proposed method (280,000 samples) is the deep learning based technique (Liskowski & Krawiec, 2016), which uses 400,000 samples. A sincere effort was therefore made to assess the performance of the proposed method using 400,000 samples and it was noticed that there was a minor improvement in the performance of the proposed technique which came at a very high computational cost. It is therefore advantageous to use a lesser number of samples to achieve comparative performance with much lesser computational time. An attempt has been made to assess the effect of the patch size on the outcome of the result and it has been discerned that the patch size plays a major role in the accurate extraction of the blood vessels. Table 5.6, 5.7, 5.8 and 5.9 show the effect of the patch size on various parameters.

Table 5.6: Effect of patch size on various parameters in the case of DRIVE dataset using AdaBoost technique

Patch Size	Sensitivity	Specificity	Accuracy
5*5	0.5621	0.9592	0.9256
7*7	0.713	0.9694	0.9476
9*9	<b>0.7821</b>	<b>0.9747</b>	<b>0.9592</b>
11*11	0.6868	0.9684	0.9445
13*13	0.5459	0.9536	0.9191

Table 5.7: Effect of patch size on various parameters in the case of DRIVE dataset using LogitBoost

Patch Size	Sensitivity	Specificity	Accuracy
5*5	0.5768	0.9587	0.9264
7*7	0.721	0.9677	0.9467
9*9	<b>0.7914</b>	<b>0.9741</b>	<b>0.9595</b>
11*11	0.704	0.9653	0.9431
13*13	0.549	0.9521	0.918

Table 5.8: Effect of patch size on various parameters in the case of STARE dataset using AdaBoost

Patch Size	Sensitivity	Specificity	Accuracy
5*5	0.4879	0.9553	0.9223
7*7	0.6808	0.9617	0.9424
9*9	<b>0.7689</b>	<b>0.9652</b>	<b>0.9529</b>
11*11	0.7085	0.9588	0.9415
13*13	0.5881	0.946	0.9209

Table 5.9: Effect of patch size on various parameters in the case of STARE dataset using LogitBoost

Patch Size	Sensitivity	Specificity	Accuracy
5*5	0.4935	0.9534	0.9209
7*7	0.6969	0.959	0.941
9*9	<b>0.7840</b>	<b>0.9629</b>	<b>0.9518</b>
11*11	0.72	0.956	0.9398
13*13	0.5951	0.9442	0.9197

Therefore it is clear from the experimental results that the optimal patch size is  $9 \times 9$  as it gives the best values for sensitivity, specificity, and accuracy on both the datasets. An effort has also been made to assess the effect of the number of orientations on the outcome of the result and it was found that 6 orientations give the best result as shown in Table 5.10.

Table 5.10: Effect of number of orientations on various parameters for both DRIVE and STARE datasets

Dataset	Classifier	Sensitivity	Specificity	Accuracy
DRIVE (4 Orientations)	AdaBoost	0.7689	0.9756	0.9580
	LogitBoost	0.7707	0.9754	0.9580

	STARE	(4 Orientations)	AdaBoost	0.7681	0.9645	0.9512
	STARE	(4 Orientations)	LogitBoost	0.7697	0.9613	0.9485
DRIVE	(6 Orientations)	AdaBoost	<b>0.7821</b>	<b>0.9747</b>	<b>0.9592</b>	
		LogitBoost	<b>0.7914</b>	<b>0.9741</b>	<b>0.9595</b>	
STARE	(6 Orientations)	AdaBoost	<b>0.7689</b>	<b>0.9652</b>	<b>0.9529</b>	
		LogitBoost	<b>0.7840</b>	<b>0.9629</b>	<b>0.9518</b>	
DRIVE	(8 Orientations)	AdaBoost	0.7653	0.9767	0.9587	
		LogitBoost	0.7855	0.9742	0.9581	
STARE	(8 Orientations)	AdaBoost	0.7615	0.9657	0.9519	
		LogitBoost	0.7669	0.9641	0.9508	

Experiments were done to find an optimal Gabor filter size and it was observed that the filter of size  $7 \times 7$  gives the best result in terms of sensitivity, specificity and accuracy as shown in Table 5.11 and 5.12.

Table 5.11: Effect of Gabor filter size on various parameters for DRIVE dataset

Filter Size	Classifier	Sensitivity	Specificity	Accuracy
$5 \times 5$	AdaBoost	0.7716	0.9746	0.9573
	LogitBoost	0.7774	0.9749	0.9581
$7 \times 7$	AdaBoost	<b>0.7821</b>	<b>0.9747</b>	<b>0.9592</b>
	LogitBoost	<b>0.7914</b>	<b>0.9741</b>	<b>0.9595</b>
$9 \times 9$	AdaBoost	0.7747	0.9745	0.9575
	LogitBoost	0.7911	0.9730	0.9567

Table 5.12: Effect of Gabor filter size on various parameters for STARE dataset

Filter Size	Classifier	Sensitivity	Specificity	Accuracy
5 × 5	AdaBoost	0.7548	0.9659	0.9516
	LogitBoost	0.7655	0.9644	0.9509
7 × 7	AdaBoost	<b>0.7689</b>	<b>0.9652</b>	<b>0.9529</b>
	LogitBoost	<b>0.7840</b>	<b>0.9629</b>	<b>0.9518</b>
9 × 9	AdaBoost	0.7686	0.9671	0.9521
	LogitBoost	0.7815	0.9613	0.9492

Further, in the proposed work, it is worth mentioning that if the size of the dictionary is increased to 512 or 1024 along with the number of iterations for training the dictionary, higher performance in terms of sensitivity, specificity, and accuracy can be obtained but it comes at the cost of high computational time. Furthermore, it is worth mentioning that there are some other existing studies which also have used KSVD along with OMP for vessel extraction from retinal images. Most of the studies differ in terms of the number of dictionaries used, feature vector values and classification techniques. One of the recent such technique is proposed by Javidi et al. (Javidi et al., 2017) where two dictionaries, one corresponding to vessel pixels and other to non-vessel pixels have been learned. The dictionary feature vectors consist of the intensity values normalized to zero mean and unit variance. In the proposed work, only one dictionary is learned for both vessel and non-vessel pixels. Learning one dictionary over two dictionaries requires significantly lesser time. Besides, in the proposed technique, rather than intensity values, Gabor feature values, and their corresponding sparse coefficient values have been used to create the feature vectors. The advantage of using Gabor feature values over intensity values is that they provide meaningful information by taking into account the orientation of various neighbors of the pixel under consideration. Another major benefit associated with Gabor feature values is that they are resistant to photometric effects such as improper illumination which can directly affect the intensity values. It is important to state that various classification

techniques have been used in different studies to classify the pixels into the vessel and non-vessel pixels but in this work, boosting technique has been chosen because of its strong predictive power besides low bias and variance which results in the better generalization of the unseen pixels. In this work two boosting techniques, AdaBoost and LogitBoost have been used. The performance of both the techniques is comparable in terms of accuracy and specificity but there is a significant difference in the case of sensitivity on both the DRIVE and STARE datasets. It has been observed that LogitBoost is better at identifying the vessel pixels in comparison to the AdaBoost technique and this is because of the fact that LogitBoost technique is better at handling annoying artefacts such as noise and low contrast which affect the classification process (Friedman et al., 2000a). Overall, it can be concluded that proposed feature based dictionary learning technique delivers very promising results with lesser training as compared to some of the renowned methods and deep learning techniques which require a lot of samples for training the classifier.

## 5.4 Chapter summary

In this chapter, a novel technique based on dictionary learning and sparse coding has been proposed. The dictionary is learned from Gabor feature vectors calculated at various scales and orientations for the patches extracted randomly from the images. A combination of the Gabor feature vectors and the corresponding sparse coefficient vectors is used for classification. For classification, two ensemble based classifiers based on boosted decision trees, AdaBoost and LogitBoost are evaluated. Publicly available, DRIVE and STARE datasets have been used for the evaluation of the proposed technique. It has been observed that the LogitBoost algorithm performs better than the AdaBoost algorithm in the classification of pixels for the same number of training samples on DRIVE dataset whereas AdaBoost performs better on STARE dataset. Results show that the proposed technique performs better than most of the state of the art techniques published recently.

# **Chapter 6**

## **Conclusion and Future Scope**

---

---

Concluding remarks have been presented in this chapter which have been framed on the basis of the design and analysis of the techniques proposed in this research work. Contributions of the work have been summarized and an insight to the future direction has been provided in which the work can be further extended.

### **6.1 Conclusion**

Diseases are on the surge and this surge can be attributed to human lifestyle and various other factors. Some of these diseases may lead into life threatening situations if not diagnosed earlier in their beginning stage. Early diagnosis may steer into effective treatment and save the person from dire consequences associated with the diseases. One of the most effective and efficient way to diagnose various diseases is retinal imaging in which the image of the retina is captured by a low power microscope. Blood vessels are then extracted from the retinal images which are then carefully examined by the ophthalmologist to find any irregularities that may exist in the structure. Presence of irregularities indicate the existence of the disease. Extracting blood vessels from the images is a complex and challenging task as various factors affect the accuracy of extraction of the blood vessels such as low and non-uniform radiance/illumination, low contrast, and noise.

Although a lot of work has been done on increasing the contrast of the images besides denoising, very less work has been done to address the problem of low and non-uniform illumination in images. In this work, three image enhancement techniques namely; Histogram clipping, Radiance indicator based histogram equalization for retinal vessel enhancement (RIHE-RVE), and Radiance indicator based histogram equalization for recursive retinal vessel enhancement (RIHE-RRVE) have been proposed that enhances the quality of the images by resolving the issue of low and non-uniform illumination. The techniques RIHE-RVE and RIHE-RRVE take care of low

and improper illumination in the images whereas histogram clipping controls the over-enhancement and does not allow it to move beyond optimal value. Performance evaluation of the techniques has been done on the publicly available datasets namely; Digital retinal images for vessel extraction (DRIVE), Structured analysis of the retina (STARE), Child heart and health study in England (CHASE), and Open access series of imaging studies (OASIS). Quantitative analysis of the proposed techniques has been done using the metrics Entropy (Information content), Structured similarity index (SSIM), Peak signal to noise ratio (PSNR), and Euclidean distance. Qualitative inspection of the images shows that the images enhanced by the proposed technique has high and uniform illumination.

Finally, an improved vessel segmentation technique based on dictionary learning and sparse coding approach has been proposed to achieve higher accuracy in the extraction of the blood vessels from the retinal images. Ensemble classification technique using AdaBoost and LogitBoost classifiers has been used to classify the pixels into vessel and non-vessel pixels. The feature vectors to train the classifiers consist of the combination of both the sparse codes obtained from the dictionary using KSVD and Gabor feature values obtained at multiscale. Performance evaluation of the technique has been done on the publicly available DRIVE and STARE datasets. Both the quantitative as well as qualitative results indicate that the proposed technique exhibits higher performance in terms of the metrics, Sensitivity (SN), Specificity (SP), and Accuracy (ACC) than the majority of the state of the art techniques.

## **6.2 Significance to the Society**

Commonly occurring diseases such as diabetes and hypertension etc. are on the surge which may lead to various vision threatening eye diseases such as diabetic retinopathy, macular degeneration etc. These diseases if not diagnosed early may lead to permanent vision loss. Not only eye diseases but some non-eye diseases such as neurological diseases and cardiological diseases can also be diagnosed by careful examination of the retinal blood vessels. This is a very novel area in which the diseases can be investigated without any blood tests. In order to diagnose these diseases, the blood vascular structure of the retina is needed to be analyzed for various abnormalities but extracting the

vascular structure of the blood vessels from the retinal images is very complex and time consuming. The proposed technique contributes towards accurate extraction of the blood vascular structure from the retinal images with minimum effort.

### **6.3 Scope of Future Work**

Although the proposed technique is very effective and efficient at extracting the blood vessels from the retinal images, still there is a scope of improvement in it. Though the technique can very accurately segment the blood vessels from normal healthy images it suffers slightly while handling the pathological images as can be observed in the STARE dataset, so the technique can be further improved by making it robust to various pathologies. In this work, only Gabor features have been used along with the sparse codes to create feature vectors. A combination of various other features can also be tried in along with the sparse codes to achieve higher performance. The time complexity of the proposed technique can be further reduced by using a dimensionality reduction technique while still preserving the attained accuracy. Recently various deep learning techniques have been proposed which can be further explored and used along with dictionary learning techniques to obtain improved performance.



## References

---

---

- Al Shehhi, R., Marpu, P. R., & Woon, W. L. (2016). An Automatic Cognitive Graph-Based Segmentation for Detection of Blood Vessels in Retinal Images. *Mathematical Problems in Engineering*. <https://doi.org/10.1155/2016/7906165>
- Annunziata, R., Kheirkhah, A., Hamrah, P., & Trucco, E. (2015). Scale and curvature invariant ridge detector for tortuous and fragmented structures. *Lecture Notes in Computer Science (Including Subseries Lecture Notes in Artificial Intelligence and Lecture Notes in Bioinformatics)*. [https://doi.org/10.1007/978-3-319-24574-4\\_70](https://doi.org/10.1007/978-3-319-24574-4_70)
- Azzopardi, G., Strisciuglio, N., Vento, M., & Petkov, N. (2015). Trainable COSFIRE filters for vessel delineation with application to retinal images. *Medical Image Analysis*, 19(1), 46–57. <https://doi.org/10.1016/j.media.2014.08.002>
- Bankhead, P., Scholfield, C. N., McGeown, J. G., & Curtis, T. M. (2012). Fast retinal vessel detection and measurement using wavelets and edge location refinement. *PLoS ONE*. <https://doi.org/10.1371/journal.pone.0032435>
- Birgui Sekou, T., Hidane, M., Olivier, J., & Cardot, H. (2017). Segmentation of retinal blood vessels using dictionary learning techniques. *Lecture Notes in Computer Science (Including Subseries Lecture Notes in Artificial Intelligence and Lecture Notes in Bioinformatics)*. [https://doi.org/10.1007/978-3-319-67561-9\\_9](https://doi.org/10.1007/978-3-319-67561-9_9)
- Budai, A., Bock, R., Maier, A., Hornegger, J., & Michelson, G. (2013). Robust vessel segmentation in fundus images. *International Journal of Biomedical Imaging*. <https://doi.org/10.1155/2013/154860>
- Carrillo, J. F., Hoyos, M. H., Dávila, E. E., & Orkisz, M. (2007). Recursive tracking of vascular tree axes in 3D medical images. *International Journal of Computer Assisted Radiology and Surgery*. <https://doi.org/10.1007/s11548-007-0068-6>
- Cetin, S., Demir, A., Yezzi, A., Degertekin, M., & Unal, G. (2013). Vessel tractography using an intensity based tensor model with branch detection. *IEEE Transactions on Medical Imaging*. <https://doi.org/10.1109/TMI.2012.2227118>
- Cetin, S., & Unal, G. (2015). A higher-order tensor vessel tractography for segmentation of vascular structures. *IEEE Transactions on Medical Imaging*. <https://doi.org/10.1109/TMI.2015.2425535>
- Chan, R. H., Chung-Wa, & Nikolova, M. (2005). Salt-and-pepper noise removal by median-type noise detectors and detail-preserving regularization. *IEEE Transactions on Image Processing*, 14(10), 1479–1485.

<https://doi.org/10.1109/TIP.2005.852196>

Chaudhuri, S., Chatterjee, S., Katz, N., Nelson, M., & Goldbaum, M. (1989). Detection of blood vessels in retinal images using two-dimensional matched filters. *IEEE Transactions on Medical Imaging*, 8(3), 263–269.  
<https://doi.org/10.1109/42.34715>

Chen, D., Mirebeau, J. M., & Cohen, L. D. (2016). Vessel tree extraction using radius-lifted keypoints searching scheme and anisotropic fast marching method. *Journal of Algorithms and Computational Technology*.  
<https://doi.org/10.1177/1748301816656289>

Chen, R., Dharmarajan, K., Kulkarni, V. T., Punnanithinont, N., Gupta, A., Bikdeli, B., ... Ranasinghe, I. (2013). Most Important Outcomes Research Papers on Hypertension. *Circulation: Cardiovascular Quality and Outcomes*, 6(4).  
<https://doi.org/10.1161/CIRCOUTCOMES.113.000424>

Cheng, Y., Hu, X., Wang, J., Wang, Y., & Tamura, S. (2015). Accurate vessel segmentation with constrained B-snake. *IEEE Transactions on Image Processing*.  
<https://doi.org/10.1109/TIP.2015.2417683>

Chengjun Liu, & Wechsler, H. (2002). Gabor feature based classification using the enhanced fisher linear discriminant model for face recognition. *IEEE Transactions on Image Processing*, 11(4), 467–476.  
<https://doi.org/10.1109/TIP.2002.999679>

Cherry, K. M., Peplinski, B., Kim, L., Wang, S., Lu, L., Zhang, W., ... Summers, R. M. (2014). Sequential Monte Carlo tracking of the marginal artery by multiple cue fusion and random forest regression. *Medical Image Analysis*.  
<https://doi.org/10.1016/j.media.2014.09.006>

Cheung, N., & Wong, T. Y. (2009). Microvascular changes in the retina as a risk marker for cardiovascular disease. *Current Cardiovascular Risk Reports*.  
<https://doi.org/10.1007/s12170-009-0009-8>

Congdon, N., Zheng, Y., & He, M. (2012). The worldwide epidemic of diabetic retinopathy. *Indian Journal of Ophthalmology*, 60(5), 428.  
<https://doi.org/10.4103/0301-4738.100542>

Dai, P., Luo, H., Sheng, H., Zhao, Y., Li, L., Wu, J., ... Suzuki, K. (2015). A new approach to segment both main and peripheral retinal vessels based on gray-voting and Gaussian mixture model. *PLoS ONE*.  
<https://doi.org/10.1371/journal.pone.0127748>

Dietterich, T. G. (2000). *Ensemble Methods in Machine Learning*.  
[https://doi.org/10.1007/3-540-45014-9\\_1](https://doi.org/10.1007/3-540-45014-9_1)

Elad, M., & Aharon, M. (2006). Image denoising via sparse and redundant

- representations over learned dictionaries. *IEEE Transactions on Image Processing*. <https://doi.org/10.1109/TIP.2006.881969>
- Fraz, M.M., Barman, S. A., Remagnino, P., Hoppe, A., Basit, A., Uyyanonvara, B., ... Owen, C. G. (2012). An approach to localize the retinal blood vessels using bit planes and centerline detection. *Computer Methods and Programs in Biomedicine*, 108(2), 600–616. <https://doi.org/10.1016/j.cmpb.2011.08.009>
- Fraz, Muhammad Moazam, Remagnino, P., Hoppe, A., Uyyanonvara, B., Rudnicka, A. R., Owen, C. G., & Barman, S. A. (2012). An Ensemble Classification-Based Approach Applied to Retinal Blood Vessel Segmentation. *IEEE Transactions on Biomedical Engineering*, 59(9), 2538–2548. <https://doi.org/10.1109/TBME.2012.2205687>
- Fraz, Muhammad Moazam, Rudnicka, A. R., Owen, C. G., & Barman, S. A. (2014). Delineation of blood vessels in pediatric retinal images using decision trees-based ensemble classification. *International Journal of Computer Assisted Radiology and Surgery*. <https://doi.org/10.1007/s11548-013-0965-9>
- Freund, Y., & Schapire, R. E. (1996). Experiments with a New Boosting Algorithm. *Proceedings of the 13th International Conference on Machine Learning*. <https://doi.org/10.1.1.133.1040>
- Friedman, J., Hastie, T., & Tibshirani, R. (2000a). Additive logistic regression: A statistical view of boosting. *Annals of Statistics*. <https://doi.org/10.1214/aos/1016218223>
- Friedman, J., Hastie, T., & Tibshirani, R. (2000b). Additive logistic regression: a statistical view of boosting (With discussion and a rejoinder by the authors). *The Annals of Statistics*, 28(2), 337–407. <https://doi.org/10.1214/aos/1016218223>
- Friman, O., Hindennach, M., Kühnel, C., & Peitgen, H.-O. (2010). Multiple hypothesis template tracking of small 3D vessel structures. *Medical Image Analysis*, 14(2), 160–171. <https://doi.org/10.1016/j.media.2009.12.003>
- Fu, H., Xu, Y., Lin, S., Kee Wong, D. W., & Liu, J. (2016). DeepVessel: Retinal Vessel Segmentation via Deep Learning and Conditional Random Field. In *Lecture Notes in Computer Science (including subseries Lecture Notes in Artificial Intelligence and Lecture Notes in Bioinformatics)* (pp. 132–139). [https://doi.org/10.1007/978-3-319-46723-8\\_16](https://doi.org/10.1007/978-3-319-46723-8_16)
- Haghhighat, M., Zonouz, S., & Abdel-Mottaleb, M. (2015). CloudID: Trustworthy cloud-based and cross-enterprise biometric identification. *Expert Systems with Applications*, 42(21), 7905–7916. <https://doi.org/10.1016/j.eswa.2015.06.025>
- Hassouna, M. S., & Farag, A. A. (2005). Robust Centerline Extraction Framework Using Level Sets. *2005 IEEE Computer Society Conference on Computer Vision and Pattern Recognition (CVPR'05)*, 1, 458–465.

<https://doi.org/10.1109/CVPR.2005.306>

- Hoover, A., Hoover, A.;Kouznetsova, V;Goldbaum, M., & Hoover, A. (2000). Locating blood vessels in retinal images by piecewise threshold probing of a matched filter response. *IEEE Transactions on Medical Imaging*, 19(3), 203–210. <https://doi.org/10.1109/42.845178>
- Javidi, M., Pourreza, H.-R., & Harati, A. (2017). Vessel segmentation and microaneurysm detection using discriminative dictionary learning and sparse representation. *Computer Methods and Programs in Biomedicine*, 139, 93–108. <https://doi.org/10.1016/j.cmpb.2016.10.015>
- Jiang, X., & Mojon, D. (2003). Adaptive local thresholding by verification-based multithreshold probing with application to vessel detection in retinal images. *IEEE Transactions on Pattern Analysis and Machine Intelligence*. <https://doi.org/10.1109/TPAMI.2003.1159954>
- Khan, K. B., Khaliq, A. A., Jalil, A., & Shahid, M. (2018). A robust technique based on VLM and Frangi filter for retinal vessel extraction and denoising. *PLOS ONE*, 13(2), e0192203. <https://doi.org/10.1371/journal.pone.0192203>
- Kim, M., & Chung, M. G. (2008). Recursively separated and weighted histogram equalization for brightness preservation and contrast enhancement. *IEEE Transactions on Consumer Electronics*, 54(3), 1389–1397. <https://doi.org/10.1109/TCE.2008.92269>
- Kolar, R., Kubena, T., Cernosek, P., Budai, A., Hornegger, J., Gazarek, J., ... Odstrcilik, J. (2013a). Retinal vessel segmentation by improved matched filtering: evaluation on a new high-resolution fundus image database. *IET Image Processing*. <https://doi.org/10.1049/iet-ipr.2012.0455>
- Kolar, R., Kubena, T., Cernosek, P., Budai, A., Hornegger, J., Gazarek, J., ... Odstrcilik, J. (2013b). Retinal vessel segmentation by improved matched filtering: evaluation on a new high-resolution fundus image database. *IET Image Processing*, 7(4), 373–383. <https://doi.org/10.1049/iet-ipr.2012.0455>
- Lam, B. S. Y., Gao, Y., & Liew, A. W. C. (2010). General retinal vessel segmentation using regularization-based multiconcavity modeling. *IEEE Transactions on Medical Imaging*. <https://doi.org/10.1109/TMI.2010.2043259>
- Läthén, G., Jonasson, J., & Borga, M. (2010). Blood vessel segmentation using multi-scale quadrature filtering. *Pattern Recognition Letters*. <https://doi.org/10.1016/j.patrec.2009.09.020>
- Law, M. W. K., & Chung, A. C. S. (2010). An oriented flux symmetry based active contour model for three dimensional vessel segmentation. *Lecture Notes in Computer Science (Including Subseries Lecture Notes in Artificial Intelligence and Lecture Notes in Bioinformatics)*. [https://doi.org/10.1007/978-3-642-15558-7\\_13](https://doi.org/10.1007/978-3-642-15558-7_13)

- Law, W. K., & Chung, A. C. S. (2006). Segmentation of vessels using weighted local variances and an active contour model. *Proceedings of the IEEE Computer Society Conference on Computer Vision and Pattern Recognition*. <https://doi.org/10.1109/CVPRW.2006.189>
- Lázár, I., & Hajdu, A. (2015). Segmentation of retinal vessels by means of directional response vector similarity and region growing. *Computers in Biology and Medicine*, 66, 209–221. <https://doi.org/10.1016/j.combiomed.2015.09.008>
- Lee, S., & Lee, S. (2015). Adaptive Kalman snake for semi-autonomous 3D vessel tracking. *Computer Methods and Programs in Biomedicine*, 122(1), 56–75. <https://doi.org/10.1016/j.cmpb.2015.06.008>
- Li, H., Yezzi, A., & Cohen, L. (2009). 3D multi-branch tubular surface and centerline extraction with 4D iterative key points. *Lecture Notes in Computer Science (Including Subseries Lecture Notes in Artificial Intelligence and Lecture Notes in Bioinformatics)*. [https://doi.org/10.1007/978-3-642-04271-3\\_126](https://doi.org/10.1007/978-3-642-04271-3_126)
- Li, Q., Feng, B., Xie, L., Liang, P., Zhang, H., & Wang, T. (2016). A cross-modality learning approach for vessel segmentation in retinal images. *IEEE Transactions on Medical Imaging*. <https://doi.org/10.1109/TMI.2015.2457891>
- Liskowski, P., & Krawiec, K. (2016). Segmenting Retinal Blood Vessels With Deep Neural Networks. *IEEE Transactions on Medical Imaging*, 35(11), 2369–2380. <https://doi.org/10.1109/TMI.2016.2546227>
- Marcus, D. S., Wang, T. H., Parker, J., Csernansky, J. G., Morris, J. C., & Buckner, R. L. (2007). Open Access Series of Imaging Studies (OASIS): Cross-sectional MRI Data in Young, Middle Aged, Nondemented, and Demented Older Adults. *Journal of Cognitive Neuroscience*, 19(9), 1498–1507. <https://doi.org/10.1162/jocn.2007.19.9.1498>
- Marín, D., Aquino, A., Gegundez-Arias, M. E., & Bravo, J. M. (2011). A New Supervised Method for Blood Vessel Segmentation in Retinal Images by Using Gray-Level and Moment Invariants-Based Features. *IEEE Transactions on Medical Imaging*, 30(1), 146–158. <https://doi.org/10.1109/TMI.2010.2064333>
- Memari, N., Ramli, A. R., Saripan, M. I. Bin, Mashohor, S., & Moghbel, M. (2017). Supervised retinal vessel segmentation from color fundus images based on matched filtering and AdaBoost classifier. *PLoS ONE*. <https://doi.org/10.1371/journal.pone.0188939>
- Moreno, R., & Smedby, Ö. (2015). Gradient-based enhancement of tubular structures in medical images. *Medical Image Analysis*. <https://doi.org/10.1016/j.media.2015.07.001>

- Nägele, M. P., Barthelmes, J., Ludovici, V., Cantatore, S., Von Eckardstein, A., Enseleit, F., ... Flammer, A. J. (2018). Retinal microvascular dysfunction in heart failure. *European Heart Journal*. <https://doi.org/10.1093/eurheartj/ehx565>
- Nikolova, M. (2004). A Variational Approach to Remove Outliers and Impulse Noise. *Journal of Mathematical Imaging and Vision*. <https://doi.org/10.1023/B:JMIV.0000011920.58935.9c>
- Oliveira, W. S., Teixeira, J. V., Ren, T. I., Cavalcanti, G. D. C., & Sijbers, J. (2016). Unsupervised Retinal Vessel Segmentation Using Combined Filters. *PLOS ONE*, 11(2), e0149943. <https://doi.org/10.1371/journal.pone.0149943>
- Ooi, C., & Mat Isa, N. (2010). Quadrants dynamic histogram equalization for contrast enhancement. *IEEE Transactions on Consumer Electronics*, 56(4), 2552–2559. <https://doi.org/10.1109/TCE.2010.5681140>
- Ooi, C., Pik Kong, N., & Ibrahim, H. (2009). Bi-histogram equalization with a plateau limit for digital image enhancement. *IEEE Transactions on Consumer Electronics*, 55(4), 2072–2080. <https://doi.org/10.1109/TCE.2009.5373771>
- Qian Zhao, Y., Hong Wang, X., Fang Wang, X., & Shih, F. Y. (2014). Retinal vessels segmentation based on level set and region growing. *Pattern Recognition*. <https://doi.org/10.1016/j.patcog.2014.01.006>
- Querques, G., Borrelli, E., Sacconi, R., De Vitis, L., Leocani, L., Santangelo, R., ... Bandello, F. (2019). Functional and morphological changes of the retinal vessels in Alzheimer's disease and mild cognitive impairment. *Scientific Reports*, 9(1), 63. <https://doi.org/10.1038/s41598-018-37271-6>
- Rahebi, J., & Hardalaç, F. (2014). Retinal blood vessel segmentation with neural network by using gray-level co-occurrence matrix-based features patient facing systems. *Journal of Medical Systems*. <https://doi.org/10.1007/s10916-014-0085-2>
- Ren, Y., Zhang, L., & Suganthan, P. N. (2016). Ensemble Classification and Regression-Recent Developments, Applications and Future Directions [Review Article]. *IEEE Computational Intelligence Magazine*. <https://doi.org/10.1109/MCI.2015.2471235>
- Ricci, E., & Perfetti, R. (2007). Retinal blood vessel segmentation using line operators and support vector classification. *IEEE Transactions on Medical Imaging*. <https://doi.org/10.1109/TMI.2007.898551>
- Rodrigues, P., Guimarães, P., Santos, T., Simão, S., Miranda, T., Serranho, P., & Bernardes, R. (2013). Two-dimensional segmentation of the retinal vascular network from optical coherence tomography. *Journal of Biomedical Optics*, 18(12), 126011. <https://doi.org/10.1117/1.JBO.18.12.126011>
- Roychowdhury, S., Koozekanani, D., & Parhi, K. (2014). Blood Vessel Segmentation

- of Fundus Images by Major Vessel Extraction and Sub-Image Classification. *IEEE Journal of Biomedical and Health Informatics*, 1–1. <https://doi.org/10.1109/JBHI.2014.2335617>
- Rubinstein, R., Zibulevsky, M., & Elad, M. (2008). Efficient implementation of the K-SVD algorithm using batch orthogonal matching pursuit. *CS Technion*.
- Rubinstein, R., Zibulevsky, M., & Elad, M. (2010). Double Sparsity: Learning Sparse Dictionaries for Sparse Signal Approximation. *IEEE Transactions on Signal Processing*, 58(3), 1553–1564. <https://doi.org/10.1109/TSP.2009.2036477>
- Shen, L. L., Bai, L., & Fairhurst, M. (2007). Gabor wavelets and General Discriminant Analysis for face identification and verification. *Image and Vision Computing*. <https://doi.org/10.1016/j.imavis.2006.05.002>
- Sim, K. S., Tso, C. P., & Tan, Y. Y. (2007). Recursive sub-image histogram equalization applied to gray scale images. *Pattern Recognition Letters*, 28(10), 1209–1221. <https://doi.org/10.1016/j.patrec.2007.02.003>
- Singh, K., Gupta, A., & Kapoor, R. (2015). Fingerprint image super-resolution via ridge orientation-based clustered coupled sparse dictionaries. *Journal of Electronic Imaging*, 24(4), 043015. <https://doi.org/10.1117/1.JEI.24.4.043015>
- Singh, K., Kapoor, R., & Nayar, R. (2015). Fingerprint denoising using ridge orientation based clustered dictionaries. *Neurocomputing*, 167, 418–423. <https://doi.org/10.1016/j.neucom.2015.04.053>
- Singh, K., Kapoor, R., & Sinha, S. K. (2015). Enhancement of low exposure images via recursive histogram equalization algorithms. *Optik*, 126(20), 2619–2625. <https://doi.org/10.1016/j.ijleo.2015.06.060>
- Singh, K., Vishwakarma, D. K., & Walia, G. S. (2019). Blind image deblurring via gradient orientation-based clustered coupled sparse dictionaries. *Pattern Analysis and Applications*. <https://doi.org/10.1007/s10044-017-0652-5>
- Singh, K., Vishwakarma, D. K., Walia, G. S., & Kapoor, R. (2016). Contrast enhancement via texture region based histogram equalization. *Journal of Modern Optics*, 63(15), 1444–1450. <https://doi.org/10.1080/09500340.2016.1154194>
- Singh, N., Kaur, L., & Singh, K. (2019). Histogram equalization techniques for enhancement of low radiance retinal images for early detection of diabetic retinopathy. *Engineering Science and Technology, an International Journal*. <https://doi.org/10.1016/j.jestch.2019.01.014>
- Singh, N. P., & Srivastava, R. (2016). Retinal blood vessels segmentation by using Gumbel probability distribution function based matched filter. *Computer Methods and Programs in Biomedicine*. <https://doi.org/10.1016/j.cmpb.2016.03.001>

- Soares, J. V. B., Leandro, J. J. G., Cesar, R. M., Jelinek, H. F., & Cree, M. J. (2006). Retinal vessel segmentation using the 2-D Gabor wavelet and supervised classification. *IEEE Transactions on Medical Imaging*, 25(9), 1214–1222. <https://doi.org/10.1109/TMI.2006.879967>
- Staal, J., Abramoff, M. D., Niemeijer, M., Viergever, M. A., & van Ginneken, B. (2004). Ridge-Based Vessel Segmentation in Color Images of the Retina. *IEEE Transactions on Medical Imaging*, 23(4), 501–509. <https://doi.org/10.1109/TMI.2004.825627>
- Tropp, J. A., & Gilbert, A. C. (2007). Signal recovery from random measurements via orthogonal matching pursuit. *IEEE Transactions on Information Theory*. <https://doi.org/10.1109/TIT.2007.909108>
- Vega, R., Sanchez-Ante, G., Falcon-Morales, L. E., Sossa, H., & Guevara, E. (2015). Retinal vessel extraction using Lattice Neural Networks with dendritic processing. *Computers in Biology and Medicine*, 58, 20–30. <https://doi.org/10.1016/j.combiomed.2014.12.016>
- Villalobos-Castaldi, F. M., Felipe-Riverón, E. M., & Sánchez-Fernández, L. P. (2010). A fast, efficient and automated method to extract vessels from fundus images. *Journal of Visualization*, 13(3), 263–270. <https://doi.org/10.1007/s12650-010-0037-y>
- Wang, Lei, Zhang, H., He, K., Chang, Y., & Yang, X. (2015). Active contours driven by multi-feature Gaussian distribution fitting energy with application to vessel segmentation. *PLoS ONE*. <https://doi.org/10.1371/journal.pone.0143105>
- Wang, Li, He, L., Mishra, A., & Li, C. (2009). Active contours driven by local Gaussian distribution fitting energy. *Signal Processing*. <https://doi.org/10.1016/j.sigpro.2009.03.014>
- Wang, Liwei, Zhang, Y., & Feng, J. (2005). On the Euclidean distance of images. *IEEE Transactions on Pattern Analysis and Machine Intelligence*. <https://doi.org/10.1109/TPAMI.2005.165>
- Wang, S., Yin, Y., Cao, G., Wei, B., Zheng, Y., & Yang, G. (2015). Hierarchical retinal blood vessel segmentation based on feature and ensemble learning. *Neurocomputing*, 149, 708–717. <https://doi.org/10.1016/j.neucom.2014.07.059>
- Wang, X., Heimann, T., Lo, P., Sumkauskaitė, M., Puderbach, M., de Bruijne, M., ... Wegner, I. (2012). Statistical tracking of tree-like tubular structures with efficient branching detection in 3D medical image data. *Physics in Medicine and Biology*. <https://doi.org/10.1088/0031-9155/57/16/5325>
- Welikala, R. A., Dehmeshki, J., Hoppe, A., Tah, V., Mann, S., Williamson, T. H., & Barman, S. A. (2014). Automated detection of proliferative diabetic retinopathy using a modified line operator and dual classification. *Computer Methods and*

*Programs in Biomedicine.* <https://doi.org/10.1016/j.cmpb.2014.02.010>

- Wong, W. L., Su, X., Li, X., Cheung, C. M. G., Klein, R., Cheng, C.-Y., & Wong, T. Y. (2014). Global prevalence of age-related macular degeneration and disease burden projection for 2020 and 2040: a systematic review and meta-analysis. *The Lancet Global Health*, 2(2), e106–e116. [https://doi.org/10.1016/S2214-109X\(13\)70145-1](https://doi.org/10.1016/S2214-109X(13)70145-1)
- Woźniak, M., Graña, M., & Corchado, E. (2014). A survey of multiple classifier systems as hybrid systems. *Information Fusion*, 16, 3–17. <https://doi.org/10.1016/j.inffus.2013.04.006>
- Xiao, Z., Adel, M., & Bourennane, S. (2013). Bayesian method with spatial constraint for retinal vessel segmentation. *Computational and Mathematical Methods in Medicine*. <https://doi.org/10.1155/2013/401413>
- Xu, C., & Prince, J. L. (1998). Snakes, shapes, and gradient vector flow. *IEEE Transactions on Image Processing*. <https://doi.org/10.1109/83.661186>
- Yang, Y., Huang, S., & Rao, N. (2008). An Automatic Hybrid Method for Retinal Blood Vessel Extraction. *International Journal of Applied Mathematics and Computer Science*, 18(3), 399–407. <https://doi.org/10.2478/v10006-008-0036-5>
- Yau, J. W. Y., Rogers, S. L., Kawasaki, R., Lamoureux, E. L., Kowalski, J. W., Bek, T., ... Wong, T. Y. (2012). Global Prevalence and Major Risk Factors of Diabetic Retinopathy. *Diabetes Care*, 35(3), 556–564. <https://doi.org/10.2337/dc11-1909>
- Yeong-Taeg Kim. (1997). Contrast enhancement using brightness preserving bi-histogram equalization. *IEEE Transactions on Consumer Electronics*, 43(1), 1–8. <https://doi.org/10.1109/30.580378>
- You, X., Peng, Q., Yuan, Y., Cheung, Y., & Lei, J. (2011). Segmentation of retinal blood vessels using the radial projection and semi-supervised approach. *Pattern Recognition*, 44(10–11), 2314–2324. <https://doi.org/10.1016/j.patcog.2011.01.007>
- Yu Wang, Qian Chen, & Baeomin Zhang. (1999). Image enhancement based on equal area dualistic sub-image histogram equalization method. *IEEE Transactions on Consumer Electronics*, 45(1), 68–75. <https://doi.org/10.1109/30.754419>
- Yureidini, A., Kerrien, E., & Cotin, S. (2012). Robust RANSAC-based blood vessel segmentation. *Medical Imaging 2012: Image Processing*. <https://doi.org/10.1117/12.911670>
- Zeng, Y. zhan, Zhao, Y. qian, Tang, P., Liao, M., Liang, Y. xiong, Liao, S. hui, & Zou, B. ji. (2017). Liver vessel segmentation and identification based on oriented flux symmetry and graph cuts. *Computer Methods and Programs in Biomedicine*. <https://doi.org/10.1016/j.cmpb.2017.07.002>

- Zhang, B., Karray, F., Li, Q., & Zhang, L. (2012). Sparse Representation Classifier for microaneurysm detection and retinal blood vessel extraction. *Information Sciences*, 200, 78–90. <https://doi.org/10.1016/j.ins.2012.03.003>
- Zhang, B., Zhang, L., Zhang, L., & Karray, F. (2010). Retinal vessel extraction by matched filter with first-order derivative of Gaussian. *Computers in Biology and Medicine*. <https://doi.org/10.1016/j.combiomed.2010.02.008>
- Zhang, Jin, Tang, Z., Gui, W., & Liu, J. (2016). Retinal vessel image segmentation based on correlational open active contours model. *Proceedings - 2015 Chinese Automation Congress, CAC 2015*. <https://doi.org/10.1109/CAC.2015.7382643>
- Zhang, Jiong, Dashtbozorg, B., Bekkers, E., Pluim, J. P. W., Duits, R., & Ter Haar Romeny, B. M. (2016). Robust Retinal Vessel Segmentation via Locally Adaptive Derivative Frames in Orientation Scores. *IEEE Transactions on Medical Imaging*. <https://doi.org/10.1109/TMI.2016.2587062>
- Zhang, L., Fisher, M., & Wang, W. (2015). Retinal vessel segmentation using multi-scale textons derived from keypoints. *Computerized Medical Imaging and Graphics*, 45, 47–56. <https://doi.org/10.1016/j.compmedimag.2015.07.006>
- Zhao, Y., Liu, Y., Wu, X., Harding, S. P., & Zheng, Y. (2015). Retinal vessel segmentation: An efficient graph cut approach with Retinex and local phase. *PLoS ONE*. <https://doi.org/10.1371/journal.pone.0122332>
- Zhao, Y., Rada, L., Chen, K., Harding, S. P., & Zheng, Y. (2015). Automated Vessel Segmentation Using Infinite Perimeter Active Contour Model with Hybrid Region Information with Application to Retinal Images. *IEEE Transactions on Medical Imaging*. <https://doi.org/10.1109/TMI.2015.2409024>
- Zhu, C., Zou, B., Xiang, Y., Cui, J., & Wu, H. (2016). An ensemble retinal vessel segmentation based on supervised learning in fundus images. *Chinese Journal of Electronics*. <https://doi.org/10.1049/cje.2016.05.016>
- Zhu, C., Zou, B., Zhao, R., Cui, J., Duan, X., Chen, Z., & Liang, Y. (2017). Retinal vessel segmentation in colour fundus images using Extreme Learning Machine. *Computerized Medical Imaging and Graphics*, 55, 68–77. <https://doi.org/10.1016/j.compmedimag.2016.05.004>
- Zolfagharnasab, H., & Naghsh-Nilchi, A. R. (2014). Cauchy based matched filter for retinal vessels detection. *Journal of Medical Signals and Sensors*.
- Zuiderveld, K. (1994). Contrast Limited Adaptive Histogram Equalization. In *Graphics Gems* (pp. 474–485). <https://doi.org/10.1016/B978-0-12-336156-1.50061-6>